

# **Spin-orbit Torques in Magnetic Heterostructures**

**Doctoral Thesis**

by

**Raghvendra Posti**

**(2018PHZ0011)**



**DEPARTMENT OF PHYSICS**

**INDIAN INSTITUTE OF TECHNOLOGY  
ROPAR**

**MAY 2024**

# Spin-orbit Torques in Magnetic Heterostructures

By

**Raghvendra Posti**

*Submitted*

*in fulfillment of the requirements for the degree*

*of*

**Doctor of Philosophy**



**Department of Physics**

**Indian Institute of Technology Ropar**

**December 2023**



©Indian Institute of Technology Ropar  
All rights reserved.

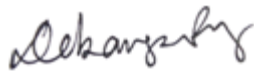


This thesis is dedicated to  
*My parents and my village.*



# Certificate

It is certified that the work contained in this thesis entitled “**Spin-orbit torques in magnetic heterostructures**” by **Mr. Raghvendra Posti**, a research scholar in the Department of Physics, Indian Institute of Technology Ropar, for the award of degree of **Doctor of Philosophy** has been carried out under my supervision and has not been submitted elsewhere for a degree.



Dr. Debangsu Roy

Assistant Professor

Department of Physics

Indian Institute of Technology Ropar

Rupnagar, Punjab- 140001, India

**December 2023**





# Declaration

I hereby declare that the work presented in the thesis entitled “**Spin-orbit torques in magnetic heterostructures**” submitted for the degree of **Doctor of Philosophy in Physics** by me to Indian Institute of Technology Ropar has been carried out under the supervision of **Dr. Debangsu Roy**. This work is original and has not been submitted in part or full by me elsewhere for a degree.



Raghvendra Posti

PhD Research Scholar

Department of Physics

Indian Institute of Technology Ropar

Rupnagar, Punjab-140001, India

**December 2023**



# Acknowledgements

I would like to express my deepest appreciation to the individuals without whom this journey would not have been possible.

First and foremost, I would like to sincerely acknowledge my supervisor Dr. Debangsu Roy, for introducing me this fascinating field of spintronics and for being an excellent guide. As the first student of his research group, we have worked day and night to build a laboratory from scratch. His academic and research expertise and his belief in my abilities helped me in establishing our research lab. He was always available with help, academically or personally, even during the unconventional hours of the day. Dr. Roy's guidance, availability for discussions, and his dedication to the work served as constant motivation for both myself and fellow lab members. His constructive criticism towards my scientific writings immensely contributed to my publications and the successful completion of this thesis.

I extend heartfelt thanks to the members of my Doctoral Committee—Dr. Asoka Biswas, Dr. Subhendu Sarkar, Dr. Shankhadeep Chakraborty, and Dr. Sudipta Sinha—for their individual insights and valuable suggestions throughout this journey.

Special appreciation goes to Dr. Dhanajay Tiwari and Dr. Alberto Anadon for their immense help and insightful discussions during the course of this thesis. Dr. Alberto's assistance with my queries on data analysis, particularly during the lab setup, is greatly appreciated.

I would like to thank my lab mates—Abhishek, Ajit, Preet Kamal, Adarsh, Chirag, Athira, and Kanupriya—for their academic support and for fostering a friendly and cheerful environment in the lab. I especially acknowledge Abhishek for his assistance in the lab setup and for being a constant presence, both personally and professionally, during the challenging days we faced.

Of course, I owe my deepest gratitude to my RDRS group—Sanjay, Damanpreet, and Rakhi—who have significantly contributed to my academic journey, bringing entertainment and joy to the experience. I heartily thank you guys for all the good times we had over the past five years, you guys showed immense care for a lazy person like me. We have seen each other grow professionally and personally from our first day of PhD to this very day. I'm truly thankful for these memories and I hope we continue to create many more. Thank you for the lifelong friendship.

I would like to thank Rajat bhai, Akanshu, Pragya, Chamola, and Hafsoah and for always being there when research was overwhelming. I want to thank all PG Lab 2 members—Nitin, Sahil, Vasu, Shagun, Pardeep, and Mukesh—for all the fun and memories that we made here, during our initial days. A heartfelt thank you to the TC Cricket group members, because of you guys' cricket remained as a constant source of joy for me during this journey. I would like to thank Sahab, Pawan, Rajat for all the fun and memories. I also acknowledge and thank all those who have been part of this journey, including those inadvertently omitted.

Most importantly, profound gratitude is extended to my family and my village. I thank my parents, dadi and my sisters for their unwavering support for my passion of science and their blessings. I would like to thank Shakuntala Puphu for being source of motivation for me since my first day of school to this very day. I would like to acknowledge my first physics teacher late Arvind guruji for his support, may your soul rest in peace.

Lastly, an acknowledgement for my village. The memories of my village, Lamgaundi, and the desire to contribute to its well-being, has always inspired me to put in extra efforts in my work.

## List of Publications

### Journal Articles:

1. D Kaur, Rakhi, **R. Posti**, J Singh, D Roy, S Sarkar, and M Kumar, “Nanopatterning Induced Si Doping in Amorphous Ga<sub>2</sub>O<sub>3</sub> for Enhanced Electrical Properties and Ultra-Fast Photodetection” Wiley Small 2309277 (2024)
2. **R. Posti**, A. Kumar, M. Baghoria, B Prakash, D. Tiwari, and D. Roy, “Odd symmetry planar Hall effect: A method of detecting current-induced in-plane magnetization switching,” *Applied Physics Letters* 122, 152405 (2023).
3. **R. Posti**, A. Kumar, D. Tiwari, and D. Roy, “Emergence of considerable thermoelectric effect due to the addition of an underlayer in Pt/Co/Pt stack and its application in detecting field free magnetization switching,” *Applied Physics Letters* 121, 223502 (2022).  
(Featured article on APL homepage)

### Submitted and Ongoing works

1. **R. Posti**, and D. Roy, “Universality of initialization-free multistate memory behavior in perpendicularly magnetized heterostructure: integration of spin-orbit torque and magnetic field” (*manuscript under review*)
2. A Kumar, C Kalouni, R Posti, V K Malik, D Tiwari, and D Roy, “Remanent Ferromagnetic Resonance Spectroscopy: A probe for magnetic state configurations in nanotubes” (*manuscript under review*)
3. P. Kamal, A. Tripathi, **R. Posti**, and D. Roy, Unveiling transverse dynamics of Neel Skyrmion amidst defect for enhanced magnetic storage applications (*manuscript under preparation*)
4. **R. Posti**, D Tiwari, and D. Roy, “Reconfigurable in-memory logic operations and two-step writing process induced multistate memory behavior in a single device” (*to be submitted*)



# Abstract

In the rapidly evolving landscape of modern electronics, where the relentless pursuit of enhanced performance and miniaturization has driven technological advancements, Moore's law has served as a guiding principle. However, as this law approaches a state of saturation due to the constant miniaturization of electronic components, alternative pathways, particularly spintronics, are being explored. This dissertation focuses on spin-orbit torque (SOT) as a key mechanism within spintronics to sustain and extend Moore's law.

The study investigates the SOT-induced magnetization reversal in ferromagnetic layers with both in-plane magnetic anisotropy (IMA) and perpendicular magnetic anisotropy (PMA). By characterizing SOT-induced effective fields in these heterostructures, the research demonstrates the capability to switch magnetization orientation. Taking a comprehensive approach, the investigation merges fundamental principles with practical applications, employing a heavy metal/ferromagnetic/heavy metal (HM/FM/HM) model for SOT devices.

The thesis unfolds with an introductory background on spin-orbit coupling and its effects on magnetic heterostructures, followed by a detailed description of experimental techniques and the room temperature transport measurements setup. Subsequent chapters delve into the separation of spin-orbit torque components from thermoelectric effects, the detection of SOT-induced field-free magnetization switching, exploration of multistate memory behavior, and the detection of in-plane magnetization switching using the odd symmetry planar Hall effect.

The study introduces novel reading mechanisms, such as the anomalous Nernst effect (ANE) and odd planar Hall voltage (O-PHV), to deepen understanding and demonstrate the potential of SOT-induced magnetization switching in various devices. The research reveals multistate memory behavior with potential applications in neuromorphic computing. The thesis concludes by summarizing key findings, and paving the way for future investigations in the field of spintronics, with a specific emphasis on spin-orbit torque.





## **List of abbreviations**

MRAM: Magnetic Random Access Memory

FM: Ferromagnetic metal

HM: Heavy Metal

IMA: In-Plane Magnetic Anisotropy

PMA: Perpendicular Magnetic Anisotropy

SOI: Spin Orbit Interaction

STT: Spin Transfer Torque

SOT: Spin Orbit Torque

SOC: Spin Orbit Coupling

SHE: Spin Hall Effect

REE: Rashba Edelstein Effect

LLG: Landau Lifshitz Gilbert Equation

AD-SOT: Anti-damping Spin Orbit Torque

FL-SOT: Field-Like Spin Orbit Torque

DMI: Dzyaloshinskii-Moriya Interaction

AFM: Atomic Force Microscopy

OHE: Ordinary Hall Effect

AHE: Anomalous Hall Effect

PHE: Planar Hall Effect

AC: Alternating Current

DC: Direct Current

PVD: Physical Vapour Deposition

SEM: Scanning Electron Microscopy

MTJ: Magnetic Tunnel Junction

SE: Scattered Electron

BSE: Back Scattered Electron

ANE: Anomalous Nernst Effect

# Contents

<b>Outline of the thesis</b>	<b>a</b>
<b>1. Introduction to basic concepts</b>	<b>1</b>
1.1 Magnetic anisotropy	1
1.2 Manipulation of magnetization	3
1.2.1 Magnetic field	4
1.2.2 Current-controlled magnetization	5
1.2.2.1 Spin-transfer torque(STT) mechanism	5
1.2.2.2 Spin-orbit torque (SOT) mechanism	6
1.3 Spin-Orbit coupling and Charge to Spin conversion	6
1.3.1 Spin-orbit Coupling	7
1.3.2 Charge current to spin current conversion	8
1.3.2.1 Spin Hall effect(SHE)	9
1.3.2.2 Rashba-Edelstein effect(REE)	11
1.4 SOT switching dynamics	12
1.5 Magnetisation reversal by SOT	15
1.5.1 Macrospin	15
1.5.2 Domain dynamics	16
1.5.3 Field-free magnetization switching	17
1.5.4 Experimental realization	18
1.6 Reading of magnetization reorientation	19
1.7 Characterization of Spin-orbit torques	21
1.7.1 Harmonic Hall method to characterize SOT	22
1.7.2 Thermoelectric effects	23
References	25
<b>2. Experimental technique and room temperature transport measurements setup</b>	<b>29</b>
2.1 Thin film deposition	29
2.1.1 Magnetron sputtering deposition	29
2.2 Atomic force microscopy	32
2.3 Vibration sample magnetometry (VSM)	33

2.4	Device fabrication	34
2.4.1	Photolithography	35
2.5	Scanning Electron Microscope (SEM)	36
2.6	Wire Bonding	38
2.7	Room temperature transport measurement setup	39
2.7.1	Instruments required	40
2.7.2	Bipolar Electromagnet and Helmholtz coils	41
2.7.3	Sample mount and breakout box	42
2.7.4	Rotational assembly	44
2.7.5	Source and measurement units	44
2.7.5.1	AC measurements	45
2.7.5.2	DC measurements	45
	References	47
<b>3.</b>	<b>Separation of Spin-orbit torque from thermoelectric effects and detection of SOT induced field-free magnetization switching in Pt/Co/Pt stack with Ta-underlayer utilizing thermoelectric effect</b>	<b>49</b>
3.1	Introduction	49
3.2	Experimental details	51
3.3	Results and discussion	52
3.3.1	Separation of AHE and PHE contributions	52
3.3.2	Anisotropy field ( $H_k$ ) calculations	53
3.3.2.1	For Pt/Co/Pt sample	53
3.3.2.2	For Ta/Pt/Co/Pt sample	53
3.3.3	SOT measurement for the Pt stack	54
3.3.4	Second harmonic signal comparison for Pt stack and Ta stack	56
3.3.5	SOT measurement for the Ta stack	57
3.3.6	Magnetization switching in Ta-stack	60
3.3.6.1	Current induced magnetization switching in Ta/Pt/Co/Pt stack	60
3.3.6.2	Field-free switching in Ta/Pt/Co/Pt stack	62
3.3.7	Repeatability of ANE nature in different Ta stacks	64
3.4	Conclusion	65
	References	66

<b>4. Multistate memory behavior of SOT induced magnetization switching in presence of an external field</b>	<b>69</b>
4.1 Introduction	69
4.2 Effect of external field ( $H_z$ ) on SOT	70
4.3 Multi-state memory behavior in HM/FM/HM stack	73
4.3.1 Sample alignment	74
4.3.2 Multistate SOT switching	75
4.4 Stabilization of domain states and presence of Néel domain walls	76
4.4.1 Presence of domain states	76
4.4.2 Presence of Néel domain walls	77
4.5 Energy barrier reduction with states	79
4.6 Initialization free multistate behaviour	81
4.6.1 Comparison of with-initialization and initialization free states	83
4.6.2 Exploring the sole effect of $H_z$ on multistate behavior	84
4.6.3 Retention of states after switching off the field $H_z$	84
4.6.4 Multistate behavior on sample other than Pt/Co/Pt	87
4.7 Conclusion	88
References	89
<b>5. Detection of in-plane magnetization switching using odd symmetry planar Hall Effect</b>	<b>93</b>
5.1 Introduction	93
5.2 Theoretical Background	95
5.3 Experimental Details	97
5.4 Results and Discussion	98
5.4.1 Magnetic properties of heterostructure	98
5.4.2 Odd symmetry planar Hall signal	99
5.4.3 SOT characterization in NiFe-stack	99
5.4.4 Comparison of reading mechanisms	101
5.4.5 Magnetization switching detection	102
5.4.6 Magnetization reversal energy barrier	103
5.5 Conclusion	105
References	106
<b>6. Conclusions and Outlook</b>	<b>109</b>



# List of Figures

1. Schematic of mechanisms used for writing operation of information in a MTJ bit. From left to right these are: current generated magnetic field, STT, SOT, and motion of domain walls (DW)	<b>b</b>
1.1. FM thickness dependency of magnetic anisotropy in Pd/Co multilayer. This heterostructure shows a PMA behavior for Co thickness less than $\sim 13$ Å	<b>3</b>
1.2. Magnetization manipulation schemes	<b>4</b>
1.3. Schematic of mechanisms used for writing operation of information in a MTJ bit. From left to right these are: current generated magnetic field, STT, SOT, and motion of domain walls (DW)	<b>5</b>
1.4. (a) Motion of electron in around the nucleus in laboratory frame of reference. (b) relative motion of nucleus around electron in electron's frame of reference	<b>7</b>
1.5. Skew scattering or Mott scattering mechanism illustrating the deflection of spin up electron due to magnetic field produced in electron's rest frame.	<b>9</b>
1.6. Illustration of side-jump scattering mechanism	<b>10</b>
1.7. FM/HM heterostructure illustrating the generation of spin current in HM due to SHE	<b>11</b>
1.8. Illustration of 2D electron gas fermi surface with Rashba coupling.	<b>12</b>
1.9. AD-SOT and FL-SOT affecting the magnetization dynamics in LLG equation	<b>14</b>
1.10. Schematic of macrospin picture illustrating the effect of SOT on FM magnetization	<b>15</b>
1.11. Effect of SOT on domain dynamics. The SOT effective field induces switching only in the presence of a symmetry breaking field	<b>16</b>
1.12. Experimental method to perform SOT induce magnetization switching involve short duration current pulses followed by a reading mechanism	<b>18</b>
1.13. Coordinate geometry defining magnetization and magnetic field.	<b>19</b>
1.14. Heat gradient produced due to resistivity differences of different layers	<b>23</b>



2.1. Schematic illustrating the operation of a magnetron sputtering system	31
2.2. Key elements of an atomic force microscope (AFM)	32
2.3. VSM data showing magnetization vs. field (applied along z-direction) plots for PMA (a) Pt/Co/Pt stack, and (b) Ta/Pt/Co/Pt stack. (c) Processed VSM data after slope correction	34
2.4. Diagram illustrating lithography techniques, showcasing (a) the lift-off process on the left and (b) the etching technique on the right	35
2.5. A schematic diagram of the scanning Electron Microscopy (SEM).	36
2.6. Main signals produced when the electron beam interacts with the sample	38
2.7. Schematic of bonding system	39
2.8. A schematic diagram of room temperature transport setup	40
2.9. (a) Eagle Cad generated gerber file image of 12-pin sample mount PCB design. (b) Pasted and bonded devices with different pads. (c) Actual sample mount PCB with a one-rupee coin for the size reference	42
2.10. Sample mount stage PCB for (a) xz-rotation (gerber image of design) (b) yz-rotation, and (xy-rotation)	43
2.11. (a) $M$ vs. $H_z$ result for Pt/Co/Pt PMA stack obtain by VSM measurement (b) $R$ vs $H_z$ results measured from AHE transport measurement	46
3.1. (a) Scanning electron microscopy image of the six-terminal Hall bar devices with Hall measurement geometry. (b) Magnetization measurements by VSM as a function of out-of-plane applied field ( $H_z$ ) and inset shows AHE resistance measurements vs. $H_z$	51
3.2. (a) First harmonic Hall resistance ( $R_H^\omega$ ) as a function of in-plane magnetic field applied at $\sim 45^\circ$ from current direction (For Pt/Co/Pt stack). (b) Separated AHE and PHE resistances as a function of in-plane field	52
3.3. (a) First harmonic Hall voltage data ( $V_H^\omega$ ) as a function of field along $x$ -direction ( $H_x$ ) for Pt/Co/Pt stack, the fitted curve in low field regime is shown in red color. (b) $\sin(2\theta)$ vs. $\sin(\theta_H - \theta)$ for Ta/Pt/Co/Pt stack at external magnetic field 4500 Oe	54

- 3.4. (a) Pt stack with directions of spin currents ( $J_s$ ) flowing from each HM layer and an effective spin current direction, along with the schematic diagram for the AC Hall measurement with its coordinate geometry. (b) First harmonic ( $V_H^\omega$ ) and second harmonic ( $V_H^{2\omega}$ ) voltage vs. magnetic field sweep in  $x$ -direction ( $H_x$ ) under  $\sim 4$  mA current. (c)  $V_H^\omega$  and  $V_H^{2\omega}$  vs. magnetic field sweep in  $y$ -direction ( $H_y$ ) under  $\sim 4$  mA current. (d)  $H_{AD}$  as a function of applied AC currents (inset:  $H_{FL}$  vs. AC current) **55**
- 3.5. (a)  $R_H^{2\omega}$  vs.  $H_x$  for Pt stack. Inset: zoom-in view of  $R_H^{2\omega}$  vs.  $H_x$  in lower field regime. (b)  $R_H^{2\omega}$  vs.  $H_x$  for Ta stack (Inset: thermal gradient due to resistivity mismatch, color gradients indicate the heat distribution in each layer. The darker portion represents the hot region, while the lighter portion represents the cold region in each layer in the picture, black arrows point from top to bottom layer, indicating heat flow direction. The thickness of the right arrow denotes the magnitude of the current flowing through these layers.), (c)  $R_H^{2\omega}$  vs.  $H_z$  comparison for Pt stack and Ta stack, measurements are performed at  $J_{AC} \sim 1 \times 10^{10} \text{ A/m}^2$  **57**
- 3.6.(a) Illustration of the experimental geometry and spin current ( $J_s$ ) and polarization directions ( $\sigma$ ) for each HM layer in Ta- stack. (b) Normalized  $R_H^\omega$  vs.  $\theta_H$ . (c)  $R_H^{2\omega}$  vs.  $\theta$  at different external magnetic fields. (d) Contributions of SOT and ANE as a function of  $1/(H_{ext}+H_k)$ . Measurements are performed at  $I_{AC} = 4.4$  mA **58**
- 3.7. Second harmonic Hall voltage  $V_H^{2\omega}$  as a function of magnetic field angle ( $\theta_H$ ) in  $yz$ -plane **59**
- 3.8. DC Hall resistance as a function of applied current pulse in presence of in-plane applied magnetic field. (Top portion shows plots in presence of positive values of in-plane magnetic field (in Oe) and bottom portion in presence of negative values of in-plane magnetic field (in Oe)) **61**
- 3.9.(a)  $R_H$  vs.  $I$  for Ta- stack with Co wedge and uniformly grown Ta stacks (inset: illustration of Co uniform and Co wedge in Ta stack). (b)  $R_H^{2\omega}$  (anomalous Hall resistance ( $R_H$ ) in the inset) vs.  $H_z$  for Ta stack. (c) Writing and reading scheme for the 2<sup>nd</sup> harmonic ANE based reading mechanism. (d)  $R_H^{2\omega}$  (left  $y$ -axis) and  $R_H$  (right  $y$ -axis) vs. applied current pulses (inset: retracing of  $R_{xy}^{2\omega}$  as a function of applied current pulses) **63**

- 3.10. Hysteric nature of  $R_H^{2\omega}$  vs.  $H_z$  for two different devices of Ta stack with Co thickness 0.6 nm in (a), and for a Ta stack device with Co thickness 0.85 nm in (b) **64**
- 4.1. (a) FM/HM model system with coordinate geometry. In-plane current through HM and external fields along x- and z- directions ( $H_x$  and  $H_z$ , respectively) are applied. (b) Root of Eq. (4.8) as a function of  $h_z$  ( $=H_z/H_k$ ). Here, various line plots represent the  $\sin\theta$  vs.  $h_z$  plot for a fix value of  $h_x$  ( $=H_x/H_k$ ) (numeric values of  $h_x$  are written to the right side of plot). Inset: normalized  $\sin\theta$  vs.  $h_z$  plot for different values of  $h_x$ . (c)  $H_{AD}$  value from Eq. (4.10) as a function of  $H_x$  in presence of different  $H_z$  values. (d) Results of micromagnetic simulation showing the trend of change in magnetization z-component ( $m_z$ ) during the action of  $H_z$  and a 4 ns current pulse **71**
- 4.2. (a) Misalignment ( $\theta$ ) between applied field ( $H_{ext}$ ) and current direction producing in-plane and out of plane component of  $H_{ext}$ . Polarity of hysteresis depending on the component of  $H_{ext}$  produced by (b)  $\theta > 0^\circ$ , and (c)  $\theta < 0^\circ$  **74**
- 4.3. SOT switching in presence of (a) negative and (b) positive  $H_z$  fields showing memristor behavior. (c) Trend of reduction of saturation state in SOT switching in presence of different  $H_z$  magnitude and polarity **74**
- 4.4. Switching field ( $H_c$ ), scaled by value of  $H_c$  when field is out of plane to the sample ( $H_c(0)$ ) and plotted as a function of angle of external field from z-axis ( $\theta$ ) (refer to Fig. 4.2 (a)) **76**
- 4.5. (a) Out of plane effective SOT field ( $H_{z,eff}$ ) acting on chiral and achiral DW. SOT induces chiral Néel wall motion (top). Contraction/expansion of DW by SOT, inducing magnetization switching depending on  $H_x$  polarity (bottom). (b) SOT loop shift as a consequence of  $\pm H_z$ . Here, a symmetry breaking field  $H_x \sim 1300$  Oe was also applied. (c) Linear trend of SOT induced hysteresis loop shift as a function of  $H_z$ . Linear plots with different slopes attributes to the different polarity of  $H_x$  **77**
- 4.6. (a) Energy barrier (red points) obtained from the Arrhenius fitting Eq. (4.13) at different  $H_z$  field values (Inset: Representative case for the fitting of Eq. (4.13) when  $H_z = 7$  Oe). Energy barrier modification with respect to the  $H_z$  field is well fitted by Eq. (4.15) (black line). (b) Comparison of energy barrier (red circle) reduction and reduction of saturation states (black square) as a function of  $H_z$  **80**

- 4.7. (a) Multistate SOT switching procedure in presence of initialization step. (b) in absence of initialization step (c) multistate data (red points) after initialization step (black points) (d) multistate data even in the absence of any initialization step **81**
- 4.8. (a) Conventional multistate behavior with (red circle) and without (black solid square) initialization step. +60 mA SOT current pulse with different  $H_z$  field stabilizing different states. Initialization step corresponds to the -60 mA pulse (b) Insufficient current pulse for SOT switching (+1 mA) and varying  $H_z$  showing no change in state or  $V_H$  **83**
- 4.9. Retention of different states after switching off the  $H_z$  field. States are read after various time intervals **84**
- 4.10. (a) SOT switching hysteresis after the application of various  $H_z$  fields. For each  $H_z$  field value Hall voltage (y-axis) of Hall bar device is recorded after an application of 5 mS current pulses (x-axis). (b) Trend of the reduction of saturation (i.e., Hall voltage at saturation, here it is read after the application of 5mS current pulse of +45 mA) as a function of  $H_z$  **86**
- 5.1. (a) Pt/Co/NiFe/Pt stack with the experimental geometries and SOT directions. (b) Planar Hall voltage ( $V_H$ ) vs.  $\phi_H$  in presence of 300 Oe (inset:  $V_H$  vs.  $H_x$ ). (c)  $V_H$  vs.  $H_z$ . (d)  $V_H$  vs.  $\phi_H$  from  $0^\circ$  to  $360^\circ$  (trace and retrace) in the presence of 5 Oe (black) and 22 Oe fields (red) **95**
- 5.2.(a) PHE voltage vs.  $H_x$  at  $\pm 5$  mA currents. (b)  $V_H(+5 \text{ mA}) - V_H(-5 \text{ mA})$ , and (c)  $V_H(+5 \text{ mA}) + V_H(-5 \text{ mA})$  vs.  $H_x$ . (d) O-PHV ( $\Delta V_H$ ) measured at magnetic field sweep step **97**
- 5.3. (a)  $R_{xy}^{2\omega}$  vs.  $H_x$  for different applied AC (solid circles) current and the fitted curve (corresponding lines) using Eq. 5.8. (b)  $H_{AD}$ ,  $H_I$ , and  $H_{Oe}$  contributions as a function of applied AC **98**
- 5.4. (a)  $V_H^{2\omega}$  vs.  $H_x$ . (b) O-PHV vs.  $H_x$  (at 1 mA applied currents) **99**
- 5.5. (a) Measurement scheme for the O-PHV method. (b) O-PHV (read by  $\pm 1$  mA) as function of DC pulses ( $I_{\text{write}}$ ) in the presence of different  $H_z$  fields (-30, 0, and, +20 Oe). (c) O-PHV (read currents  $\pm 1$  mA) after consecutive  $\pm 35$  mA pulses in presence of 20 Oe  $H_z$  **100**
- 5.6.  $I_c$  vs.  $\ln\left(\frac{\tau_p}{\tau_0}\right)$  for  $+m_x$  to  $-m_x$  and  $-m_x$  to  $+m_x$  (data points are fitted with Eq. (5.9)) **102**



## List of tables

3.1. Comparison of SOT efficiencies in our stack with the similar stacks reported in the literature	60
4.1. Explained x-axis of Fig. 4.9	85



## Outline of the Thesis

In the constantly evolving landscape of modern electronics, where the pursuit of enhanced performance and miniaturization has been the central driving force, Moore's law has served as a guiding principle. This empirical observation, suggesting that the quantity of transistors on an integrated circuit would roughly double every two year, has paved the way towards unparalleled computing capability [1]. While this observation held true for a significant part of the latter half of the 20th century, the relentless miniaturization of electronic components led this law to approach a state of saturation. To sustain the trajectory of Moore's law alternate pathways are being explored, among which the field of spintronics has emerged as a promising candidate. In the conventional electronics, which is based on transport of electric charge, the intrinsic spin property of electron is merely explored. The novel approach of including spin degree of freedom alongside with charge transport led to the emergence of the field of spin-transport based electronic or spintronics[2].

The field of spintronics emerges with the effects like giant magnetoresistance (GMR) [3,4] and tunneling magnetoresistance (TMR)[5,6] where experiments involved ferromagnetic metal (FM)/ normal-metal (NM) and FM/oxide heterostructures. GMR, recognized with a 2007 Nobel Prize, revolutionized magnetic read-head technology, and enhanced hard drive performance. Ever since the GMR and TMR discoveries, a significant amount of research has been done to understand the spin transport in magnetic material. Utilizing this knowledge, magnetic sensors and state-of-the art magnetic memory devices have already translated into the industrial products[7,8]. Among the conventional spintronics devices, magnetic random-access memory (MRAM) embodies the most advanced technology[9]. MRAM devices rely on magnetic tunnel junctions (MTJs)[10], which consist of two FM layers separated by a thin insulating tunnel barrier, serving as the bit cell (see Fig. 1) [11,12]. In MTJs, there are two FM layers: a magnetically fixed layer and a free layer whose magnetization is relatively easy to reorient. Manipulating the orientation of free layer is equivalent to writing a bit. A current application through MTJ will read this magnetization reorientation as a change in MTJ resistance. First generation MRAM were based on current induced Oersted field as a writing mechanism. However, it faced challenges with the down-scaling and reducing power consumption to align with the advanced technology requirements[11]. Instead of field, the second generation MRAM devices use current to switch the magnetization. These MRAM utilizes spin transfer torque (STT) mechanism to write a bit[13,14]. However, achieving fast



switching demands a significant current flow through the barrier layer in MTJs, expediting barrier degradation. The solution to this problem comes with the spin-orbit torque (SOT) mechanism[15]. In SOT, a heavy metal (HM) produces spin polarized current due to its high spin orbit coupling (SOC) energy. The spin current then interacts with the adjacent FM free layer and can switch the magnetization orientation[16-18]. This separation of writing and reading paths in SOT-MRAMs solve the barrier degradation problem of STT-MRAM.

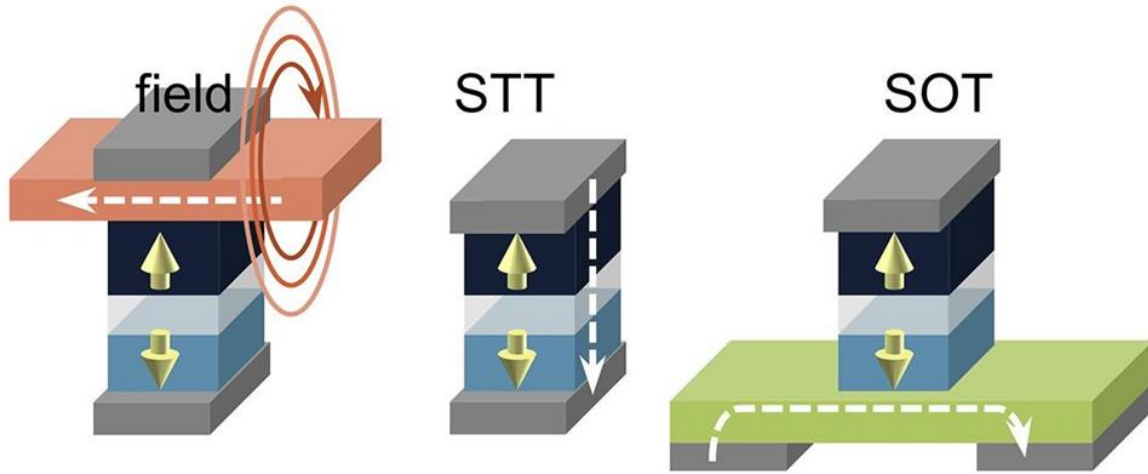


Figure 1. Schematic of mechanisms used for writing operation of information in a MTJ bit. From left to right these are: current generated magnetic field, STT, SOT, and motion of domain walls (DW) (Figure taken from Ref. [12])

In this dissertation, we examine the SOT mechanism, taking into account the magnetic orientation of Fm layer. Magnetization orientation depends on the magnetic anisotropy of the material which is a material parameter. The magnetic materials usually have an in-plane magnetic anisotropy (IMA) which favours the in-plane orientation of magnetization. Magnetization can be directed permanently towards out-of-plane direction under certain conditions. These conditions involve the perpendicular magnetic anisotropy (PMA) induced by interactions at film surface and interface with adjacent materials[19]. We characterized the SOT induced effective fields in both PMA and IMA based heterostructures. Moreover, our study also describes that the characterized SOT induced effective field can switch the magnetization orientation.

In our study, we adopted approaches that merge both fundamental principles and practical applications. Our investigation centers on HM/FM/HM model SOT devices. Employing transport measurement methodologies, we aim to deepen our understanding of magnetization

switching under the influence of SOT excitation. We introduce novel reading mechanisms to examine SOT-induced magnetization switching in both PMA and IMA-based devices. Notably, IMA and PMA devices exhibit distinct advantages stemming from variations in material deposition parameters and memory bit density. This research endeavors to unveil the fundamental mechanisms underpinning SOT-induced magnetization reversal within these magnetic heterostructures. Furthermore, through the utilization of transport measurement techniques and field-dependent symmetries, we demonstrate the phenomenon of multistate memory behavior in SOT switching in PMA-based devices. Prior to our investigation, this behavior had solely been examined in terms of material engineering. We tried to explore this based on transport measurements. Due to the non-volatile nature of SOT-based multistate memory, multistate SOT switching behavior has potential for its utilization in neuromorphic computing applications.

## Outline of the thesis

This thesis is organized in six chapters. Chapter 1 is dedicated to the introductory background which introduces spin-orbit coupling and its effects on magnetic heterostructures. Methods to convert charge into spin current (spin Hall effect, and Rashba effect), and magnetization dynamics in presence of spin orbit torques are also discussed in this part. Further, it also reviews the existing methodologies to characterize SOT and detect SOT induced magnetization switching. The remainder of this thesis is structured as follows:

- **Chapter 2: Experimental technique and room temperature transport measurements setup:**

In this chapter, we will describe the experimental techniques that are used to fabricate and characterize our magnetic heterostructure devices. Along with discussing the basic deposition and magnetic characterization techniques, we will discuss the details of our custom-built transport measurement system, utilizing which we performed all our transport experiments.

- **Chapter 3: Separation of Spin-orbit torque from thermoelectric effects and detection of SOT induced field-free magnetization switching in Pt/Co/Pt stack with Ta-underlayer utilizing thermoelectric effect**

SOT has two components, namely, antidamping-like (AD)-SOT and field-like (FL)-SOT. Here in this chapter, we discuss that Ta addition to the asymmetric stack (Pt/Co/Pt) gives rise to several compelling effects, viz., thermoelectric effects [particularly, anomalous Nernst effect (ANE)], and enhanced perpendicular magnetic anisotropy which was negligible in a Pt/Co/Pt stack. For this Ta/Pt/Co/Pt stack, the antidamping-SOT values are evaluated after carefully removing the contribution of the ANE and it is found to match the AD-SOT of the Pt/Co/Pt stack. We have observed current-induced field-free magnetization switching in Ta/Pt/Co/Pt stack with Co thickness gradient. Furthermore, we have utilized the thermoelectric effects to develop a technique to detect the field-free magnetization switching. This technique detects the second harmonic ANE signal as a reading mechanism. Using ANE symmetry with the applied current, the switching can be detected in a single current sweep which was corroborated to the conventional DC Hall method.

- **Chapter 4: Multistate memory behavior of SOT induced magnetization switching in presence of an external field**

In this chapter, we will explore the combined symmetry of SOT and DC field to stabilize multistate behavior. Further, we observe this behavior in Pt/Co/Pt stack which is one of the earliest model systems for PMA studies thereby expanding the potential applicability of our results. We verified that the integration of SOT with a static field yields multiple metastable saturation states, characterized by the magnitude and polarity of the static field. Furthermore, our finding suggests that this phenomenon is induced by both SOT and external field simultaneously. This effect enables the manipulation of energy barrier between states. At last, our measurements try to resolve the initialization problem of modern memristor devices through experimental demonstration of initialization-free multistate memory.

- **Chapter 5: Detection of in-plane magnetization switching using odd symmetry planar Hall effect**

In this chapter, we will demonstrate that the odd planar Hall voltage (O-PHV) signal exhibits an odd symmetry with the application of an external magnetic field which motivates us to develop a reading mechanism for detecting magnetization switching of in-plane magnetized heterostructures. We verified our DC-based reading mechanism in the Pt/Co/NiFe/Pt stack where a thin Co layer is inserted to create dissimilar interfaces about the NiFe layer. Remarkably, the current-induced in-plane fields are found to be significantly large in Pt/Co/NiFe/Pt stack. Furthermore, we employed the O-PHV method to detect the current-induced magnetization switching. The pure DC nature of the writing and reading mechanism of our proposed in-plane magnetization detection technique through O-PHV makes it the easiest one. Moreover, we show high repeatability and easy detection of our proposed method which will open avenues toward in-plane SOT switching based memory devices and sensors.

In the final chapter (Chapter 6) of this thesis, we will summarize the key findings and insights gained throughout this research journey. Additionally, we will identify and discuss few open questions within the field, paving the way for future investigations and advancements in this domain of study.

## References

- [1] R. R. Schaller, Moore's law: past, present and future, *IEEE Spectrum* **34**, 52 (1997).
- [2] I. Žutić, J. Fabian, and S. Das Sarma, Spintronics: Fundamentals and applications, *Reviews of Modern Physics* **76**, 323 (2004).
- [3] P. Grünberg, R. Schreiber, Y. Pang, M. B. Brodsky, and H. Sowers, Layered Magnetic Structures: Evidence for Antiferromagnetic Coupling of Fe Layers across Cr Interlayers, *Physical Review Letters* **57**, 2442 (1986).
- [4] M. N. Baibich, J. M. Broto, A. Fert, F. N. Van Dau, F. Petroff, P. Etienne, G. Creuzet, A. Friederich, and J. Chazelas, Giant Magnetoresistance of (001)Fe/(001)Cr Magnetic Superlattices, *Physical Review Letters* **61**, 2472 (1988).
- [5] J. S. Moodera, L. R. Kinder, T. M. Wong, and R. Meservey, Large Magnetoresistance at Room Temperature in Ferromagnetic Thin Film Tunnel Junctions, *Physical Review Letters* **74**, 3273 (1995).
- [6] W. H. Butler, X. G. Zhang, T. C. Schulthess, and J. M. MacLaren, Spin-dependent tunneling conductance of  $\mathrm{Fe}/\mathrm{MgO}/\mathrm{Fe}$  sandwiches, *Physical Review B* **63**, 054416 (2001).
- [7] S. Parkin, J. Xin, C. Kaiser, A. Panchula, K. Roche, and M. Samant, Magnetically engineered spintronic sensors and memory, *Proceedings of the IEEE* **91**, 661 (2003).
- [8] B. Dieny *et al.*, Opportunities and challenges for spintronics in the microelectronics industry, *Nature Electronics* **3**, 446 (2020).
- [9] S. Bhatti, R. Sbiaa, A. Hirohata, H. Ohno, S. Fukami, and S. N. Piramanayagam, Spintronics based random access memory: a review, *Materials Today* **20**, 530 (2017).
- [10] S. Tehrani, J. M. Slaughter, E. Chen, M. Durlam, J. Shi, and M. DeHerren, Progress and outlook for MRAM technology, *IEEE Transactions on Magnetics* **35**, 2814 (1999).
- [11] Z. Guo, J. Yin, Y. Bai, D. Zhu, K. Shi, G. Wang, K. Cao, and W. Zhao, Spintronics for Energy- Efficient Computing: An Overview and Outlook, *Proceedings of the IEEE* **109**, 1398 (2021).
- [12] V. Krizakova, M. Perumkunnil, S. Couet, P. Gambardella, and K. Garello, Spin-orbit torque switching of magnetic tunnel junctions for memory applications, *Journal of Magnetism and Magnetic Materials* **562**, 169692 (2022).

- [13] Y. J. A. b. Huai, Spin-transfer torque MRAM (STT-MRAM): Challenges and prospects, **18**, 33 (2008).
- [14] A. V. Khvalkovskiy *et al.*, Basic principles of STT-MRAM cell operation in memory arrays, *Journal of Physics D: Applied Physics* **46**, 074001 (2013).
- [15] Q. Shao *et al.*, Roadmap of Spin–Orbit Torques, *IEEE Transactions on Magnetism* **57**, 1 (2021).
- [16] L. Liu, C.-F. Pai, Y. Li, H. W. Tseng, D. C. Ralph, and R. A. Buhrman, Spin-Torque Switching with the Giant Spin Hall Effect of Tantalum, *Science* **336**, 555 (2012).
- [17] I. M. Miron *et al.*, Perpendicular switching of a single ferromagnetic layer induced by in-plane current injection, *Nature* **476**, 189 (2011).
- [18] K. Garello, C. O. Avci, I. M. Miron, M. Baumgartner, A. Ghosh, S. Auffret, O. Boulle, G. Gaudin, and P. Gambardella, Ultrafast magnetization switching by spin-orbit torques, *Applied Physics Letters* **105**, 212402 (2014).
- [19] M. T. Johnson, P. J. H. Bloemen, F. J. A. d. Broeder, and J. J. d. Vries, Magnetic anisotropy in metallic multilayers, *Reports on Progress in Physics* **59**, 1409 (1996).



# Chapter 1

## Introduction to the Basic Concepts

The main application of spintronics in magnetic storage technology comes from manipulating the magnetization of magnetic materials. However, before understanding the magnetization manipulation an understanding of magnetization orientation is must. In magnetic materials, magnetization has one preferential direction over other. This directional dependent property of magnetic materials is known as magnetic anisotropy.

### 1.1 Magnetic anisotropy

In magnetic materials, magnetization has preferred directions, with respect to a crystal axis or shape of materials, where it can align easily (easy axis) and where magnetization is hard to align (hard axis). This directional dependent property of magnetic materials is known as magnetic anisotropy. The contribution of anisotropy adds as an energy term in total energy functional of a magnetic material. This anisotropy energy defines as the energy difference of easy and hard axis of a magnetic material. The orientation of the easy magnetic axis results from a combination of various intrinsic and extrinsic factors. These contributions collectively define effective magnetic anisotropy of a material. For a ferromagnet, situated between two interfaces, a phenomenological model separating volume, surface/interface, and demagnetizing contribution of effective magnetic anisotropy ( $K_{\text{eff}}$ ) can be written as[1,2]:

$$K_{\text{eff}} = \frac{2K_s}{t} + K_V - 2\pi M_s^2 \quad (1.1)$$

$K_s$  is surface/interfacial contribution and  $K_V$  is volume contribution of effective anisotropy,  $t$  is magnetic layer thickness, and last term  $(-2\pi M_s^2)$  defines demagnetization energy or shape anisotropy.

The volume contribution comes from magnetocrystalline anisotropy which an intrinsic property of magnetic material. As the name suggests, magnetization has an easy direction



depending on their crystal structure. Magnetocrystalline anisotropy results from the spin-orbit interaction (SOI) and magnetocrystalline anisotropy energy depends on angle between magnetization and crystal structure defining easy axis. SOI couples spin momentum to orbital angular momentum. Additionally, the Coulomb interaction between electron orbitals and the crystal field, which arises from the periodic potential of the crystal lattice, defines certain orientations as energetically preferred.

Demagnetization or shape anisotropy contribution in the effective magnetic anisotropy is an outcome of minimization of magnetostatic energy. The magnetostatic energy is defined by:

$$E_u = -\frac{1}{2}\mu_0 \mathbf{M} \cdot \mathbf{H}_{demag} \quad (1.2)$$

Here,  $\mathbf{M}$  ( $=M_s \hat{m}$ ) is magnetization of ferromagnetic material along  $\hat{m}$ .  $H_{demag}$  is the demagnetization or stray field originated by magnetization in the ferromagnetic material and is given by:

$$\mathbf{H}_{demag} = -N\mathbf{M} \quad (1.3)$$

Here,  $N$  is called demagnetizing tensor. The demagnetization factors  $N_i$  ( $i=x,y,z$ ) for principal axis  $i$  for the case of a thin-film is:  $N_x = N_y = 0$ , and  $N_z = 1$  (considering  $x, y$  as in-plane axes, and  $z$  as out-of-plane axis to the thin film). Further, using Eq. (1.3), Eq. (1.2) can be modified as:

$$E_u = -\frac{1}{2}\mu_0 M_s^2 \cos^2 \theta \quad (1.4)$$

here  $\theta$  being the angle between thin film normal and magnetization. Eq. (1.4) states that magnetization direction in thin film plane is energetically more favored than magnetization out-of-plane. Therefore, thin films tend to favor an in-plane alignment of magnetization. In general, thin films with higher FM thickness shows in-plane magnetic anisotropy (IMA).

FM heterostructures with magnetization easy axis pointing along out-of-plane to the thin film have perpendicular magnetic anisotropy (PMA). In general, the FM thin films show IMA. However, it is evident from Eq. (1.1) that to make magnetization configuration out-of-film plane more favorable surface or interface contribution must be dominating. As the thickness of FM film decreased the significance of interfacial properties becomes increasingly pronounced (Fig. 1.1). This, consequently, amplify the surface anisotropy. This phenomenon, originally predicted by L. Néel in 1954 can be ascribed to alteration in symmetry at the interfaces. It was

earlier noted in Pt/Co/Pt [3] and Co/Pd [4] multilayer systems. The high SOI energy of heavy-metals (Pt, Pd etc.) and FM/HM interface effects benefits these systems. Enhanced surface anisotropy of HM/FM system have several possible sources. For instance, magnetostriction effect introduced from strains which is resulting from a lattice mismatch between adjacent elements[5]. Additionally, electron hybridization at the interfaces can also results in PMA [6].

It is evident from preceding section that PMA requires a rigorous optimization process. On the other hand, IMA based material stacks require lesser investment on the optimization process. However, high energy barrier at small device sizes makes PMA based material stack a prime candidate for high density memory application [7,8]. Hence, utilizing PMA based devices memory bit size can be reduce to nanometer range.

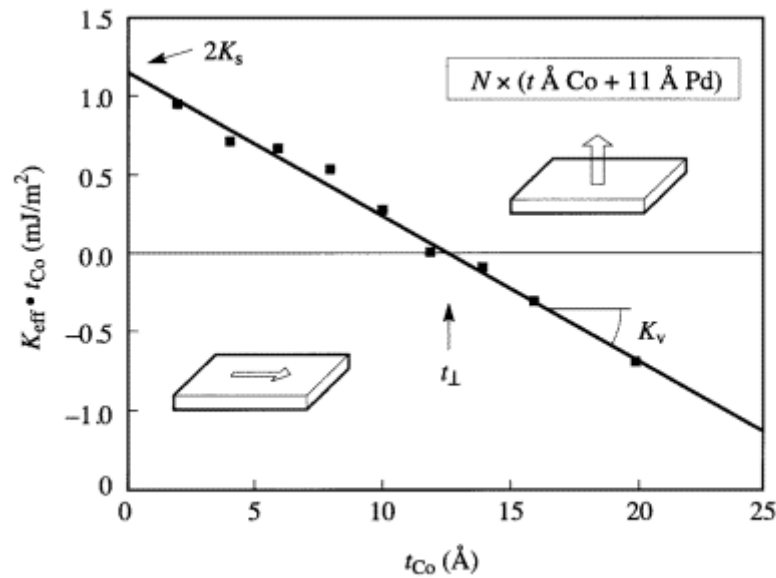


**Figure 1.1** FM thickness dependency of magnetic anisotropy in Pd/Co multilayer. This heterostructure shows a PMA behavior for Co thickness less than  $\sim 13$  Å [Figure source: Ref. [4]]

## 1.2 Manipulation of magnetization

Due to their non-volatile nature ferromagnet based heterostructures are prime candidate for memory application. Magnetic random-access memory (MRAM) based on FM heterostructure required writing a bit in terms of controlling FM magnetization orientation. Ferromagnetic magnetization aligns in certain directions depending upon IMA or PMA. To modify the

magnetic orientation between easy directions there are two major approaches: Magnetization controlled by magnetic field, and by current (scheme shown in Fig. 1.2).

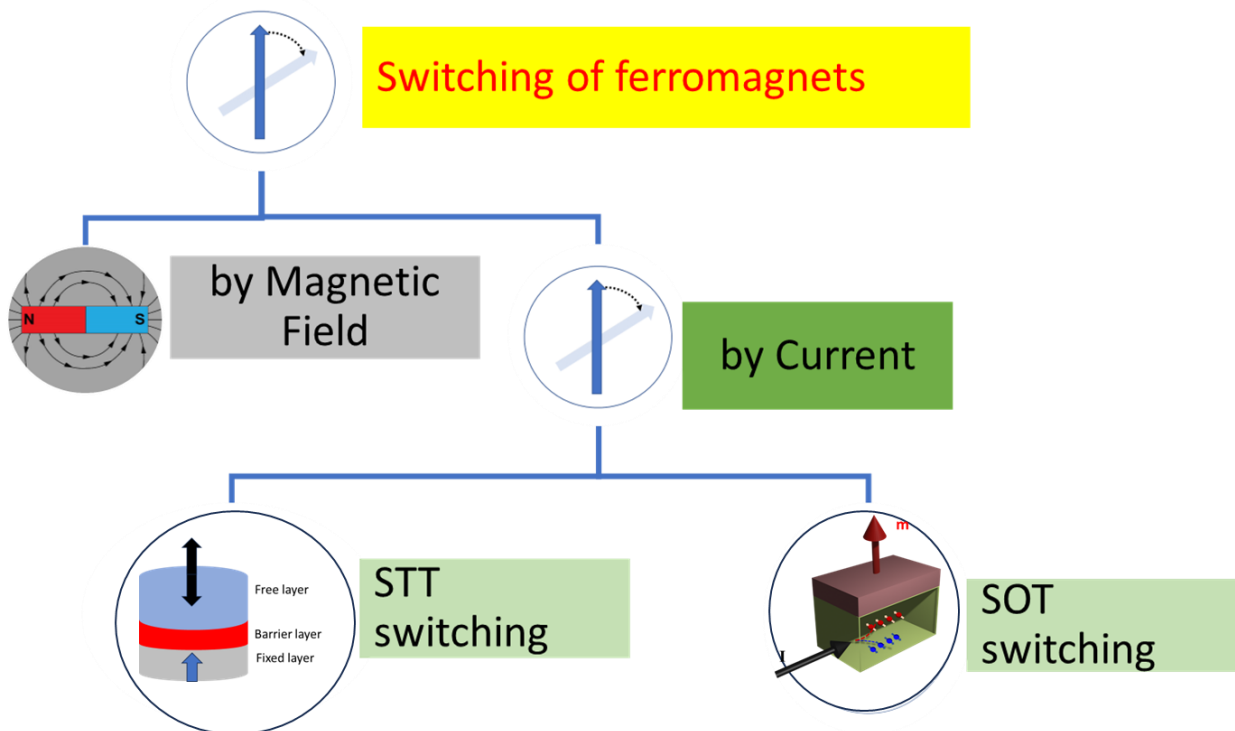


**Figure 1.2** Magnetization manipulation schemes.

### 1.2.1 Magnetic field

To control magnetization, one straight forward method is to employ a magnetic field. High enough magnetic results in saturation of magnetization along the magnetic field direction. Therefore, changing the direction magnetic field magnetization orientation can be changed in ferromagnetic materials. However, as the magnetic bit size reduces the magnetic field can interact with multiple bits. Additionally, reduced device size also requires higher magnetic field to control magnetization[9]. Hence, MRAM based on field-controlled writing mechanism suffers from scalability problem and are not energy efficient.

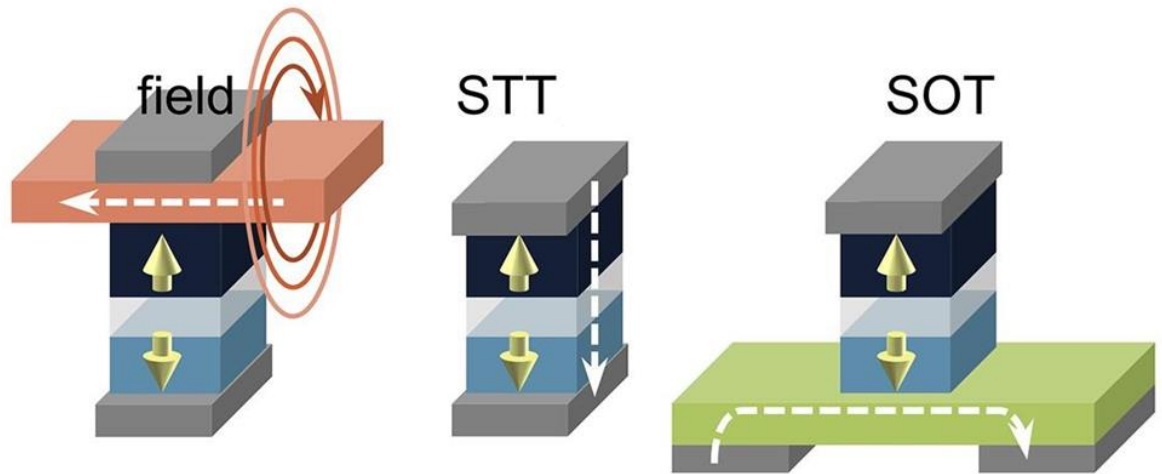


**Figure 1.3** Schematic of mechanisms used for writing operation of information in a MTJ bit. From left to right these are: current generated magnetic field, STT, SOT, and motion of domain walls (DW) (Figure taken from Ref. [10])

### 1.2.2 Current-controlled magnetization

In current-controlled mechanism, conduction current, carrying random spin orientations, converted into spin polarized current or spin current. This spin current interacts with the FM magnetization and applies torques on it. These torques can potentially switch the magnetization orientation of FM material. Current control of magnetization governs by two mechanisms (Shown in Fig 1.3):

- 1) Spin-transfer torque (STT) mechanism
- 2) Spin-orbit torque (SOT) mechanism

#### 1.2.2.1 Spin-transfer torque (STT) mechanism

Magnetic tunnel junctions (MTJs) are the building blocks of magnetic random access memory devices (MRAM)[11]. MTJ consists of two ferromagnetic layers separated by a thin barrier layer. Two magnetic layers are magnetically fixed and free, respectively. A memory bit is stored in terms of magnetization reorientation of free layer magnetization. In STT mechanism conduction electron drive the magnetization switching. It was theoretically predicted by Slonczewski et.al., in 1996 [12]. Current through MTJ polarize conduction current in the

direction of fix layer magnetization due to exchange interaction between conduction electrons and 3d electrons of fixed layer[13,14]. The polarised current or spin current then interact with free-layer magnetization. The transfer of angular momentum from spin current to free layer magnetization exert a torque on free layer magnetization and can eventually switch its magnetization and therefore, can store a bit.

STT mechanism overcomes the scalability issue of field-controlled devices, since here, the local application of current is limited to each MTJ cell only.

#### **1.2.2.2 Spin-orbit torque (SOT) mechanism**

The main drawback of STT mechanism is, applying a high magnitude current through MTJ to switch the free layer magnetization. Current through MJT propagates through thin barrier layer which degrade the device performance over the time and deteriorate the MRAM lifetime. To overcome this problem, in recent years, SOT mechanism is used to switch magnetization[15,16]. Due to their high spin-orbit coupling (SOC) energy of heavy metals (HM) like Ta, Pt, W etc., HMs can covert conduction current to spin polarised current. Therefore, in ferromagnetic (FM)/ heavy-metal (HM) heterostructures, an in-plane current through the HM layer converted into spin current and can flip the magnetic orientation of adjacent FM layer[17]. High spin-orbit coupling (SOC) energy of HM layer assist the accumulation of polarised spin at FM/HM interface. Various SOC phenomena that coverts charge current to spin current in SOT mechanism are discussed in latter section. In contrast to the STT mechanism, the SOT mechanism separates the writing path and reading path which therefore, solve the low endurance problem of STT based devices. This thesis is focused around the SOT mechanism.

### **1.3 Spin-orbit coupling and Charge to Spin conversion**

In SOT mechanism a charge current converted into spin current. This spin current applies SOTs on adjacent FM. Moreover, the spin currents are manifest of spin-orbit coupling (SOC) and inversion symmetry breaking. Therefore, before discussing SOTs in details an understanding of spin current generation is must and for that one has to understand the key role of SOC

interactions. Firstly, the SOC is briefly discussed followed by the mechanism that generates spin currents from charge current.

### 1.3.1 Spin-orbit Coupling

The origin of SOC is the relativistic interaction between electron spin moment with its orbital motion around the nucleus[18]. When an electron is in motion at relativistic velocities, an electric field appears as a magnetic field when observed from the electron's rest frame. It can be understood from the following relation:

$$\mathbf{B} = \frac{1}{c^2} (\mathbf{E} \times \mathbf{v}) \quad (1.5)$$

Here,  $c$  is the speed of light,  $\mathbf{B}$  is the magnetic field produced by an electron moving with a relativistic velocity  $\mathbf{v}$  in an electric field  $\mathbf{E}$ .

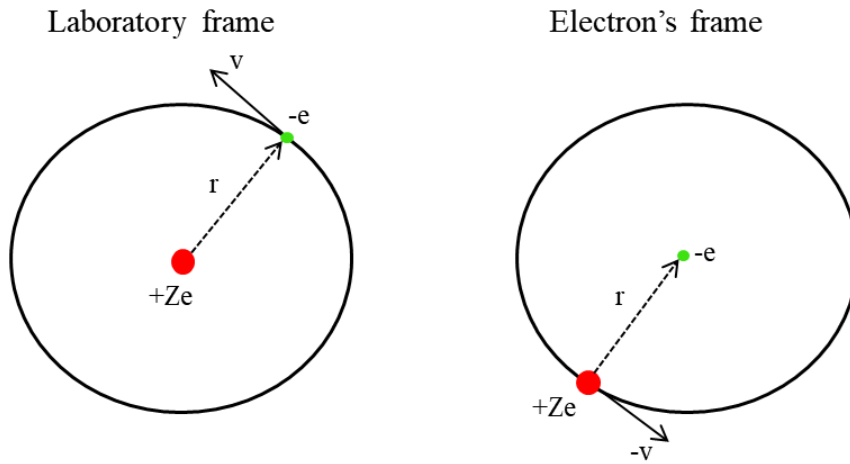


Figure 1.4 (a) motion of electron in around the nucleus in laboratory frame of reference. (b) relative motion of nucleus around electron in electron's frame of reference.

The SOC can be easily understood by the simplest model of hydrogen atom. Fig. 1.4 shows the illustration of an electron revolving about its nucleus. Both laboratory frame and electron's frame has been illustrated in Fig 1.4 (a) and (b), respectively. An electron with velocity  $\mathbf{v}$  revolves around nucleus while experiencing an electric field  $\mathbf{E} = \frac{1}{4\pi\epsilon_0} \left( \frac{Ze}{r^2} \right) \hat{\mathbf{r}}$ . Here,  $\mathbf{r} = r\hat{\mathbf{r}}$  are

the coordinate of electron orbit from nucleus. Therefore, according to Eq. (1.5), in the rest frame of electron a magnetic field is experienced by electron:

$$\mathbf{B} = \frac{1}{c^2} \frac{1}{4\pi\epsilon_0} \left( \frac{Ze}{r^2} \right) (\hat{\mathbf{r}} \times \mathbf{v}) = \frac{\mu_0}{4\pi} \left( \frac{Zev}{r^2} \right) \hat{\mathbf{z}} \quad (1.6)$$

The orbital angular momentum of electron is  $\mathbf{L} = m(\mathbf{r} \times \mathbf{v})$ . Where, m is electronic mass. Using the expression of angular momentum Eq. (1.6) can be written as:

$$\mathbf{B} = \frac{\mu_0}{4\pi} \frac{Ze}{m} \left( \frac{\mathbf{L}}{r^3} \right) \quad (1.7)$$

Similarly, the spin magnetic moment associated with electron spin is defined by

$$\boldsymbol{\mu}_s = -g_s \frac{e}{2m} \mathbf{S} \quad (1.8)$$

where  $g_s=2$ .

The energy of this interaction is defined as:  $E = -\boldsymbol{\mu}_s \cdot \mathbf{B}$ . This interaction energy can be expressed in terms of spin ( $\mathbf{S}$ ) and orbital ( $\mathbf{L}$ ) angular moment using Eq. (1.7) and Eq. (1.8).

$$E = \frac{\mu_0}{4\pi} \frac{e^2}{m} \left( \frac{Z}{r^3} \right) (\mathbf{S} \cdot \mathbf{L}) \quad (1.9)$$

Eq. (1.9) suggest that the relativistic interaction energy is due to the spin and orbital momentum coupling. Therefore, the interaction between electron spin and a magnetic field generated by the orbital motion of electron around its nucleus is called ‘spin-orbit interaction’ or ‘spin-orbit coupling (SOC).’

Throughout this thesis work, SOC becomes apparent through various effects that have been explored or employed. Some well-known examples of SOC-related phenomena include magneto-crystalline anisotropy, spin-orbit torques, spin current generation, planar Hall effect, and the anomalous Hall effect. In this section the role of SOC in the generation of spin polarised current has been discussed.

### 1.3.2 Charge current to spin current conversion

When a charge current flows through non-magnetic heavy-metals (HM), due to SOC interaction, conduction electrons undergo scattering events depending upon their spin polarization. These spin-dependent scattering events results in a spin current where conduction

electrons have a specific polarization. The polarization direction of spin current orients transversely to the charge current. Two underlying mechanisms that generate spin currents in HMs are: (a) Spin Hall effect (SHE), and (b) Rashba-Edelstein effect (REE). SHE is considered to be governing the scattering in the bulk of HM and therefore assigned as a bulk generated effect. However, REE is associated with the spin polarization at the HM interface and considered an interface effect.

### 1.3.2.1 Spin Hall effect (SHE)

The spin Hall effect (SHE) is a phenomenon observed in heavy-metals with strong SOC interactions[19-21]. This bulk originated effect converts a charge current into a spin current. SHE relies on SOC interaction and results from intrinsic as well as extrinsic mechanisms. The intrinsic mechanism is linked to the band structure and arises from the perturbation caused by spin-orbit coupling in electronic band structures. Whereas the extrinsic contributions are consequence of scattering from impurities, defects, surfaces, and interfaces. Further, extrinsic contributions are categorized into skew-scattering mechanism and side-jump mechanism.

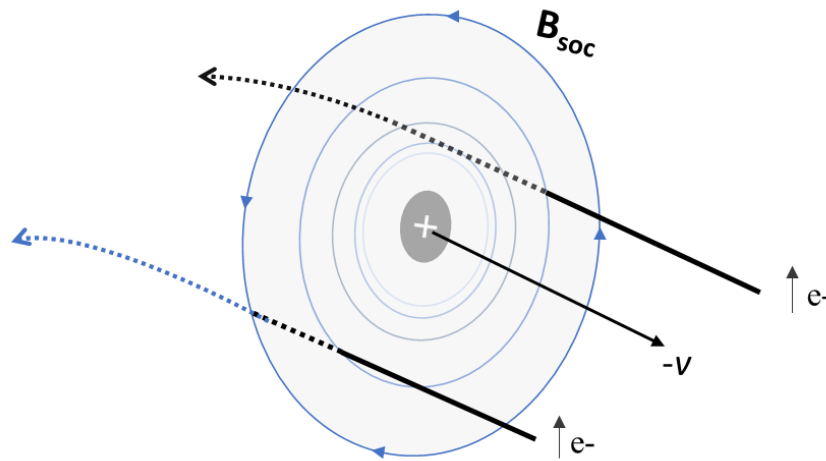


Figure 1.5 Skew scattering or Mott scattering mechanism illustrating the deflection of spin up electron due to magnetic field produced in electron's rest frame. [Modified illustration from Ref [22]]

Skew-scattering, also known as Mott effect, can be understood by analysing electron deflection in presence of electric field produced by impurity[22-24]. Due to SOC interaction, electric field



produced by impurities acts as a magnetic field in the rest frame of conduction electron. This magnetic field is similar to the Eq. (1.5). The magnetic field decreases as the distance between electron and nucleus increases. Therefore, the force ( $\mathbf{F}$ ) acting on spin ( $\mathbf{s}$ ) in this inhomogeneous magnetic field ( $F = \nabla(\mathbf{s} \cdot \mathbf{B})$ ) deflects the spin up and down along different directions. If spin is parallel to the magnetic field, then the direction of deflection is towards increasing field, however, if the spin and field are anti-parallel the conduction electron deflects towards decreasing field direction. This is illustrated in Fig 1.5 for the case of up spin. Therefore, up, and down spin are scattered along different directions.

Side-jump scattering is a quantum mechanical effect. The side jump effect emerges due to the anomalous velocity operator in spin-orbit coupled systems[25,26]. When impurity perturbations are introduced, scattering of free electron wave-packet (with wave vector  $\mathbf{k}$ ) gain a transverse component. It can be understood as a sideways spin dependent displacement of electron upon collision with an impurity [Fig. 1.6].

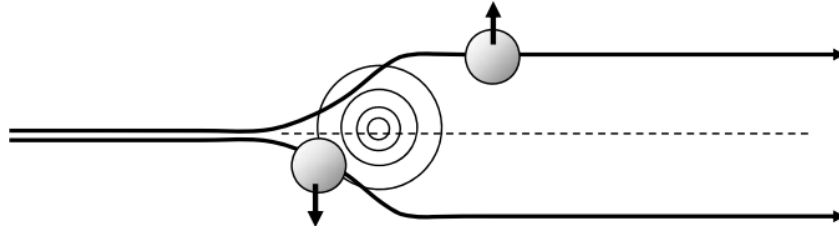


Figure 1.6 Illustration of side-jump scattering mechanism [Fig. from Ref [27]]

Hence, deflections of conduction electrons in high SOC materials show a spin dependency. In other words, an in-plane charge current deflects in HMs depending upon their spin orientation and accumulates of polarized spin takes place. The polarization of spin is transverse to charge current direction. This conversion of conduction electron flow to the polarized electron flow, i.e., spin current can be understood as:

$$\mathbf{j}_s = \frac{\hbar}{2e} \theta_{SH} (\boldsymbol{\sigma} \times \mathbf{j}_e) \quad (1.10)$$

Where  $\mathbf{j}_s$  is the spin current generated by the transport of a charge current  $\mathbf{j}_e$  and has spin polarization along  $\boldsymbol{\sigma}$ . Factor  $\theta_{SH}$  in Eq. (1.10) is known as spin Hall angle and describes the efficiency of charge to spin current conversion. The illustration of SHE generating a spin current mutually perpendicular to the current flow and spin polarization is depicted in Fig. 1.7.

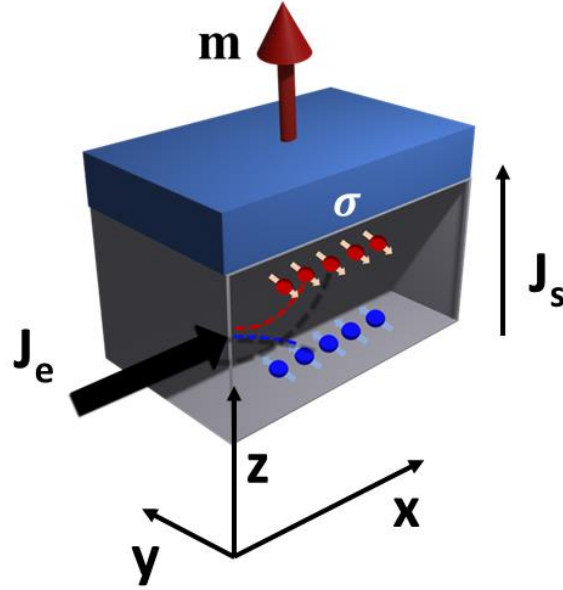


Figure 1.7 FM/HM heterostructure illustrating the generation of spin current in HM due to SHE.

### 1.3.2.2 Rashba-Edelstein effect (REE)

Rashba-Edelstein effect (REE) is considered to accumulate the polarized spin of conduction electron at the material interface[28,29]. The inversion symmetry breaking at the FM/HM interface, due to different work functions or inhomogeneous crystal fields from interfaces, leads to an electric field. The direction of this interface generated electric field is perpendicular to the interface. When an in-plane current applied along the interface, in the rest frame of conduction electron this electric field acts as a magnetic field as discussed in Eq. (1.5). This effective field induces a non-equilibrium spin accumulation at FM/HM interface. The effective field ( $\mathbf{B}_{REE}$ ) is given by:

$$\mathbf{B}_{REE} = \frac{1}{c^2} (\mathbf{E} \times \mathbf{v}) \quad (1.11)$$

Here, interface generated electric field is  $\mathbf{E} = E\hat{\mathbf{z}}$ , and  $\mathbf{v}$  is the velocity vector of conduction electron. Therefore, effective magnetic field is perpendicular to the wavevector  $\mathbf{k}$  of conduction electron and electric field direction  $\hat{\mathbf{z}}$ .

The interface generated electric field and SOC interaction defines the REE Hamiltonian as:

$$H_{REE} = \alpha_{REE} (\boldsymbol{\sigma} \times \mathbf{k}) \cdot \hat{\mathbf{z}} \quad (1.12)$$

Here  $\alpha_{REE}$  Rashba coupling constant which is a material dependent parameter. Further Eq. (1.12) describes the spin polarization, which is  $\mathbf{k}$ -vector dependent, in FM/HM interface as illustrated in FIG 1.8. This spin accumulation at the FM/HM interface interacts (s-d exchange interaction) with FM magnetization and induce spin torque.

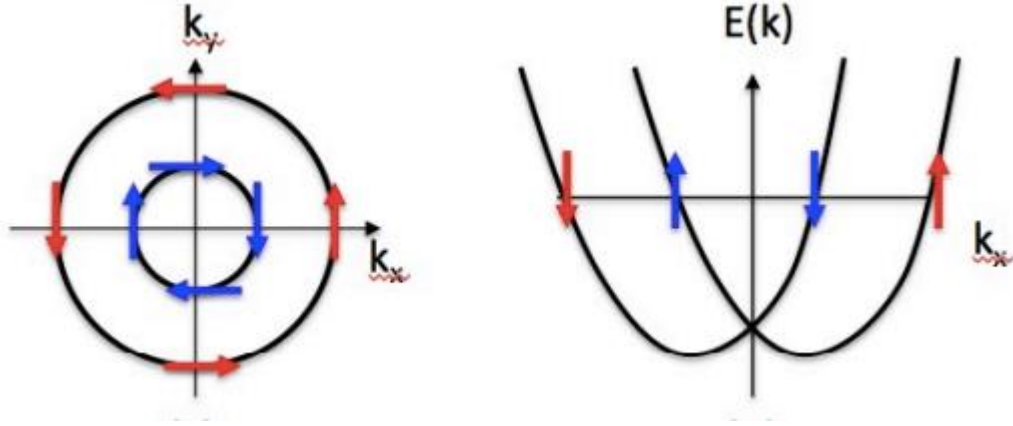


Figure 1.8 Illustration of 2D electron gas Fermi surface with Rashba coupling. [Figure from Ref [30]]

In conclusion, in-plane current through HM/FM heterostructures induces non-equilibrium spin accumulation by means of SHE and REE. This accumulation of polarized spins apply spin-orbit torques on the FM magnetization. As a possible outcome of these torque FM can switch its magnetic orientation.

## 1.4 SOT switching dynamics

The magnetization dynamics of magnetic materials is described by Landau-Lifshitz-Gilbert equation. An application of in-plane current through HM in FM/HM heterostructures exert spin-orbit torques (SOTs) on the FM magnetization. The SOT term in the LLG equation can be expressed as follows:

$$\frac{\partial \mathbf{M}}{\partial t} = -\gamma \mathbf{M} \times \mathbf{H}_{eff} + \frac{\alpha}{M_s} \mathbf{M} \times \frac{\partial \mathbf{M}}{\partial t} + a \mathbf{M} \times (\mathbf{M} \times \boldsymbol{\sigma}) + b \mathbf{M} \times \boldsymbol{\sigma} \quad (1.13)$$

Where:

- $\mathbf{M}$  is the magnetization of FM.

- $\gamma$  is the gyromagnetic ratio, a fundamental constant.
- $H$  is the effective magnetic field, which includes contributions from external fields, exchange interactions, and anisotropy.
- $\alpha$  is the Gilbert damping parameter, representing the energy dissipation term.
- $\sigma$  is the spin polarization direction.
- $a$ , and  $b$  are respective torque amplitudes.

The first term in the LLG equation accounts for the precession of the magnetic moment around the effective magnetic field. The second term is a phenomenological damping term that describes the dissipation of energy due to the interaction between the magnetic moment and its environment. Additional two terms introduced to account for the influence of spin-orbit torques (SOTs) on the magnetization dynamics. These terms are anti-damping-like (AD-SOT) and field-like SOT (FL-SOT), respectively (Fig. 1.9). In experiments, the AD-SOT and FL-SOT are extracted in terms of their effective fields.

AD-SOT is predominantly attributed to the SHE and expressed as[31]:

$$\tau_{AD} \propto M \times (M \times \sigma) \quad (1.13)$$

Consequently, the interaction between spin polarization ( $\sigma$ ) and FM magnetization occurs in a manner where a component of  $\sigma$ , which is perpendicular to  $M$ , applies a torque to  $M$ , aiming to rotate it towards  $\sigma$ . This is known as dephasing of polarized spin. Overall, spin currents generated by SHE induces a torque on FM magnetization that aligns the magnetization vector along the direction of the current. Similar to the field induced torques ( $\tau \propto M \times field$ ), AD-SOT can be written in terms an effective field induced by AD-SOT as:

$$\tau_{AD} \propto M \times H_{AD} \quad (1.14)$$

Here, AD-SOT effective field is:

$$H_{AD} \propto (M \times \sigma) \quad (1.15)$$

The constant of proportionality determines the scale of AD-SOT and, within the SHE framework, is expressed as:  $\frac{\theta_{SH}\hbar}{2eM_S t_{FM}} j$ . Where charge current through HM is  $j$ ,  $\theta_{SH}$  is spin-Hall angle, while the FM has thickness  $t_{FM}$  and saturation magnetization  $M_S$ .

For a charge current applied same as previously, the FL-SOT is expressed as:

$$\tau_{FL} \propto (M \times \sigma) \quad (1.16)$$

This torque term is a direct outcome of the spin accumulation at the interface between the FM and HM. Consequently, the FM magnetization precesses around the exchange field produced by spin accumulation  $\sigma$ . Given that the non-equilibrium spin accumulation is responsible for the FL-SOT, therefore, FL-SOT is considered as a manifestation of the REE[17,32]. Moreover, in experimental settings, the FL-SOT is determined in terms of its effective field, as expressed by:

$$H_{FL} \propto \sigma \quad (1.17)$$

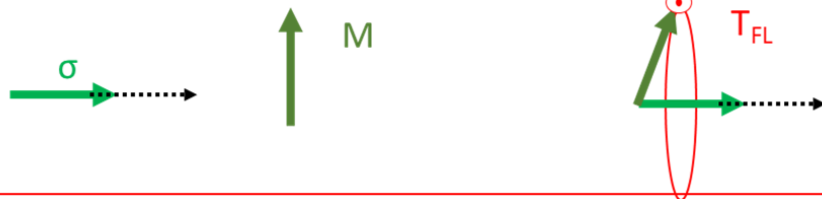
Where the direction of FL-SOT effective field is same as the direction of spin accumulation. In the upcoming sections of this thesis, it will become evident that in the Pt/Co/Pt system, the FL-SOT is negligible because of the symmetrical Co/Pt interface on both sides of the FM. Nevertheless, when the number of interfaces is increased, the influence of FL-SOT on magnetization dynamics becomes noticeable.

### AD Torque



Absorption of the transverse part of the spin current rotates **M** towards the direction of  $\sigma$ .

### FL Torque



Precession of **M** about the exchange field created by  $\sigma$ .

Figure 1.9 AD-SOT and FL-SOT affecting the magnetization dynamics in LLG equation.

In systems characterized by PMA and a structural composition of HM/FM, the reversal of magnetization is primarily driven by the AD-SOT. This conclusion is supported by the fact that experimental switching phase diagrams consistently align with explanations grounded in the AD-SOT term. Further, the field-like component is generally considered inconsequential in

metallic systems, largely as a result of the rapid dephasing of transverse spins, and it is generally disregarded.

## 1.5 Magnetization reversal by SOT

### 1.5.1 Macrospin

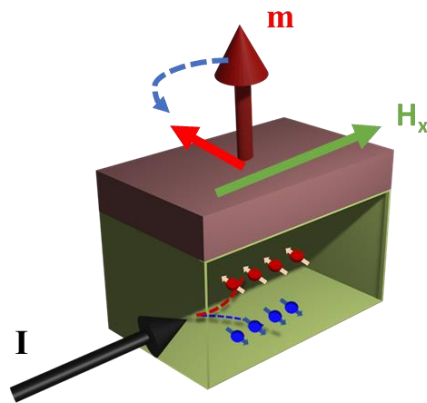


Figure 1.10 Schematic of macrospin picture illustrating the effect of SOT on FM magnetization.

In systems with PMA, deterministic bipolar switching is not achievable by SOTs alone. This limitation arises because the spin polarization ( $\sigma$ ) is oriented perpendicular to the easy-axis direction ( $z$ ), therefore, AD-SOT acting on FM magnetization ( $\mathbf{m}$ ), rotates  $\mathbf{m}$  in the  $xy$ -plane. From this in-plane orientation achieving  $\pm m_z$  state is equally probable or equal energy is required to reach both up and down magnetization states. Once the SOT is deactivated from this condition it results in a probabilistic switching of magnetization. To enable deterministic SOT-induced switching, a symmetry-breaking mechanism is essential (Fig. 1.10). Typically, this is provided by applying an in-plane magnetic field parallel or anti-parallel to the direction of the current[31]. It is important to note that the in-plane magnetic field itself does not favor specific magnetic orientations but effectively disrupts the symmetry in the magnetization's response to SOTs. Consequently, the combined influence of the in-plane current (governing

spin polarization via the spin Hall effect) and the magnetic field aligned with the current direction determines the magnetization orientation.

### 1.5.2 Domain dynamics

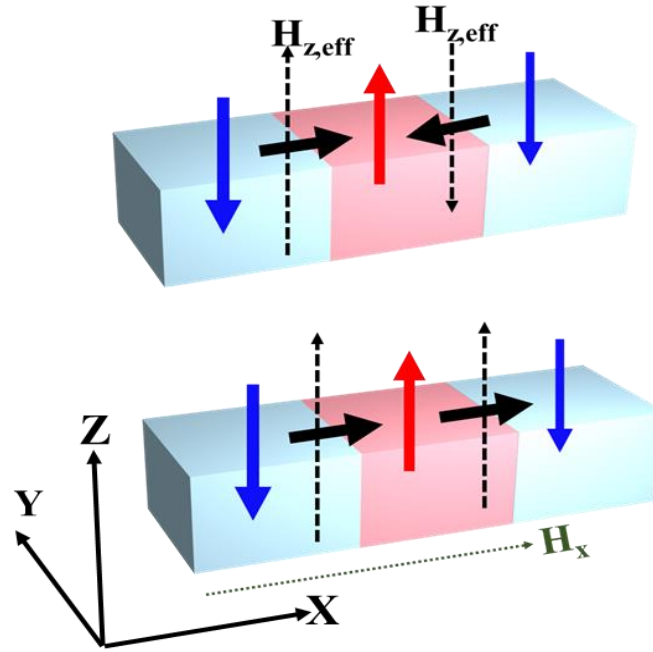


Figure 1.11 Effect of SOT on domain dynamics. The SOT effective field induces switching only in the presence of a symmetry breaking field.

In FM/HM heterostructures, Néel domain walls can stabilize, and SOT switching of magnetization occurs through domain wall dynamics. In FM/HM heterostructures, the presence of a strong spin-orbit coupling at the interface between the FM and HM layers leads to the emergence of the interfacial [33,34](DMI). DMI is an antisymmetric exchange interaction that favors non-collinear spin configurations. The interfacial DMI promotes different chiral structures including the formation of Néel domain walls in the FM layer. Néel domain walls are characterized by a 180-degree rotation of the magnetization direction across the domain wall, creating a non-collinear spin structure. The presence of Néel domain walls is energetically favorable due to the DMI. DMI stabilizes Néel domain walls by lowering their energy and

pinning them to the interface between the FM and HM layers. This pinning effect prevents the uncontrolled motion of Néel domain walls, ensuring their stability. In magnetic heterostructures with PMA, SHE-induced AD-SOT can drive Néel domain walls (DWs) in a manner similar to an out-of-plane applied field, with the direction of DW motion depending on the DW chirality[35,36]. The combination of current-induced magnetization switching and DW motion in HM/FM heterostructures can be explained by a scenario involving both the SHE and DMI. When a charge current ( $J_c$ ) flows along the x-axis in the HM layer of a magnetic heterostructure, it generates a transverse spin current ( $J_s$ ) along the z-axis through the SHE. This spin current injects spins into the FM layer with their spin polarization direction ( $\sigma$ ) parallel to the y-axis. In the presence of a Néel-type DW this spin current results in an effective field ( $H_{z,eff}$ ) through the AD-SOT mechanism. In a homochiral DW, the  $H_{z,eff}$  acting on the in-plane component of DW magnetization give rise to different polarity of  $H_{z,eff}$ . This effective field favours the propagation of certain domain. Therefore, in the case of homochiral Néel DWs,  $H_{z,eff}$  can induce DW motion, but it does not lead to domain expansion due to the opposite signs of  $H_{z,eff}$  for up-down and down-up DWs (Fig. 1.11). However, by applying a strong enough in-plane bias field ( $H_x$ ) to overcome the effective DMI field ( $H_{DMI}$ ), the DW moments in the Néel-type walls will realign parallel to  $H_x$  [36,37]. This reorientation of DW moments makes  $H_{z,eff}$  point in the same direction for both up-down and down-up walls, facilitating domain expansion or contraction depending on the polarities of  $J_c$  and  $H_x$  (Fig. 1.11). Consequently, both current-driven DW motion, magnetization switching, and out-of-plane field-driven switching processes involve significant roles played by the applied current  $J_c$  and in-plane bias field  $H_x$ .

### 1.5.3 Field-free magnetization switching

As the name suggest, field-free magnetization switching by SOT refers to a process where the magnetization of a FM is switched without the application of an external magnetic field. An in-plane symmetry breaking field is generated to exclude the requirement of any external symmetry breaking field. Several methods enable field-free SOT switching in spintronic devices. One such approach involves the use of an antiferromagnetic layer placed adjacent to the magnetic layer[38]. The exchange coupling between these layers generates an effective magnetic field that assists the SOT switching process. Alternatively, magnetic layer with tilted anisotropy results in the creation of an effective magnetic field that favors field-free SOT switching[39]. Another method is to introduce broken lateral inversion symmetry in the



magnetic layer, which generates an effective magnetic field to assist in SOT switching[40]. These techniques leverage the internal properties and interactions of the materials and device structures, eliminating the need for an external magnetic field in the SOT switching process.

### 1.5.4 Experimental realization

Magnetization reversal experiments are generally conducted in a Hall bar device of FM/HM heterostructures. The Hall bar device is a common platform for such experiments because it allows for the generation and detection of spin currents and Hall voltages, making it well-suited for studying SOT-induced effects. The magnetization of the FM layer within the Hall bar device is set to an initial state, typically aligned in a specific direction. Further, A short-duration, high-amplitude current pulse is applied to the device (schematic shown in Fig. 1.12), generating a spin current due to the SHE in the HM layer. This spin current exerts SOTs on the FM layer, which can eventually flip the magnetization orientation. Current pulses enable rapid switching of the magnetization, making SOT-based devices potentially faster and more energy-efficient compared to traditional methods that rely solely on external magnetic fields. This is particularly advantageous for applications in data storage and computing. However, the application of current pulses in SOT switching experiments can have safety considerations. A high-duration pulse of electrical current can potentially damage or even burst a device due to the heat generated during the pulse.

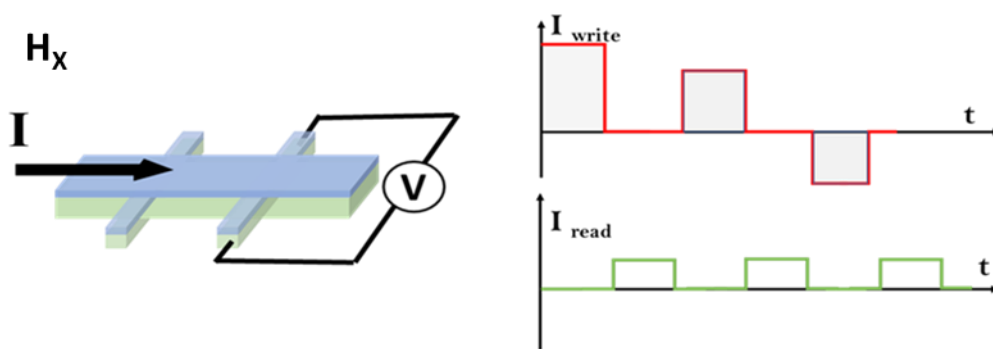


Figure 1.12 Experimental method to perform SOT induce magnetization switching involve short duration current pulses followed by a reading mechanism.

In summary, current pulses are applied in SOT switching experiments to generate spin currents and efficiently manipulate the magnetization of FM/HM heterostructures.

## 1.6 Reading the magnetization reorientation

In SOT memory, the encoding of a memory bit revolves around the manipulation of different magnetic states within an FM/HM heterostructure. So far, we have understood that to write a bit, the application of SOT current pulses with appropriate polarities is a requirement. Nevertheless, for a comprehensive memory system, there is a need for a reading mechanism that can discern the magnetic orientation post each writing pulse. In Hall bar devices consisting of FM/HM heterostructures, the Hall voltage serves as the method for detecting magnetization reorientation.

The Hall voltage have the following form[41]:

$$V_H = \left(\frac{R_H I}{t}\right) \cos(\alpha) + \left(\frac{\mu_0 R_S I}{t}\right) M \cos(\theta) + \left(\frac{k I}{t}\right) M^2 \sin^2(\theta) \sin 2\phi \quad (1.18)$$

Here, these three terms are ordinary Hall effect (OHE), anomalous Hall effect (AHE), and planar hall effect (PHE) voltages, respectively.

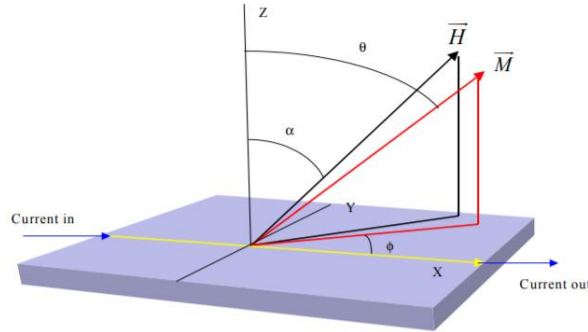


Figure 1.13 Coordinate geometry defining magnetization and magnetic field. [Figure taken from Ref [41]]

The OHE is a well-understood phenomenon that occurs when a current flows through a conductor in the presence of an external magnetic field perpendicular to the current direction. It results in a transverse voltage (Hall voltage) being generated across the conductor. The OHE voltage is caused by the Lorentz force acting on charge carriers as they move through the magnetic field.

The AHE and PHE are additional contribution to the Hall voltage that are not explained solely by the OHE mechanism. It occurs in ferromagnetic materials and is often associated with the SOC coupling of charge carriers. This interaction leads to a complex contribution to the Hall voltage that is related to the magnetization of the material. AHE and PHE results in the accumulation of spins with opposite orientations at diametrically opposite boundaries, which leads to a net transverse voltage, known as an anomalous Hall voltage. Unlike the SHE, which occurs in non-magnetic materials, the AHE in FMs is a consequence of the unique exchange-split band structure with a net spin polarization at the Fermi level, generating spin-polarized charge currents. The presence of external magnetic fields is not required for the AHE, and it arises from the interaction between conduction electrons and local potentials created by defects or impurities within the material. In contrast, the SHE is characterized by the accumulation of spins at lateral boundaries of a current-carrying conductor, generating a transverse spin current with spin polarization perpendicular to the plane defined by a charge and a spin current. The AHE is primarily characterized by the transverse voltage generated perpendicular to the charge current and the magnetization direction within FMs. Further, AHE and PHE are both Hall phenomena observed in magnetic materials but are distinguished by their characteristic voltage generation orientations. AHE is primarily associated with the transverse voltage generated perpendicular to the magnetization direction, resulting from the accumulation of spins with opposite orientations at opposite boundaries. In contrast, PHE is characterized by voltage generation within the plane of the material, parallel to the direction of charge and spin currents, and is sensitive to in-plane magnetization variations. Therefore, AHE and PHE differ not only in terms of their voltage orientation but also in the underlying magnetic configurations they are associated with, making them distinct manifestations of the Hall effect in magnetic materials.

OHE contribution is negligible in metallic FM/HM heterostructures as compare to AHE and PHE contribution. Comparing each component of Eq. (1.18) with Fig. (1.13) that AHE voltage is proportional to z-component of magnetization and PHE is proportional to the multiplication of in-plane magnetization components.

$$V_{\text{AHE}} \propto m_z$$

$$V_{\text{PHE}} \propto m_x m_y$$

In PMA-based heterostructures, where the energy-minimized states are predominantly corresponded to  $\pm m_z$ , the contribution of the PHE is nearly negligible, in addition to the

presence of the OHE. Consequently, the measured Hall voltage primarily comprises the AHE voltage contribution. As AHE is proportional to z-component of magnetization, this is particularly useful for reading the magnetization orientation in PMA-based material stacks, serving as an effective reading mechanism.

In the case of in-plane magnetic material or heterostructures with in-plane magnetic anisotropy (IMA) the third term of Eq. (1.18) dominates. However, the magnetization reorientation cannot directly be probed by PHE due to its even dependency on magnetization. One of the objectives of this thesis is to probe the SOT switching of magnetization in IMA based heterostructures. This thesis addresses the problem Hall voltage-based reading mechanism for IMA based devices and gives a method to probe the magnetization switching in them.

In the case of in-plane magnetic materials or heterostructures exhibiting in-plane magnetic anisotropy (IMA), the third term in Eq. (1.18) dominates. However, the direct assessment of magnetization reorientation via the Planar Hall Effect (PHE) is hindered by its even dependence on magnetization. One of the objectives of this thesis is investigation of SOT magnetization switching in IMA-based heterostructures. Furthermore, the thesis addresses the challenge of developing a Hall voltage-based reading mechanism for IMA-based devices and presents an innovative methodology for probing magnetization switching within this context.

## 1.7 Characterization of Spin-orbit torques

To characterize SOT in FM/HM heterostructures, second harmonic Hall measurements are employed. In these magnetic heterostructures, Hall resistance is described by the following equation:

$$R_{XY} = \Delta R_{AHE} \cos\theta + \Delta R_{PHE} \sin^2\theta \sin 2\varphi \quad (1.19)$$

Here,  $\Delta R_{AHE}$  and  $\Delta R_{PHE}$  represent the AHE and PHE resistances, respectively, and the magnetization is defined by coordinates  $(\theta, \varphi)$ . A current along x-axis generates a transverse Hall signal that is described by Eq. (1.19). When a current flows along the x-axis, it induces SOT on the magnetization ( $\mathbf{m}$ ), attempting to alter its orientation from the initial position  $(\theta_0, \varphi_0)$ .

In other words,  $\theta \rightarrow \theta_0 + \Delta\theta$ ,  $\varphi \rightarrow \varphi_0 + \Delta\varphi$

When a low-frequency AC current is applied to the FM/HM heterostructure, the magnetization ( $m$ ) begins to oscillate at the same frequency as the applied current. The frequency is deliberately kept low to ensure that the current and magnetization oscillations remain in phase.

If the applied current is:  $I_{ac} = I_0 \sin \omega t$  (1.20)

Then, the oscillation in the change of magnetization due to SOT takes the form:

$$\left. \begin{aligned} \Delta \theta &\rightarrow \Delta \theta \sin \omega t \\ \Delta \varphi &\rightarrow \Delta \varphi \sin \omega t \end{aligned} \right\} \quad (1.21)$$

This oscillation in magnetization due to SOT modifies Eq. (1.19) to introduce  $\sin(\omega t)$  terms, as a consequence of Eq. (1.21) within Eq. (1.19).

Now, as the Hall voltage is given by:  $V_{xy} = R_{xy} I_{ac}$ , the modified Eq. (1.19) and Eq. (1.20) result in the multiplication of  $\sin(\omega t)$  terms that can be converted into  $\cos(2\omega t)$ .

Consequently, the Hall voltage can be expressed in a more general form[42]:

$$V_{XY} = V_0 + V_{\omega} \sin \omega t + V_{2\omega} \cos 2\omega t \quad (1.22)$$

From Eq. (1.22), it becomes evident that the SOT-induced oscillation of magnetization by an AC current lead to a second harmonic signal. Therefore, it is intuitive that the characterization of SOT necessitates the use of second harmonic Hall measurements.

### 1.7.1 Harmonic Hall method to characterize SOT

In PMA based materials, low field harmonic Hall technique is widely used to probe both AD-SOT and FL-SOT. In the experimental setup, an external magnetic field, along current direction ( $H_x$ ) or transverse to it ( $H_y$ ), is applied to the Hall bar. The response of the first ( $V_{\omega}$ ) and second harmonic ( $V_{2\omega}$ ) Hall voltage to these applied conditions is measured. A standard lock-in amplifier proves to be the most efficient method for generating and detecting the AC signal. The systematic variation of  $H_x$  and  $H_y$ , provides a varying Hall voltage response. The analysis of Hall voltage by Eq. (1.23) provides longitudinal and transverse effective fields induced by AD-SOT ( $H_{AD}$ ) and FL-SOT ( $H_{FL}$ ), respectively[42].

$$H_{AD,FL} = -2 \frac{(B_{X,Y} \pm 2\xi B_{Y,X})}{1-4\xi^2} \quad (1.23)$$

Where,  $B_{x,y} = \frac{(\partial V_{2\omega} / \partial H_{x(y)})}{(\partial^2 V_{\omega} / \partial H_{x(y)}^2)}$ , and  $\xi = \frac{\Delta R_{PHE}}{\Delta R_{AHE}}$ .

### 1.7.2 Thermoelectric effects

Low field harmonic method discussed above is amongst the easiest method to characterize the SOTs. However, this method does not discuss about thermoelectric effect. The quantification of thermoelectric effects become important in second harmonic Hall characterization due to their dependency on Joule heating. Joule heating is produced by charge current in the samples and has a quadratic dependency on injected current (Fig. 1.14).

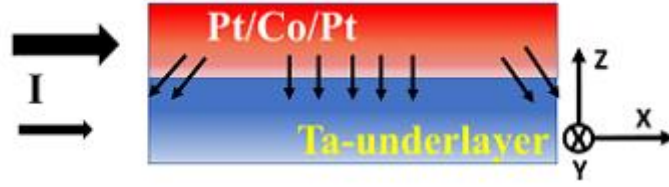


Figure 1.14 Heat gradient produced due to resistivity differences of different layers.

i.e., current induced Joule heating generates a temperature gradient as:  $\nabla T \propto I^2$

In the case applied ac current ( $I_{AC} = I_0 \sin \omega t$ ) the heat gradient  $\nabla T$  takes the following form[43,44]:

$$\nabla T \propto I_{AC}^2 = (I_0 \sin \omega t)^2 = \frac{I_0^2}{2} (1 - \cos 2\omega t) \quad (1.24)$$

Thermal gradients of this nature can lead to the occurrence of the anomalous Nernst effect (ANE). ANE is a thermal counterpart of anomalous Hall effect, driven by a heat gradient. This heat driven ANE signal have following second harmonic form[43]:

$$V^{2\omega, ANE} \propto (m \times \nabla T) \quad (1.25)$$

Here, the proportionality sign can be replaced by a substituted with a material-specific ANE coefficient. Notably, ANE has a magnetization dependency similar to AD-SOT effective field. Consequently, accurately quantifying ANE from AD-SOT becomes essential to prevent the overestimation of SOT fields.

After exploring the angular dependency of different SOT fields, the second harmonic Hall resistance can be written as[44]:

$$R_{xy}^{2\omega} = \left[ \left( -R_{AHE} \frac{H_{AD}}{H_{ext} - H_k} + R_{VT} \right) \cos\varphi + 2R_{PHE} (2\cos^3\varphi - \cos\varphi) \frac{H_{FL} + H_{Oe}}{H_{ext}} \right] \quad (1.26)$$

Equation (1.26) also serves as a means to measure the SOT effective field, in addition to detecting the thermoelectric effect. This approach necessitates either an angular sweep at a fixed field or a field sweep at a fixed angular value.

## References

- [1] S. Bandiera, R. C. Sousa, B. Rodmacq, and B. Dieny, Asymmetric Interfacial Perpendicular Magnetic Anisotropy in Pt/Co/Pt Trilayers, *IEEE Magnetics Letters* **2**, 3000504 (2011).
- [2] R. Jungblut, M. T. Johnson, J. aan de Stegge, A. Reinders, and F. J. A. den Broeder, Orientational and structural dependence of magnetic anisotropy of Cu/Ni/Cu sandwiches: Misfit interface anisotropy, *Journal of Applied Physics* **75**, 6424 (1994).
- [3] F. J. A. den Broeder, W. Hoving, and P. J. H. Bloemen, Magnetic anisotropy of multilayers, *Journal of Magnetism and Magnetic Materials* **93**, 562 (1991).
- [4] M. T. Johnson, P. J. H. Bloemen, F. J. A. d. Broeder, and J. J. d. Vries, Magnetic anisotropy in metallic multilayers, *Reports on Progress in Physics* **59**, 1409 (1996).
- [5] M. T. Johnson, R. Jungblut, P. J. Kelly, and F. J. A. den Broeder, Perpendicular magnetic anisotropy of multilayers: recent insights, *Journal of Magnetism and Magnetic Materials* **148**, 118 (1995).
- [6] G. H. O. Daalderop, P. J. Kelly, and M. F. H. Schuurmans, Magnetic anisotropy of a free-standing Co monolayer and of multilayers which contain Co monolayers, *Physical Review B* **50**, 9989 (1994).
- [7] K. Garello, C. O. Avci, I. M. Miron, M. Baumgartner, A. Ghosh, S. Auffret, O. Boulle, G. Gaudin, and P. Gambardella, Ultrafast magnetization switching by spin-orbit torques, *Applied Physics Letters* **105**, 212402 (2014).
- [8] B. Dieny and M. Chshiev, Perpendicular magnetic anisotropy at transition metal/oxide interfaces and applications, *Reviews of Modern Physics* **89**, 025008 (2017).
- [9] P. K. Amiri *et al.*, Electric-field-controlled magnetoelectric RAM: Progress, challenges, and scaling, **51**, 1 (2015).
- [10] V. Krizakova, M. Perumkunnil, S. Couet, P. Gambardella, and K. Garello, Spin-orbit torque switching of magnetic tunnel junctions for memory applications, *Journal of Magnetism and Magnetic Materials* **562**, 169692 (2022).
- [11] J.-G. Zhu and C. Park, Magnetic tunnel junctions, *Materials Today* **9**, 36 (2006).
- [12] J. C. Slonczewski, Current-driven excitation of magnetic multilayers, *Journal of Magnetism and Magnetic Materials* **159**, L1 (1996).
- [13] Y. J. A. b. Huai, Spin-transfer torque MRAM (STT-MRAM): Challenges and prospects, **18**, 33 (2008).
- [14] Y. Zhang, X. Wang, Y. Li, A. K. Jones, and Y. Chen, in *2012 Design, Automation & Test in Europe Conference & Exhibition (DATE)2012*, pp. 1313.
- [15] J. Ryu, S. Lee, K.-J. Lee, and B.-G. Park, Current-Induced Spin–Orbit Torques for Spintronic Applications, *Advanced Materials* **32**, 1907148 (2020).
- [16] Q. Shao *et al.*, Roadmap of Spin–Orbit Torques, *IEEE Transactions on Magnetism* **57**, 1 (2021).
- [17] R. Posti, A. Kumar, D. Tiwari, and D. Roy, Emergence of considerable thermoelectric effect due to the addition of an underlayer in Pt/Co/Pt stack and its application in detecting field free magnetization switching, *Applied Physics Letters* **121**, 223502 (2022).
- [18] B. H. Bransden and C. J. Joachain, *Physics of atoms and molecules* (Pearson Education India, 2003).
- [19] J. Sinova, S. O. Valenzuela, J. Wunderlich, C. H. Back, and T. Jungwirth, Spin Hall effects, *Reviews of Modern Physics* **87**, 1213 (2015).
- [20] J. E. Hirsch, Spin Hall Effect, *Physical Review Letters* **83**, 1834 (1999).



- 
- [21] Y. K. Kato, R. C. Myers, A. C. Gossard, and D. D. Awschalom, Observation of the Spin Hall Effect in Semiconductors, *Science* **306**, 1910 (2004).
- [22] J. Stöhr and H. C. J. S.-S. S. S. Siegmann, Berlin, Heidelberg, *Magnetism*, **5**, 236 (2006).
- [23] A. Ferreira, T. G. Rappoport, M. A. Cazalilla, and A. H. Castro Neto, Extrinsic Spin Hall Effect Induced by Resonant Skew Scattering in Graphene, *Physical Review Letters* **112**, 066601 (2014).
- [24] M. Gradhand, D. V. Fedorov, P. Zahn, and I. Mertig, Extrinsic Spin Hall Effect from First Principles, *Physical Review Letters* **104**, 186403 (2010).
- [25] P. Laczkowski *et al.*, Large enhancement of the spin Hall effect in Au by side-jump scattering on Ta impurities, *Physical Review B* **96**, 140405 (2017).
- [26] D. Culcer, E. M. Hankiewicz, G. Vignale, and R. Winkler, Side jumps in the spin Hall effect: Construction of the Boltzmann collision integral, *Physical Review B* **81**, 125332 (2010).
- [27] N. Nagaosa, J. Sinova, S. Onoda, A. H. MacDonald, and N. P. Ong, Anomalous Hall effect, *Reviews of Modern Physics* **82**, 1539 (2010).
- [28] T. S. Ghiasi, A. A. Kaverzin, P. J. Blah, and B. J. van Wees, Charge-to-Spin Conversion by the Rashba–Edelstein Effect in Two-Dimensional van der Waals Heterostructures up to Room Temperature, *Nano Letters* **19**, 5959 (2019).
- [29] Q. Shao *et al.*, Strong Rashba-Edelstein Effect-Induced Spin–Orbit Torques in Monolayer Transition Metal Dichalcogenide/Ferromagnet Bilayers, *Nano Letters* **16**, 7514 (2016).
- [30] A. Manchon, H. C. Koo, J. Nitta, S. M. Frolov, and R. A. Duine, New perspectives for Rashba spin–orbit coupling, *Nature Materials* **14**, 871 (2015).
- [31] L. Liu, O. J. Lee, T. J. Gudmundsen, D. C. Ralph, and R. A. Buhrman, Current-Induced Switching of Perpendicularly Magnetized Magnetic Layers Using Spin Torque from the Spin Hall Effect, *Physical Review Letters* **109**, 096602 (2012).
- [32] H. An, H. Nakayama, Y. Kanno, A. Nomura, S. Haku, and K. Ando, Spin-orbit torques in asymmetric Pt/Co/Pt structures, *Physical Review B* **94**, 214417 (2016).
- [33] A. Hrabec, N. A. Porter, A. Wells, M. J. Benitez, G. Burnell, S. McVitie, D. McGrouther, T. A. Moore, and C. H. Marrows, Measuring and tailoring the Dzyaloshinskii–Moriya interaction in perpendicularly magnetized thin films, *Physical Review B* **90**, 020402 (2014).
- [34] J. Cho *et al.*, Thickness dependence of the interfacial Dzyaloshinskii–Moriya interaction in inversion symmetry broken systems, *Nature Communications* **6**, 7635 (2015).
- [35] O. J. Lee, L. Q. Liu, C. F. Pai, Y. Li, H. W. Tseng, P. G. Gowtham, J. P. Park, D. C. Ralph, and R. A. Buhrman, Central role of domain wall depinning for perpendicular magnetization switching driven by spin torque from the spin Hall effect, *Physical Review B* **89**, 024418 (2014).
- [36] C.-F. Pai, M. Mann, A. J. Tan, and G. S. D. Beach, Determination of spin torque efficiencies in heterostructures with perpendicular magnetic anisotropy, *Physical Review B* **93**, 144409 (2016).
- [37] T.-Y. Chen, W.-B. Liao, T.-Y. Chen, T.-Y. Tsai, C.-W. Peng, and C.-F. Pai, Current-induced spin–orbit torque efficiencies in W/Pt/Co/Pt heterostructures, *Applied Physics Letters* **116**, 072405 (2020).
- [38] S. Fukami, C. Zhang, S. DuttaGupta, A. Kurenkov, and H. Ohno, Magnetization switching by spin–orbit torque in an antiferromagnet–ferromagnet bilayer system, *Nature Materials* **15**, 535 (2016).
-

- [39] V. M. P, K. R. Ganesh, and P. S. A. Kumar, Spin Hall effect mediated current-induced deterministic switching in all-metallic perpendicularly magnetized Pt/Co/Pt trilayers, *Physical Review B* **96**, 104412 (2017).
- [40] G. Yu *et al.*, Switching of perpendicular magnetization by spin–orbit torques in the absence of external magnetic fields, *Nature Nanotechnology* **9**, 548 (2014).
- [41] J. R. Lindemuth and B. C. Dodrill, Anomalous Hall effect magnetometry studies of magnetization processes of thin films, *Journal of Magnetism and Magnetic Materials* **272-276**, 2324 (2004).
- [42] M. Hayashi, J. Kim, M. Yamanouchi, and H. Ohno, Quantitative characterization of the spin-orbit torque using harmonic Hall voltage measurements, *Physical Review B* **89**, 144425 (2014).
- [43] C. O. Avci, K. Garello, A. Ghosh, M. Gabureac, S. F. Alvarado, and P. Gambardella, Unidirectional spin Hall magnetoresistance in ferromagnet/normal metal bilayers, *Nature Physics* **11**, 570 (2015).
- [44] C. O. Avci, K. Garello, M. Gabureac, A. Ghosh, A. Fuhrer, S. F. Alvarado, and P. Gambardella, Interplay of spin-orbit torque and thermoelectric effects in ferromagnet/normal-metal bilayers, *Physical Review B* **90**, 224427 (2014).



## Chapter 2

### Experimental technique and room temperature transport measurements setup

Within this chapter, a comprehensive exploration of diverse techniques and instruments employed in various experiments is provided. The procedures encompass several stages of sample preparation, including thin film deposition, device fabrication and sample characterization. All measurements on the devices were conducted utilizing a custom-built magneto-transport setup. The chapter further delves into a detailed description of the different components comprising this home-built system.

#### 2.1 Thin film deposition

In this thesis, material deposition was accomplished through the utilization of the physical vapor deposition (PVD) method, specifically employing the magnetron sputtering technique.

##### 2.1.1 Magnetron sputtering deposition

Thin film deposition is a vacuum-based technology used to put coatings of pure materials onto the surfaces of various objects. There are several methods known for this process. The coatings typically have a thickness ranging from angstroms to microns and can consist of either a single material or numerous materials arranged in layers. The object that needs to be coated with a layer is known as the substrate. Coating methods encompass physical vapor deposition (PVD), with one specific process known as sputtering [1]. The sputtering process, which is a high-energy production method, is used to manufacture stoichiometric thin films without altering the composition of the original material or the target material. Sputtering is also efficient in generating impermeable, dense sheets. This technique is a highly effective method for applying many layers of film for magnetic films for spintronics applications [2-4]. Sputtering involves

using high-energy ions of an inert gas or their mixes, combined with reactive gases, to remove atoms off the surface of target materials through physical bombardment. Momentum transfer takes place between high-energy ions and the atoms of the target substance as a consequence of their collision [5,6]. The ions, referred to as incident ions, induce a sequence of collision cascades on the surface of the target. Sometimes, these consecutive collisions result in the ions traveling significant distances and dissipating their energy. If the kinetic energy of the ion upon reaching the surface of the target exceeds the binding energy between the atoms of the target material, the impacted atom separates from the target material. The term used to describe this phenomenon is sputtering. In this setup, the target is maintained as a cathode, which is at a significantly negative voltage, while the other part of the vacuum chamber is kept at ground potential. The free electrons in the chamber are propelled out from the cathode, colliding with, and displacing the electrons of neutral gas atoms (such as Ar), resulting in their acquisition of a positive charge. Subsequently, the cathode target attracts these ions with positive charges, leading to a bombardment that dislodges loosely linked atoms and molecules from the target, occasionally accompanied by additional free electrons. These liberated electrons, in turn, enhance the creation of plasma (Figure 2.1). The expelled atoms and molecules of the target material move away from the target until they come into contact with other particles or a surface, such as the substrate, where they then condense. The term used to refer to this method is sputtering. In magnetron sputtering, magnets are employed to enhance the efficiency and control of the sputtering process. By employing an arrangement of magnets positioned at the cathode, it is possible to create a magnetic field that confines the electrons to closed paths in close proximity to the target surface[6]. Consequently, this enables the maintenance of a high-density plasma. The cathode target can receive power from either a DC or an RF power supply, referred to as DC and RF sputtering techniques, respectively. DC sputtering is commonly employed for metal deposition, utilizing a direct current power source to generate a glow discharge for sputtering. On the other hand, RF (radio frequency) sputtering is generally preferred for insulator thin films, utilizing an alternating current power source at radio frequencies to create a high-frequency plasma discharge, which is particularly effective for sputtering insulating materials. In this study we utilized magnetron sputtering to deposit Ta, Pt, Co, NiFe materials.

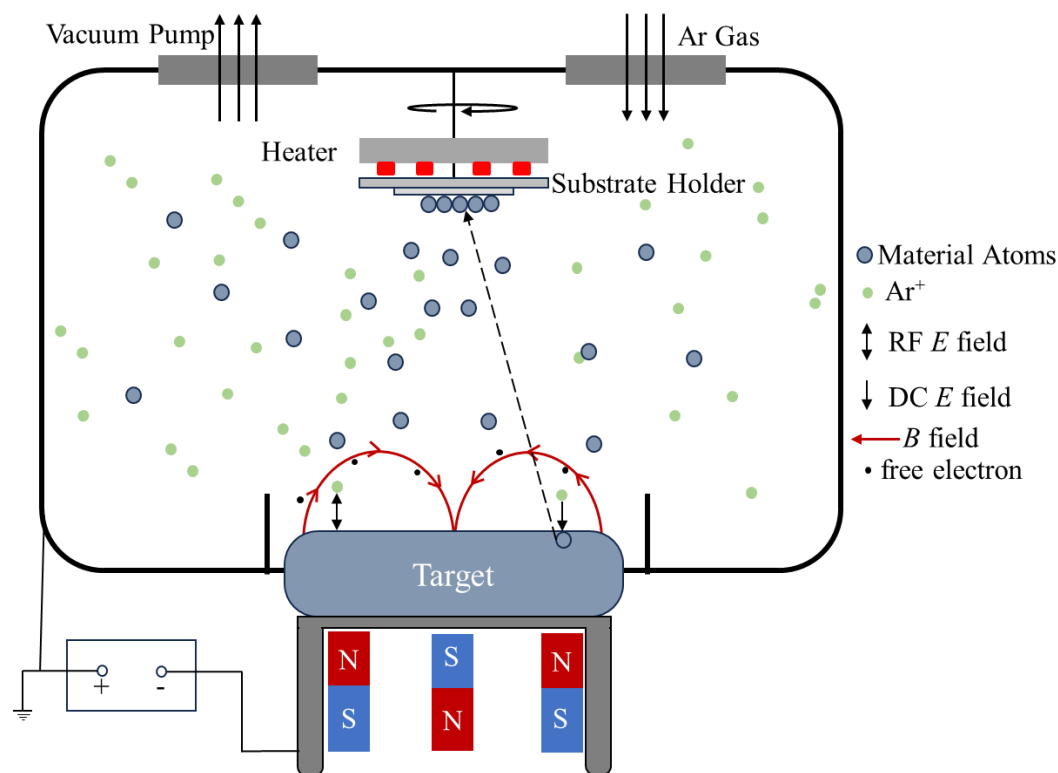


**Figure 2.1** Schematic illustrating the operation of a magnetron sputtering system.

The sputter deposition apparatus utilized for this thesis was sourced from Excel Instruments (India) and comprised a high vacuum spherical chamber measuring 12 inches in diameter. The system maintained a base vacuum level of  $7.5 \times 10^{-8}$  mbar or higher, and it included a load-lock chamber. The vacuum was sustained by an 800 L/s turbo molecular pump (from Pfeiffer vacuum) supported by a rotary pump. The spherical chamber was equipped with four 2-inch DC magnetron sputter guns grouped in a confocal manner. The targets were affixed to the guns. Shielding plates were used to prevent cross-contamination between the targets during the operation of the guns. The guns were additionally outfitted with pneumatically actuated shutters, effectively preventing any cross-contamination. The sputtering gas utilized in the chamber was ultrahigh pure Ar gas with a purity of 99.999%. It was injected into the chamber by high vacuum leak valves. The samples were introduced into the primary chambers using a load lock system, which was also evacuated by an 80 L/s turbo molecular pump (TMP) to achieve a vacuum level of  $2 \times 10^{-7}$  mbar during a time span of 2 hours. The load lock component played a crucial role in maintaining a constant high vacuum in the main chamber at all times. This decreased the likelihood of oxidation occurring on sensitive metals such as Cobalt,

Platinum and NiFe, while also reducing the entry of additional impurities from the atmosphere into the main chamber. The sputter deposition was conducted under an argon pressure of  $2 \times 10^{-3}$  mbar. The pressure mentioned was the most favourable for starting and maintaining an Ar plasma. Increased pressure typically led to the formation of porous films exhibiting elevated electrical resistance.

## 2.2 Atomic force microscopy

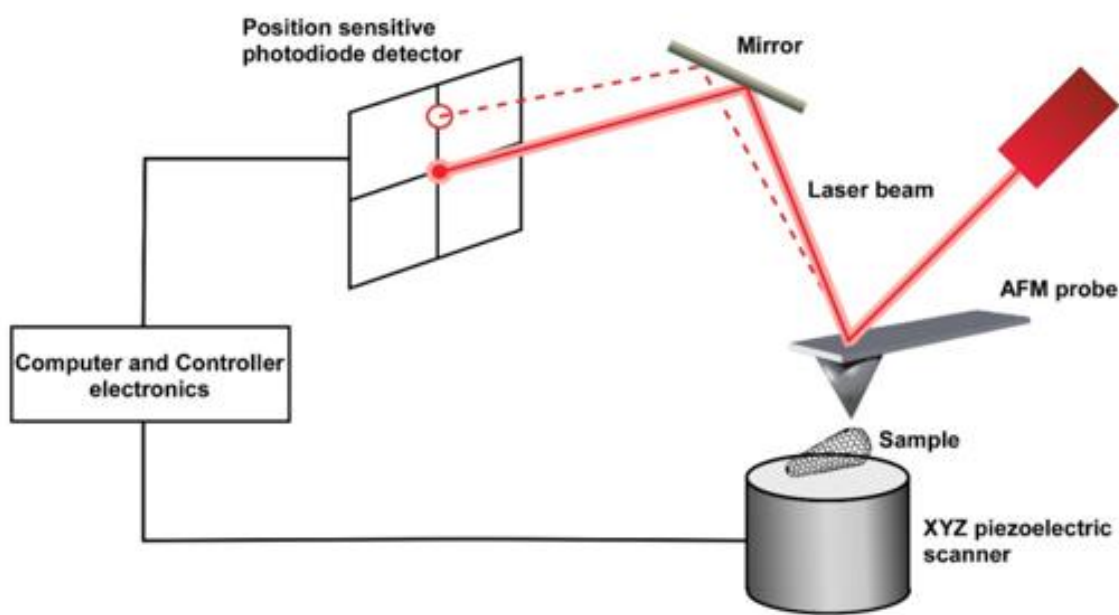


Figure 2.2: Key elements of an atomic force microscope (AFM) [Figure taken from Ref [14]]

This section delves into the intricate capabilities of Atomic Force Microscopy (AFM), a versatile measurement tool for 3D surface analysis of thin film and nanostructures[7-9]. AFM excels in providing accurate, non-destructive measurements of diverse properties such as topography, roughness, and thickness with a very high resolution[10,11]. The cantilever in AFM extends horizontally from a fixed base. It acts as a flexible support for the AFM probe or tip. The core operational principle involves scanning this probe, equipped with a sharp tip made of silicon or silicon nitride, over a thin film sample surface in a raster pattern as shown in Fig. 2.2 piezoelectric scanners use piezoelectric materials to precisely control the position of a scanning probe in three dimensions of the substrate. Controlled by a piezoelectric scanner, the

AFM tip's movement generates deflections in the AFM cantilever, tracked by a laser beam which is partially transmitted by a mirror to position-sensitive photodetector. A feedback loop in the context of computer typically refers to a system where the output of a process is fed back as input to the same process, influencing its future behaviour. This ensures a constant distance of 1nm between cantilever tip and sample yielding a detailed 3D topographic image.

To calibrate the thickness, thin films were deposited on a Si/SiO<sub>2</sub> wafer with a mask pattern, using specific sputtering parameters for a designated duration. AFM scan the whole sample surface by dividing it into many grids of small sizes. Van Der Waals interactions captures the attractive force between the atoms of the sample and the AFM tip [12,13]. At separations smaller than 1 Å the atoms in the cantilever and in the sample experience strong repulsive forces due to the overlap of electron clouds.

AFM operates in different modes, including Contact Mode, Tapping Mode, and Non-Contact Mode, each offering unique advantages and challenges[15,16]. In Contact Mode, the AFM tip maintains constant contact with the sample surface. Due to the continuous contact between the tip and the sample, in-plane shear forces are present, which limits the use of contact mode for imaging soft samples, while they are easily destroyed as a result of the tip scraping over the sample surface. To prevent potential damage to the sample caused by lateral forces, tapping mode is used. By tapping the surface intermittently at a frequency significantly faster than the lateral scan, the lateral forces between the tip and the sample are minimized. Non-Contact Mode, characterized by minimal interaction, provides super high-resolution images, albeit with challenges in maintaining tip-sample distances. The height adjustments required to maintain a constant force as the tip scans across the sample are translated into a topographic map of the surface. The variations in the height of the tip above the surface provide information about the surface features, including the thickness and roughness of the sample. This thesis utilized Bruker's Dimension ICON AFM system for precise measurements of thin film thickness and roughness.

## 2.3 Vibration sample magnetometry (VSM):

Vibration Sample Magnetometry (VSM) is a versatile and widely used technique in the field of magnetism for characterizing the magnetic properties of materials[17-19]. This method involves mounting a sample on a small vibrating platform within a magnetic field, enabling



precise measurements of the sample's magnetic response. As the sample oscillates within the magnetic field, the changes in magnetic flux are detected, providing information about its magnetic susceptibility, hysteresis loop, and other relevant properties. VSM is particularly valuable for analysing ferromagnetic, antiferromagnetic, and paramagnetic materials, offering high sensitivity and accuracy in determining magnetic moments and coercivity. This non-destructive and highly sensitive technique plays a crucial role in the magnetic characterization of various magnetic heterostructure[20]. In this thesis, MicroSense EZ9 vibrating sample magnetometer was used to characterize magnetic properties of heterostructures.

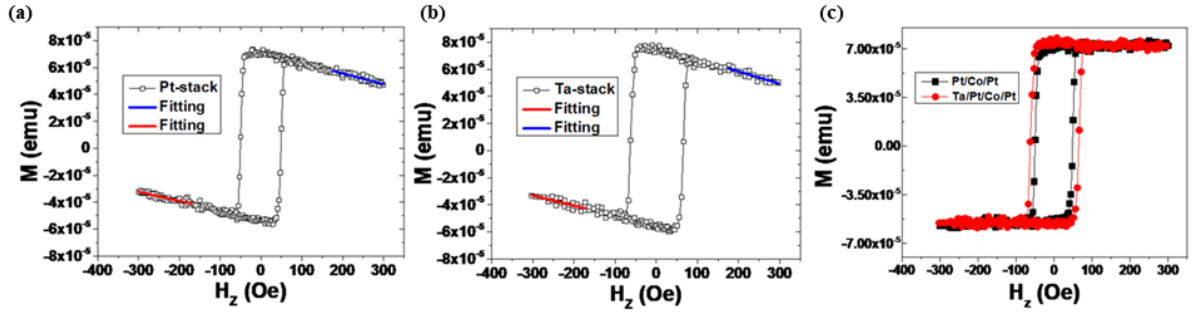


**Figure 2.3** VSM data showing magnetization vs. field (applied along z-direction) plots for PMA (a) Pt/Co/Pt stack, and (b) Ta/Pt/Co/Pt stack. (c) Processed VSM data after slope correction.

The variation of the magnetization obtained through VSM with the externally applied magnetic field along z-direction is shown in Figure 2.3 (a) (for Pt/Co/Pt) and (b) (for Ta/Pt/Co/Pt). The constant slope in the saturation region is due to the diamagnetic contribution of substrate. Afterwards, we have subtracted the diamagnetic contribution of the substrate from the VSM data. The extracted  $M$  vs.  $H$  loops for our Pt/Co/Pt and Ta/Pt/Co/Pt stacks is shown in Figure 2.3 (c).

## 2.4 Device fabrication

Following the thin film deposition and initial characterizations, the next step involved device fabrication to facilitate transport measurements. The fabrication process utilized the photolithography technique, specifically applied to create six-terminal Hall bar devices. Here, in this section photolithography technique is discussed in detail.

### 2.4.1 Photolithography

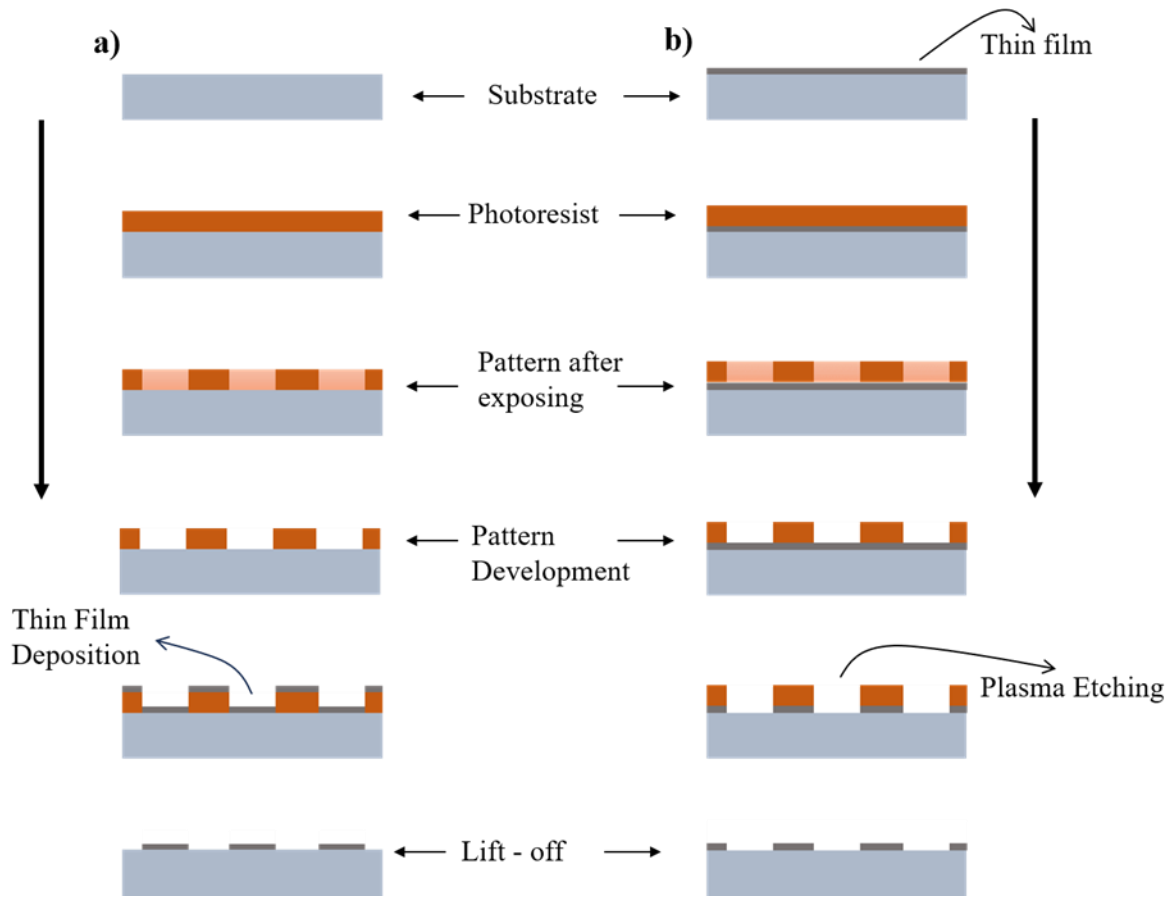


**Figure 2.4** Diagram illustrating lithography techniques, showcasing (a) the lift-off process on the left and (b) the etching technique on the right.

Photolithography constitutes a fundamental method for imprinting patterns onto a wafer surface using a photosensitive polymer solution, or photoresist. The process involves essential stages for achieving the desired design, including the application of photoresist, exposure of the wafer to light, and subsequent removal of weakened photoresist regions with a developer solution[21,22]. To execute these steps systematically, the wafer undergoes thorough cleaning with an ultrasonicator and is then dried using a nitrogen gun. The photoresist is then spin-coated onto the wafer at high speed, followed by a softbake to eliminate residual solvents and enhance the adhesion of the photoresist layer to the substrate. This mitigates the risk of nitrogen bubble formation within the photoresist due to a high solvent content. Subsequently, a digital design

generated through AutoCAD or K-layout is employed to expose the pattern with ultraviolet (UV) light. Once the desired pattern is confirmed, the final step involves developing the photoresist, wherein weakened areas are selectively removed using an alkaline solution. Photolithography patterns are formed through two distinct methods: a) lift-off, where a thin film is deposited after pattern development and later lifted off using sonication in acetone, and b) etching, where pattern formation occurs after thin film deposition. In the etching process, the residual resist and film are removed by an Ar ion beam to form the devices. The schematic in Fig. 2.4 visually depicts these systematic steps in the photolithography process.

## 2.5 Scanning Electron Microscope (SEM)

The Scanning Electron Microscope (SEM) plays an indispensable role in scientific research due to its ability to produce high-resolution images at the nanoscale level. In this study, SEM is employed to capture high-resolution images of fabricated Hall bar devices, serving as a verification tool to ensure the integrity of current and voltage channels in the devices.

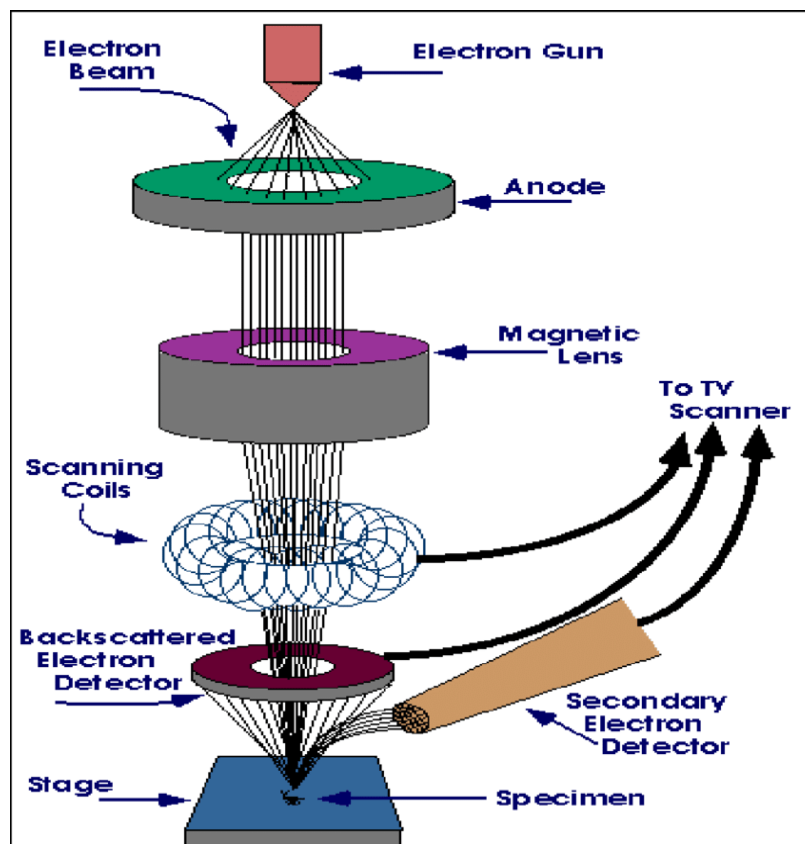


**Figure 2.5:** A schematic diagram of the scanning Electron Microscopy (SEM). (Image courtesy Iowa state university)

The resolution of visible light optical microscopes is limited by the wavelength of light used. The smallest features that can be resolved are usually a few hundred nanometers, or about half the wavelength of light. In contrast, the SEM uses an electron beam rather than visible light to function. The energy of electrons that are accelerated in a SEM can vary from a few keV to several tens of keV. The de Broglie wavelength reduces as the accelerating voltage increases because the electron velocity increases. Comparing the SEM to visible light optical microscopes, this wavelength reduction allows the SEM to reach far better resolution[23].

The SEM works by scanning a sample under vacuum with an accelerated, highly focussed electron beam in order to increase the electrons mean free path and excite the electrons within the sample. An example of a typical instrument diagram is shown in Figure 2.5. The two primary emission types used in electron guns are thermionic and field emission. Lanthanum Hexaboride is utilized for field emission and tungsten is primarily used for thermionic emission. An anode near the electron gun's tip is biased between 0.5 and 50 kV to create an electric field that draws a narrow electron beam from the tip. The electron beam is accelerated and directed towards the specimen surface by use of condenser lenses, which eventually focus and converge it. The focused electron beam is moved across the specimen's surface in a raster pattern by scanning coils that are positioned above the specimen chamber. Electrons and atoms in the sample interact when a focused electron beam hits the specimen's surface. Various kinds of electrons are emitted as a result of the interaction between the electrons and the sample's atoms as shown in Figure 2.6. Microscopic surface images of a specimen are produced using a scanning electron microscope. This is carried out by using an optical column to scan a specimen with a high energy electron beam. After that, the electrons released by the beam interact with the specimen atomic structure to produce topographic images. The beam produces a variety of electrons including backscattered and secondary electrons. Backscattered electrons (BSE) provide information regarding the specimen's atomic number and composition. It happens when a sample is repeatedly deflected across small angles. Compared to secondary electrons, BSEs can penetrate deeper within the sample and are scattered from it with less energy loss. Secondary electron (SE) reflection plays a useful role in producing a sample topographic imaging. When electrons that are initially inside the material are ejected as a result of interaction with the electron beam, secondary electrons are produced. SE typically have energy

of less than 50 eV and are located within a few nanometers of the sample surface are able to escape.

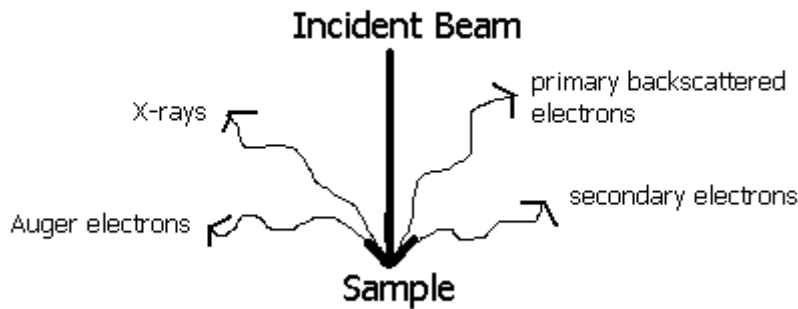


Figure 2.6: Main signals produced when the electron beam interacts with the sample.

The surface topology is provided by low energy secondary electrons. The detector collects these electrons. Mostly used detector is Everhart-Thornley Detector to collect the secondary electrons that are emitted. Typically, it consists of a photomultiplier tube to turn the light into an electrical signal and a scintillator substance that releases light when hit by secondary electrons. Pulses of light are produced when secondary electrons collide with the scintillator material. These light pulses are amplified by the photomultiplier tube, which turns them into an electrical signal proportional to the number of electrons gathered. The electronics of the SEM process the electrical signal that the photomultiplier tube produces. The final image of the specimen is built using these signals. These signals from different points on the sample surface are combined to produce a high-resolution image that depicts the surface topography and features.

## 2.6 Wire Bonding

This section describes the wire bonding which is a prevalent technology facilitating electrical connections between semiconductor chips and metal pads. Based on the energy source and force applied during bonding, wire bonding technology falls into two categories: 1) ball bonding, 2) ultrasonic wedge bonding. This thesis utilized specifically an ultrasonic wedge

bonder TPT HB02 from Technical product trade for precise bonding. Ultrasonic bonding utilizes the Aluminium wire for creating electrical contacts on Si or Si/SiO<sub>2</sub> substrates. A 50  $\mu\text{m}$  Al wire fed through the bonding tool, and the wedge-shaped tip is pressed onto bonding pads. Ultrasonic vibration in wedge bonding enhances the wire deformation process, promoting better adhesion and creating robust metallurgical bonds between the wire and bonding pads. During the initial bonding step, the bonding tool descends to the programmed bond position, establishing contact with the silicon device. Bond forces adjustable from 15grams to 150grams, accompanied by ultrasonic waves, are then applied through the bonding tool throughout the bonding duration. This duration is adjustable from 15milliseconds to 2000milliseconds. The ultrasonic method exclusively allows the creation of wedge bonds, and this technique does not rely on heat for bond formation, making it a standard in semiconductor technology. Following the creation of the first bond between the wire and pad of substrate, the tool drives the wire to form a loop, concluding at the second bond pad. During this phase, the bond head once again brings the wire into contact with defined force and ultrasonically welds the second bond onto the surface. Subsequently, the bond head slightly ascends to cut the wire. This process is fully represented in the Fig 2.7. This method proves crucial in forming desired bonds on chip pads and wire loops between chips in semiconductor technology

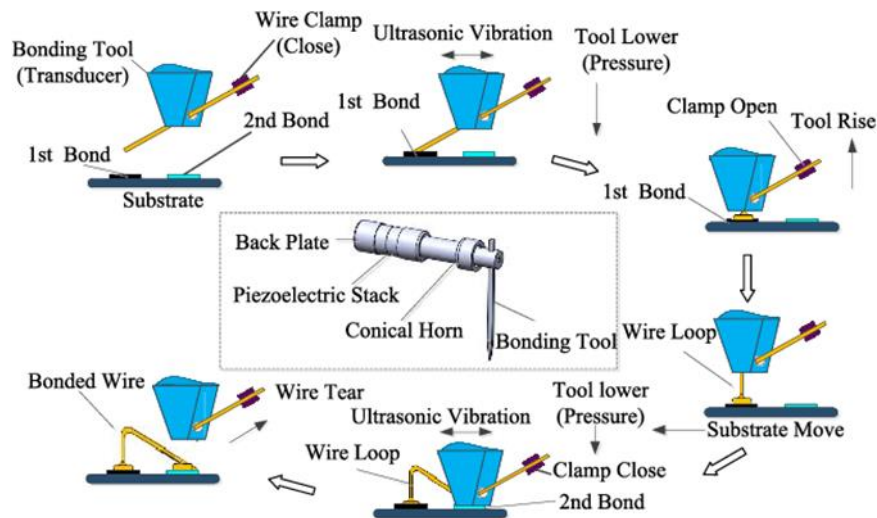


Fig: 2.7 Schematic of bonding system (Figure sourced from Ref [24])

## 2.6 Room temperature transport measurement setup

At the outset of this work, the laboratory lacked the facilities for conducting transport measurements. Consequently, a crucial goal of this thesis was to develop an electrical transport measurement setup capable of conducting all the AC and DC measurements discussed in Chapter 1. As a part of this thesis, establishment of a fully automated transport setup was done in the laboratory that can perform AHE, PHE, SOT characterization, and SOT-induced switching experiments. Thus, it was essential to combine efforts in assembling both hardware and software to create this setup, allowing for the measurement of samples using various AC and DC techniques.

### 2.6.1 Instruments required

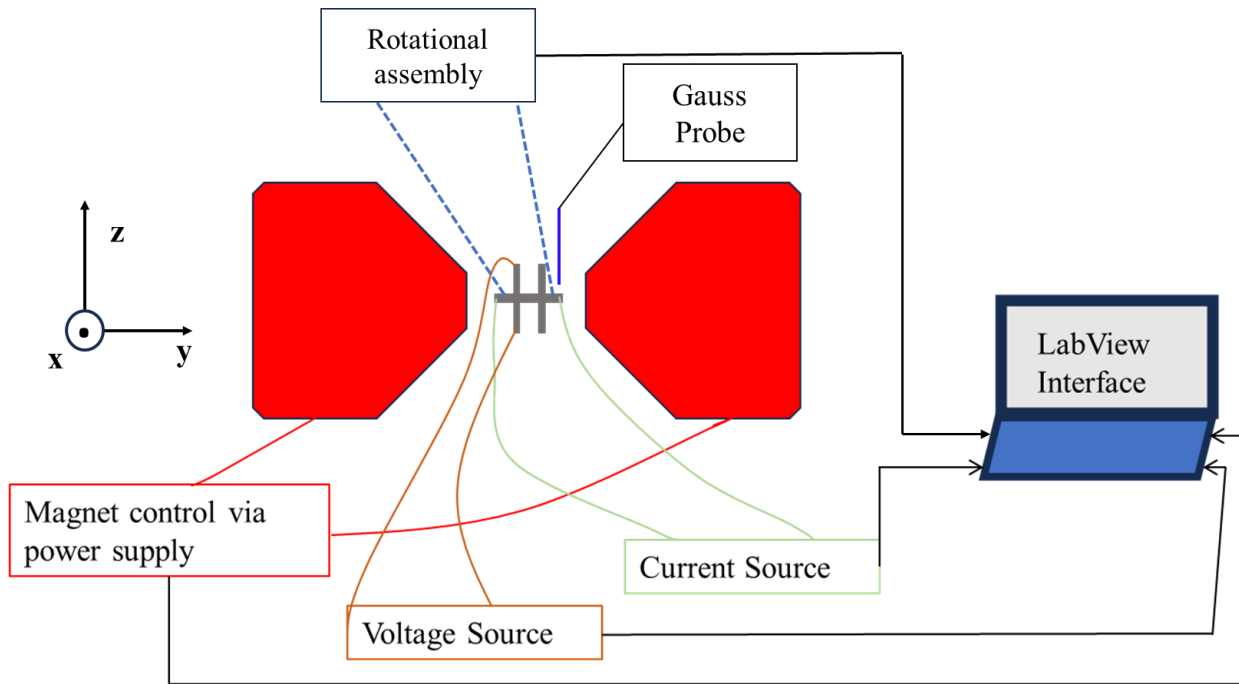


Figure 2.8 A schematic diagram of room temperature transport setup.

A schematic diagram of transport system is illustrated in Fig. 2.8. The illustration includes an electromagnet powered by a bipolar power supply, with a lithographically fabricated Hall bar device positioned between the pole pieces of the electromagnet. The orientation of the Hall bar sample can be adjusted by using different printed circuit boards (PCBs) designed within the laboratory, as elaborated later in this chapter. Wire bonding connects the current and voltage channels of the Hall bar to external circuitry. This external circuitry comprises AC or DC

current sources linked to the current channel and a DC voltmeter or lock-in amplifier connected to the voltage channels. Further, a stepper motor attached to the sample mount assembly permits the rotation of various sample orientations, allowing for measurements at various field angles. Automation and control of all these components are achieved through a PC connected to all these equipments. Consequently, the illustrated setup can measure the Hall voltage (AC or DC) by applying current (AC or DC) while sweeping either the magnetic field or field angle. A Gauss probe is positioned near the sample to provide real-time information on the applied field strength. The software component simultaneously plots the acquired data in real time, allowing for instant verification of the results.

The subsequent section provides an in-depth exploration of the efforts invested in constructing the transport setup, implementing its automation, and validating the obtained results.

### 2.6.2 Bipolar Electromagnet and Helmholtz coils

The magneto-transport experiments conducted in this thesis necessitated a consistent magnetic field. This field was generated utilizing either an electromagnet or a pair of Helmholtz coils. Specifically, the electromagnet employed in this study was the water-cooled EMH 100 electromagnet manufactured by Polytronic Corporation in India. The EMH 100 electromagnet was operated using the BCS-100 bipolar power supply, also from Polytronic Corporation. This power supply, with a capacity of 30 V and 15 A, could deliver both positive and negative currents to the electromagnet, thereby producing magnetic fields of corresponding polarities. The magnetic field strength at maximum current also depends on the separation between the pole pieces. With the device positioned between the pole pieces, a magnetic field of up to 1 Tesla could be achieved. However, a minimal separation limits the reduction in sample space between the pole pieces. Therefore, the selection of the separation distance involves a trade-off between experimental convenience and attaining the maximum available magnetic field strength. Further, cooling for the electromagnet is supplied through a custom cooling system. A steady stream of tap water is directed from a water tank from a 14 W submersible pump to the inlet of copper tubes situated within the magnet, and the circulated water is then stored in the same water tank. To maintain a low water temperature, ice gel packs are employed.

For the automation of the electromagnet, a National Instruments data acquisition device (NI-USB DAQ 6001) was employed. The NI-6001 DAQ was linked to the BCS-100 power



supply to regulate its output current, thereby controlling the magnetic field strength of the EMH 100 electromagnet. The automated system grants the ability to adjust the magnetic field, allowing for either a fixed or sweeping configuration based on the experimental requirements.

A pair of Helmholtz coils, each comprising 300 turns, were constructed to generate a stable and remanence-free field. With an applied current of 3 A, the Helmholtz coils delivered a maximum field of about 150 Oe within the sample space. When required, these coils were affixed to the electromagnet frame to supply an orthogonal field to the electromagnet's field. The calibration of field uniformity and sample positioning in both the electromagnet and Helmholtz coils was conducted using a Gauss meter from Polytronic Corporation.

### 2.6.3 Sample mount and breakout box

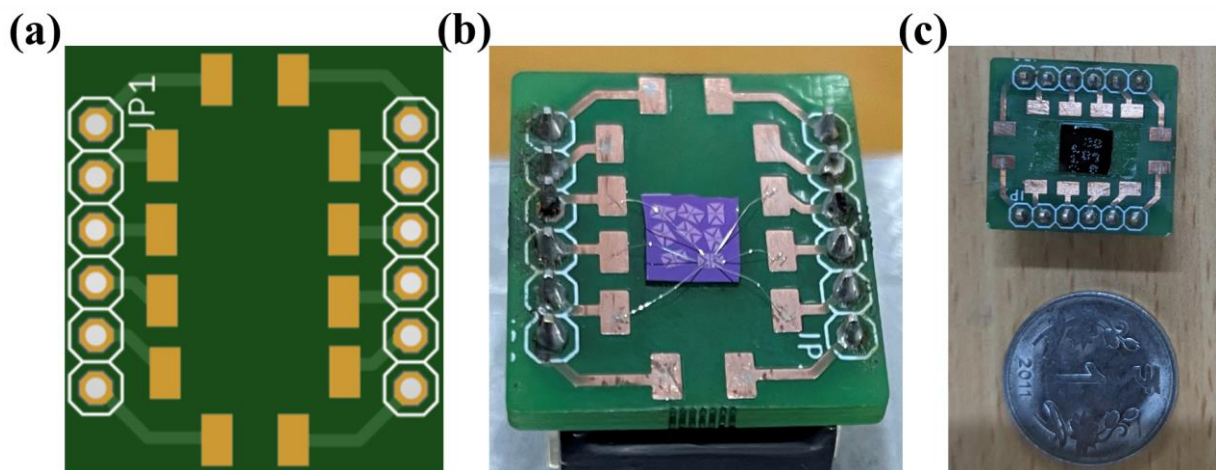


**Figure 2.9** (a) Eagle Cad generated gerber file image of 12-pin sample mount PCB design. (b) Pasted and bonded devices with different pads. (c) Actual sample mount PCB with a one-rupee coin for the size reference.

In this section, different sample mount geometries and sample holders are discussed in detail. The corresponding printed circuit boards (PCBs) were developed using the Eagle CAD software. Measurement devices were lithographically fabricated on 5 mm × 5 mm Si/SiO<sub>2</sub> substrates, which were subsequently pasted onto a 12-pin sample mount PCB. The sample mount PCB features 12 copper bonding pads connected to male pin headers soldered in parallel on the PCB, as illustrated in Figure 2.9. This chip carrier provides a sample space of 12 mm ×

8 mm. Figure 2.9 (a) display the output GERBER file image of the sample mount stage and Fig. 2.9 (b) and (c) shows actual sample mount PCB. Subsequently, this sample mount is attached to a second PCB stage offering three distinct orientation options. These orientations allow for the rotation of the device in a fixed magnetic field about different axes, as detailed later. Figure 2.10 illustrates the sample mounts on the three different orientation PCBs. The length of these PCB stages is designed to ensure that the external wiring connected to them does not occupy the space between the pole pieces of the magnet. Consequently, utilizing these PCBs minimizes the sample space between the pole pieces, enabling the attainment of a high magnetic field. Each PCB stage is equipped with 12-pin female headers connected at one end to facilitate the easy insertion of the sample mount PCB. The opposite end of this PCB stage features a 15-pin female VGA connector. The 12 pins of the sample mount PCB are then linked through the PCB stage to 12 of the 15 pins on the VGA connectors (can be seen in Fig 2.10 (a) and (b)). Subsequently, this entire PCB stage is connected to a breakout box using a male VGA counterpart, which is connected with 12 individual 25 AWG single-strand coaxial cables. The breakout box is equipped with 12 female Bayonet Neill–Concelman (BNC) connectors, facilitating easy connection to source and measurement instruments via BNC cables.

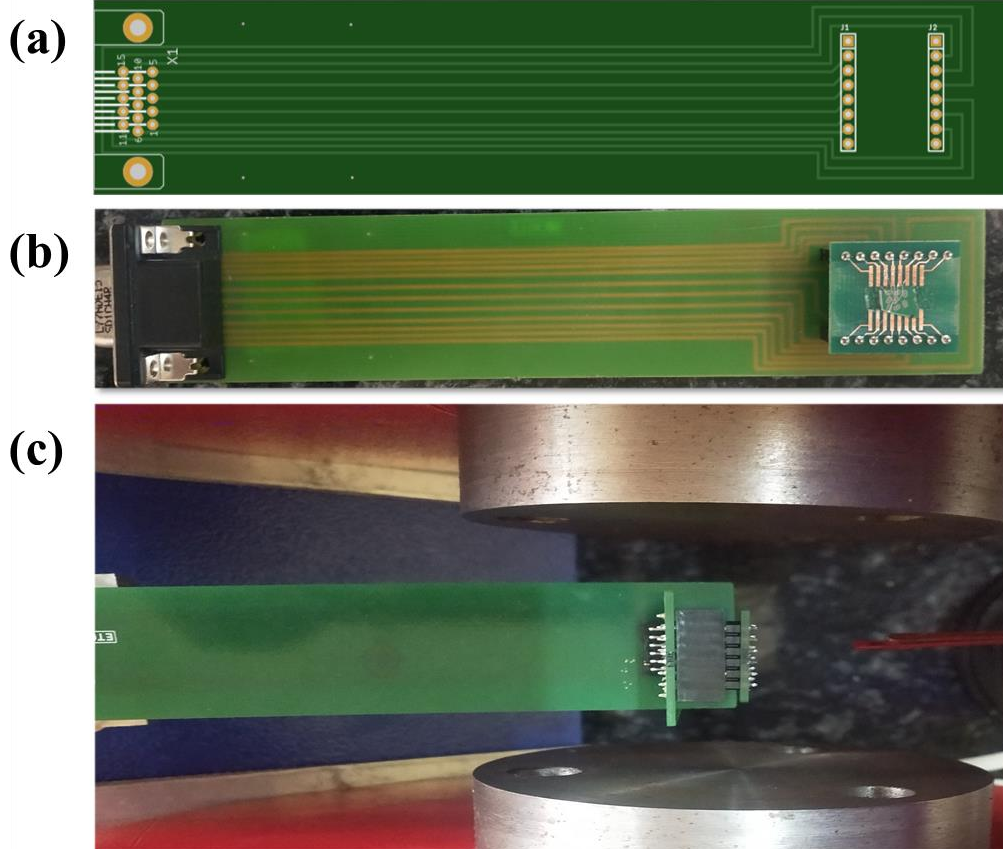


**Figure 2.10** Sample mount stage PCB for (a) xz-rotation (gerber image of design) (b) yz-rotation, and (c) xy-rotation

### 2.6.4 Rotational assembly

The ability to rotate the sample in different planes (yz-plane, xz-plane, and xy-plane) or around different axes (x, y, and z, respectively) is crucial. The rotation about these distinct axes was facilitated by a stepper motor. Initially, the stepper motor was affixed to a self-customized, vertically adjustable dual rod system. A custom-made aluminum rod was then linked to the stepper motor using a coupler, with the sample stage PCB attached to the top of the rod. The rotation about the three different axes was achieved with the assistance of three unique sample stage PCBs as depicted in Figure 2.10. PCBs in Figures 2.10 (a) and (b) were utilized for in-plane to out-of-plane field rotation, while the PCB in Figure 2.10 (c) demonstrates field rotation in-plane to the sample. To achieve the desired step size, the stepper motor was connected to the TB 6600 stepper motor driver. For automation of the rotation, the Arduino Uno R3 board was linked to the stepper driver, controlling the pulse and direction of the stepper motor. The Arduino IDE interface was utilized to upload the LIFA firmware script to the Arduino board, rendering it LabVIEW compatible.

### 2.6.5 Source and measurement units

After establishing the capabilities for both field and angular sweeps, the primary objective was to conduct transport measurements. To make the setup compatible with both AC and DC measurements, the setup incorporates Keithley 6221 current source (source both AC and DC), Keithley 2182A nanovoltmeter, Keithley 2450 source meter (for DC source and measurements), and eg&g 7265 lock-in amplifier (for AC measurements). The utilization of these instruments, coupled with the field sweep and angular sweep functionalities, enables the exploration of various effects in magnetic heterostructures such as a wide range of magnetoresistance effects, AHE and PHE voltages, SOT characterization, and SOT-induced switching.

### 2.6.5.1 AC measurements

For AC measurements Keithley 6221 is used as an AC source and eg&g 7265 was used for voltage measurements. Lock-in amplifiers can detect the voltage amplitudes at the applied AC frequency and their higher harmonics from a noisy background. The functionality of a lock-in amplifier begins with the combination of the input signal and an internally generated reference signal through a mixing process. This mixing process shifts the frequency content of the signal to a lower frequency. Subsequently, the mixed signal undergoes low-pass filtering to eliminate high-frequency noise, leaving behind the low-frequency components of interest. Crucially, the reference signal's phase can be adjusted to synchronize with the input signal's phase, enabling phase-sensitive detection. This synchronization enhances the amplifier's sensitivity to the signal. The final step involves demodulation to recover the amplitude of the signal at the reference frequency. For the accurate data acquisition, the AC source Keithley 6221 is connected with the lock-in by a homemade trigger link cable. This trigger cable converts trigger link of Keithley 6221 to a BNC cable.

Utilizing this setup which is equipped for harmonic voltage measurements, in this thesis, it was employed to detect AC AHE and PHE voltages through first harmonic measurements. Additionally, the system was utilized to characterize spin-orbit torques (SOTs) in magnetic heterostructures using second harmonic measurements. Every acquired data point is an average of at least 20 number of readings in each experiment. This number can be modified using a custom-built automated program.

### 2.6.5.2 DC measurements

In DC measurements, either the Keithley 6221 or the Keithley 2450 served as a current source, while the Keithley 2182A nanovoltmeter detected the measured signal. This configuration was used to detect DC AHE, PHE signals and SOT induced magnetization switching. Specifically, for SOT-induced switching, a current pulse was requisite. To fulfill this requirement, the Keithley 6221 (for pulse widths ranging from 15  $\mu$ S to 12 mS) and the Keithley 2450 (for pulse widths of 3 mS and above) were employed. The 2450 source meter, primarily designed for current sourcing and voltage measurement, underwent programming to enable the application of current pulses. The pulse width, starting from 3 mS, was validated using a Tektronix TDS 2002 oscilloscope. Subsequent measurements involved applying a small DC current, conducted

either through normal DC or delta measurements. In the case of delta measurements, designed to mitigate thermal drift signals, both 2-point and 3-point delta functionalities were achievable using the 2450 and 6221, respectively. Further, similar to AC measurements, a number of readings were averaged to improve the signal-to-noise ratio. All these operations can be controlled by an automated program.

To verify the transport setup, conventional magnetometry results of VSM are compared to transport measurement results. Here, one such result for the Pt/Co/Pt stack is shown (Fig. 2.11). The magnetic field was swept out of sample plane ( $H_z$ ) and measured the Hall voltage of Pt/Co/Pt Hall bar device. This stack has PMA and hence this should show a AHE signal. Obtained AHE signal then compared with the VSM results which shows a one to one correspondence of the obtained hysteresis by both AC and DC methods. The VSM results and AC AHE voltage results as a function of  $H_z$  are shown in Fig. 2.11.

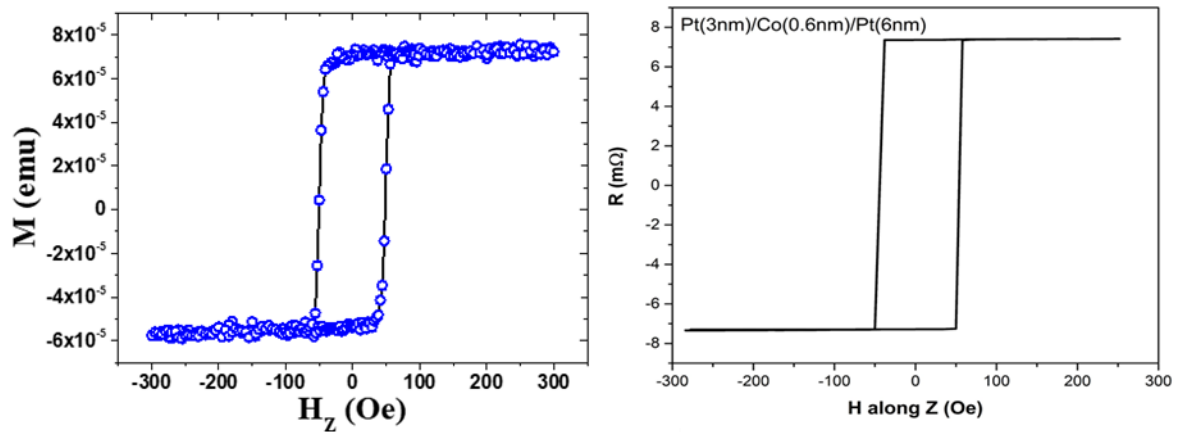


Figure 2.11 (a)  $M$  vs.  $H_z$  result for Pt/Co/Pt PMA stack obtain by VSM measurement (b)  $R$  vs  $H_z$  results measured from AHE transport measurement.

## References

- [1] M. Ohring, *Materials Science of Thin Films: Deposition and Structure* (Elsevier, 2001).
- [2] A. Hirohata and K. Takanashi, Future perspectives for spintronic devices, *Journal of Physics D: Applied Physics* **47**, 193001 (2014).
- [3] R. Wiesendanger, Nanoscale magnetic skyrmions in metallic films and multilayers: a new twist for spintronics, *Nature Reviews Materials* **1**, 16044 (2016).
- [4] R. A. Duine, K.-J. Lee, S. S. P. Parkin, and M. D. Stiles, Synthetic antiferromagnetic spintronics, *Nature Physics* **14**, 217 (2018).
- [5] J. A. Thornton, Magnetron sputtering: basic physics and application to cylindrical magnetrons, *Journal of Vacuum Science and Technology* **15**, 171 (1978).
- [6] P. J. Kelly and R. D. Arnell, Magnetron sputtering: a review of recent developments and applications, *Vacuum* **56**, 159 (2000).
- [7] T. Hugel and M. Seitz, The Study of Molecular Interactions by AFM Force Spectroscopy, *Macromolecular Rapid Communications* **22**, 989 (2001).
- [8] Rakhi and S. Sarkar, Abrupt pattern transitions in argon ion bombarded swinging Si substrates, *Physical Review B* **106**, 245420 (2022).
- [9] D. Kaur, Rakhi, P. Vashishtha, G. Gupta, S. Sarkar, and M. Kumar, Surface nanopatterning of amorphous gallium oxide thin film for enhanced solar-blind photodetection, *Nanotechnology* **33**, 375302 (2022).
- [10] P. Eaton and P. West, *Atomic force microscopy* (Oxford university press, 2010).
- [11] F. J. Giessibl, Advances in atomic force microscopy, *Reviews of Modern Physics* **75**, 949 (2003).
- [12] J. L. Hutter and J. Bechhoefer, Measurement and manipulation of van der Waals forces in atomic-force microscopy, *Journal of Vacuum Science & Technology B: Microelectronics and Nanometer Structures Processing, Measurement, and Phenomena* **12**, 2251 (1994).
- [13] A. Milling, P. Mulvaney, and I. Larson, Direct Measurement of Repulsive van der Waals Interactions Using an Atomic Force Microscope, *Journal of Colloid and Interface Science* **180**, 460 (1996).
- [14] I. Rouso and A. J. V. Deshpande, Applications of atomic force microscopy in HIV-1 research, **14**, 648 (2022).

- [15] D. Kaur, R. Wadhwa, Nisika, Y. Zhang, P. I. Kaswekar, Q. Qiao, A. Sharma, M. D. Poliks, and M. Kumar, Interfacial-Mixing and Band Engineering Induced by Annealing of CdS and a-Ga<sub>2</sub>O<sub>3</sub> n–n-Type Thin-Film Heterojunction and Its Impact on Carrier Dynamics for High-Performance Solar-Blind Photodetection, *ACS Applied Electronic Materials* **5**, 3798 (2023).
- [16] Y. Zhang, H. Zhao, and L. Zuo, Contact dynamics of tapping mode atomic force microscopy, *Journal of Sound and Vibration* **331**, 5141 (2012).
- [17] A. Pradeep, P. Priyadharsini, and G. Chandrasekaran, Sol–gel route of synthesis of nanoparticles of MgFe<sub>2</sub>O<sub>4</sub> and XRD, FTIR and VSM study, *Journal of Magnetism and Magnetic Materials* **320**, 2774 (2008).
- [18] M. Z. Kassae, E. Motamedi, and M. Majdi, Magnetic Fe<sub>3</sub>O<sub>4</sub>-graphene oxide/polystyrene: Fabrication and characterization of a promising nanocomposite, *Chemical Engineering Journal* **172**, 540 (2011).
- [19] A. Quindeau *et al.*, Tm<sub>3</sub>Fe<sub>5</sub>O<sub>12</sub>/Pt Heterostructures with Perpendicular Magnetic Anisotropy for Spintronic Applications, *Advanced Electronic Materials* **3**, 1600376 (2017).
- [20] S. Foner, The vibrating sample magnetometer: Experiences of a volunteer (invited), *Journal of Applied Physics* **79**, 4740 (1996).
- [21] L. F. Thompson, in *Introduction to Microlithography* (AMERICAN CHEMICAL SOCIETY, 1983), pp. 1.
- [22] H. J. Levinson, *Principles of lithography* (SPIE press, 2005), Vol. 146.
- [23] L. Reimer, *Scanning Electron Microscopy: Physics of Image Formation and Microanalysis*, Second Edition, *Measurement Science and Technology* **11**, 1826 (2000).
- [24] Z. Long, J. Zhang, X. Wu, Y. Liu, X. Zhou, and Z. Li, Impedance Modeling of Ultrasonic Transducers Used in Heavy Aluminum Wire Bonding, *IEEE Transactions on Components, Packaging and Manufacturing Technology* **8**, 1107 (2018).

## Chapter 3

# Separation of Spin-orbit torque from thermoelectric effects and detection of SOT induced field-free magnetization switching in Pt/Co/Pt stack with Ta-underlayer utilizing thermoelectric effect

### 3.1 Introduction

Recent years have witnessed a renewed interest in developing spin-based logic and memory devices capable of operating at high frequency with low energy consumption[1-4]. However, spin-transfer torque (STT) based magnetic random access memory devices experiences low endurance issues due to the flow of high current density through the tunnel barrier during writing operation[5,6]. In this regard, MRAM utilizing spin-orbit torque (SOT) mechanism for magnetization switching becomes of paramount importance owing to better endurance, faster access time and lower energy consumption in comparison to STT-MRAM. In SOT-MRAM, lateral current flowing through the heavy metal (HM) layer generates spin current due to the bulk spin-Hall effect (SHE)[3,7-9] or/and interfacial Rashba-Edelstein effect (REE)[10,11]. The spin current in-turn induces a torque in the adjacent ferromagnetic (FM) layer. Here, magnetization is subjected to antidamping-like ( $\tau_{AD} \propto m \times (m \times \sigma)$ ) and field-like ( $\tau_{AD} \propto m \times (m \times \sigma)$ ) torques ((AD-SOT) and FL-SOT, respectively) produced by applied current in lateral direction of HM. The AD-SOT yields an effective field  $H_{AD} (\propto (m \times \sigma))$  while FL-SOT yield  $H_{FL} (\propto \sigma)$ . Here,  $\sigma$  is spin polarization vector[3,12]. Moreover, for realizing high density SOT-MRAM, the robust perpendicular magnetic anisotropy (PMA) in the HM/FM heterostructures is desired to maintain a significant energy barrier prohibiting the thermal fluctuation.

SHE induced AD-SOT is the dominating torque which can manipulate magnetization orientation in PMA based magnetic heterostructures[1,3,13]. In order to exploit the nature of



SHE and engineer the SOT in magnetic heterostructures, different stacks of HMs and FMs possessing PMA are used. Amongst them, HM/FM/HM stacks with PMA are of particular interest where the HM layers can be of dissimilar materials[14-17]. By carefully engineering the HM layer according to their spin-Hall angles ( $\theta_{SH}$ ), SOTs and other magnetic properties in HM/FM/HM heterostructures become tuneable. For instance, Pt/Co/Ta enhances SOT efficiency[17] as both the HMs have opposite  $\theta_{SH}$ , whereas, a symmetric thickness of Pt in the Pt/Co/Pt stack diminishes the SOT efficiency[15,16]. Remarkably, the Ta/Pt/Co/Ta stack enhances the SOT efficiency as well as the anisotropy field[14]. Thus, HM/FM/HM stack with PMA and varying spin current is considered as an ideal composite FM layer for investigating different SOT studies.

It is usual to introduce a Ta underlayer for better adhesion and smoothness of the HM layer while studying the SOT effects in HM/FM heterostructures[18]. In the present study, we showed that due to the addition of a Ta underlayer to the perpendicularly magnetized Pt/Co/Pt asymmetric stack, various physical phenomena emerge which was otherwise negligible in Pt/Co/Pt stack. Here, Pt/Co/Pt asymmetric stack was considered as a model system for studying different SOT behaviour. We had characterized the SOTs in Ta/Pt/Co/Pt stacks in comparison to the Pt/Co/Pt asymmetric stack with Co layer in the form of a wedge, in both the stack. We had used low field AC harmonic Hall voltage technique[19,20] and magnetization angle-resolved harmonic Hall technique[21,22] for estimating the SOT contribution in Pt/Co/Pt and Ta/Pt/Co/Pt stack, respectively. It was found that AD-SOT contribution in Ta/Pt/Co/Pt stack is similar to the value of AD-SOT for Pt/Co/Pt stack. However, inversion symmetry breaking at the interface of Co layer generates FL-SOT, which is negligible in both the stacks due to similar interfaces about Co layer. Moreover, in Ta/Pt/Co/Pt stack, significant thermoelectric effects persist in comparison to Pt/Co/Pt stack due to electrical resistivity mismatch between Ta underlayer and Pt/Co/Pt stack. As a result of the differing resistivity, the different current flows between the Pt/Co/Pt stack and the Ta underlayer, which causes different joule heating in these layers, causing the thermal gradient to appear in the whole stack. Further, we observed field-free switching in Ta/Pt/Co/Pt stack using conventional DC Hall methodology. In addition, we had utilized the thermoelectric effects in Ta/Pt/Co/Pt as a reading mechanism for magnetization switching. We developed an AC Hall resistance reading technique using anomalous Nernst effect (ANE) to detect the field-free switching in Ta/Pt/Co/Pt apart from estimating the switching current values using our reading technique.

### 3.2 Experimental details

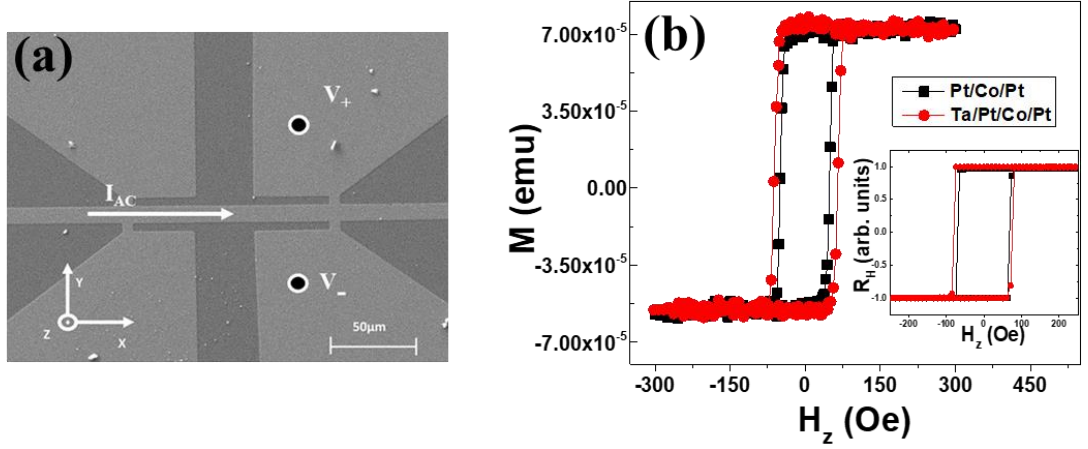


**Figure 3.1** (a) Scanning electron microscopy image of the six-terminal Hall bar devices with Hall measurement geometry. (b) Magnetization measurements by VSM as a function of out-of-plane applied field ( $H_z$ ) and inset shows AHE resistance measurements vs.  $H_z$ .

The thin film stacks of Pt(3)/Co(0.6)/Pt(6) (hereafter denoted as Pt stack) and Ta(3)/Pt(3)/Co(0.6)/Pt(6) (hereafter denoted as Ta stack) were deposited onto thermally oxidized Si/SiO<sub>2</sub> substrate by DC-magnetron sputtering at room temperature after achieving a base pressure  $\sim 10^{-8}$  Torr at a working pressure of 3 mTorr. The thickness of the films indicated in the parenthesis are in nanometers. Six terminal hall bar devices (Figure 3.1(a)) with a dimension of  $135\mu\text{m} \times 12\mu\text{m}$  were patterned using standard photo-lithography and plasma etching process. In our Hall bar devices, current channels along and perpendicular to the Co thickness gradient direction, were fabricated. Notably, devices with current channel parallel to the wedge direction were considered to have insignificant thickness gradient along y-direction (Figure 3.1(a)) and considered as uniformly grown Co devices. In this work, Pt stack and Ta stack corresponds to the thin film stacks with Co layer in wedge form unless otherwise mentioned. Unpatterned films in both the stacks were utilized for the vibration sample magnetometry (VSM) measurements. Figure 3.1(b) shows the variation of the magnetization of the stacks vs. applied field along z-direction ( $H_z$ ). The square shaped hysteresis loop as depicted in Figure 3.1(b) confirms the PMA behaviour in both the stacks which was further corroborated by performing anomalous Hall effect (AHE) resistance measurement as a function of  $H_z$  (inset of Figure 3.1(b)). The saturation magnetization ( $M_s$ ) was found to be  $\sim 1057 \pm 8$  emu/cc for Pt stack and  $\sim 1135 \pm 8$  emu/cc for Ta stack, respectively which is similar in

magnitude. For the quantitative study of SOTs, AC measurement techniques utilizing lock-in amplifiers (EG&G 7265) with reference frequency of 577.13 Hz were used. Current induced magnetization switching was probed using the DC Hall measurement technique (utilizing Keithley 2450 source meter and Keithley 2182A nanovoltmeter) and 2<sup>nd</sup> harmonic AC Hall technique. All transport measurements were carried out at room temperature.

### 3.3 Results and discussion

#### 3.3.1 Separation of AHE and PHE contributions

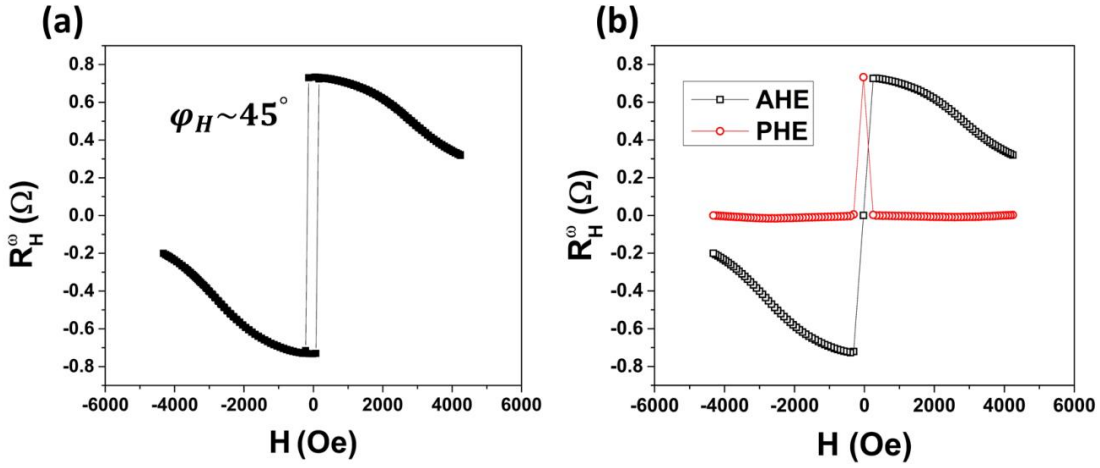


**Figure 3.2** (a) First harmonic Hall resistance ( $R_H^\omega$ ) as a function of in-plane magnetic field applied at  $\sim 45^\circ$  from current direction (For Pt/Co/Pt stack). (b) Separated AHE and PHE resistances as a function of in-plane field.

Anomalous and planar Hall (AHE and PHE) contributions are separated by symmetrization and anti-symmetrization of Hall resistance data with respect to the external magnetic field.  $R_H^\omega$  as a function of in-plane external magnetic field (applied along  $\phi_H \sim 45^\circ$ ) is shown in Fig.3.2(a) which has both AHE and PHE contributions. AHE have an odd symmetry with respect to the reversal of magnetization ( $R_{AHE} \propto m_z$ ) while PHE have an even symmetry with respect to the reversal of magnetization ( $R_{PHE} \propto m_x m_y$ ). It is evident that the anti-symmetrization and symmetrization of  $R_H^\omega$  data with respect to field axis can separate the AHE

and PHE contribution, respectively[16,23]. Hence  $R_H^\omega(-H_z \rightarrow +H_z) + R_H^\omega(+H_z \rightarrow -H_z)$  provides AHE contribution while  $R_H^\omega(-H_z \rightarrow +H_z) - R_H^\omega(+H_z \rightarrow -H_z)$  extract PHE contribution. Symmetrized and anti-symmetrized data is shown in Fig. 3.2(b). AHE to PHE ratio for Pt/Co/Pt stack is 0.02 and for Ta/Pt/Co/Pt stack is 0.002.

### 3.3.2 Anisotropy field ( $H_k$ ) calculations

#### 3.3.2.1 For Pt/Co/Pt sample

First harmonic Hall voltage ( $V_H^\omega$ ) data of Pt/Co/Pt device as a function of applied magnetic field along the current direction ( $H_x$ ) is shown in Fig. 3.3(a). The  $V_H^\omega(H) = V_H^\omega(0) \sqrt{1 - \left(\frac{H}{H_K}\right)^2}$  fitting of this data in low field regime provides the value of anisotropy field[21] which is  $0.349 \pm 0.007$  T.

**3.3.2.1 For Ta/Pt/Co/Pt sample:** According to the previous method adopted for Pt/Co/Pt stack,  $H_k$  is the field value where the fitting curve cuts the  $x$ -axis. Ta insertion enhances the anisotropy significantly rendering the switching signal very large. Thus, the curve fitting, as described for previous case, does not provide the  $H_k$  value. For Ta/Pt/Co/Pt stack, we have calculated the anisotropy field using[22]:

$$\sin(2\theta) = \frac{2H_{ext}}{H_k} \sin(\theta_H - \theta) \quad (3.1)$$

where,  $\theta_H$  is angle between the external magnetic field ( $H_{ext}$ ) and  $z$ -axis.  $\theta$  is magnetization angle. The method to find  $\theta$  values from magnetic field rotation is discussed in the main text. The fitting of Eq. (3.1) is shown in Fig. 3.3(b). The obtained value of  $H_k$  is  $\sim 1.43 \pm 0.23$  T for Ta/Pt/Co/Pt stack in comparison to the  $H_k \sim 0.34$  T observed for Pt/Co/Pt stack. The enhancement in the  $H_k$  due to the insertion of the Ta under layer is a result of enhance spin-orbit coupling at the interfaces[14].

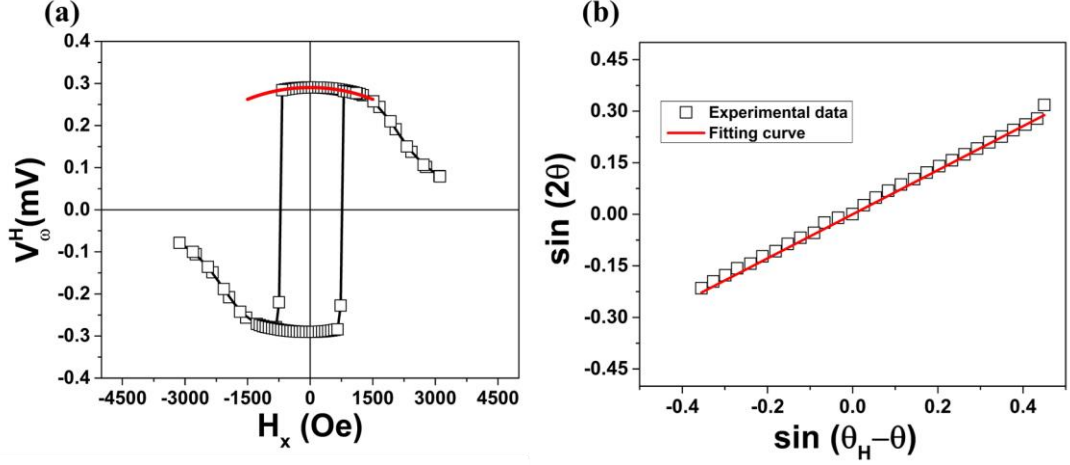


**Figure 3.3** (a) First harmonic Hall voltage data ( $V_H^\omega$ ) as a function of field along  $x$ -direction ( $H_x$ ) for Pt/Co/Pt stack, the fitted curve in low field regime is shown in red color. (b)  $\sin(2\theta)$  vs.  $\sin(\theta_H - \theta)$  for Ta/Pt/Co/Pt stack at external magnetic field 4500 Oe.

### 3.3.3 SOT measurement for the Pt stack

For Pt stack, effective fields induced by AD-SOT ( $H_{AD}$ ) and FL-SOT ( $H_{FL}$ ) were extracted using low field harmonic Hall measurement method. The results of harmonic Hall voltage measurements with varying external magnetic field for Pt stack are shown in Figure 3.4. Figure 3.4 (a) depicts the experimental geometry and coordinate system along with the material stack. Figure 3.4 (b) shows the representative plots for the in-phase first harmonic Hall voltage  $V_H^\omega$  (left y-axis) and out-of-phase second harmonic voltage  $V_H^{2\omega}$  (right y-axis) as a function of the external magnetic field applied in the direction of current ( $H_x$ ). The variation of  $V_H^\omega$  (left y-axis) and  $V_H^{2\omega}$  (right y-axis) as a function of the external magnetic field transverse to the current ( $H_y$ ) is shown in Figure 3.4 (c). A small out-of-plane field was applied during the experiment to prevent the domain nucleation in the low field range. The effective fields  $H_{AD}$ , and  $H_{FL}$  generated by current-induced AD-SOT and FL-SOT are calculated using[19]:

$$H_{AD(FL)} = \frac{B_{AD(FL)} \pm 2\xi B_{FL(AD)}}{1 - 4\xi^2} \quad (3.2)$$

where  $B_{AD(FL)} = -2 \left( \frac{\partial V_H^{2\omega}}{\partial H_{x(y)}} \right) / \left( \frac{\partial^2 V_H^\omega}{\partial H_{x(y)}^2} \right)$  and  $\xi = \Delta R_{PHE} / \Delta R_{AHE}$  is the ratio of planar Hall and anomalous Hall resistances. Here  $\pm$  sign corresponds to up-and down-magnetization, respectively. Fitting of first and second harmonic Hall voltage ( $V_H^\omega$  and  $V_H^{2\omega}$ , respectively) using

Eq. (3.2) determines the  $H_{AD(FL)}$ . The variation of the extracted  $H_{AD}$ , and  $H_{FL}$  values under different applied currents are depicted in Figure 3.4 (d).

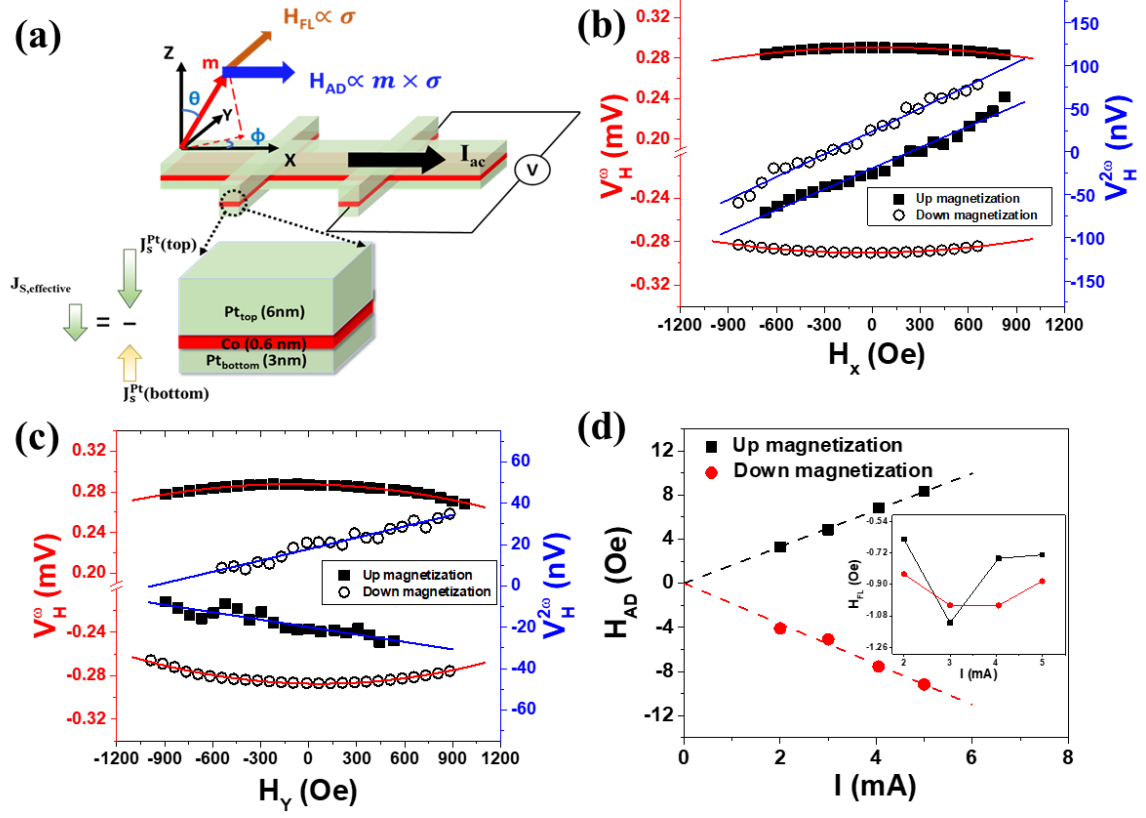


**Figure 3.4** (a) Pt stack with directions of spin currents ( $J_S$ ) flowing from each HM layer and an effective spin current direction, along with the schematic diagram for the AC Hall measurement with its coordinate geometry. (b) First harmonic ( $V_H^\omega$ ) and second harmonic ( $V_H^{2\omega}$ ) voltage vs. magnetic field sweep in  $x$ -direction ( $H_x$ ) under  $\sim 4$  mA current. (c)  $V_H^\omega$  and  $V_H^{2\omega}$  vs. magnetic field sweep in  $y$ -direction ( $H_y$ ) under  $\sim 4$  mA current. (d)  $H_{AD}$  as a function of applied AC currents (inset:  $H_{FL}$  vs. AC current).

$H_{AD}$  values increases with the applied current at a rate of  $+1.6 \pm 0.02$  Oe/mA ( $-1.8 \pm 0.08$  Oe/mA) for up-magnetization (down-magnetization) whereas  $H_{FL}$  in Pt stack shows no particular trend and is always an order smaller than  $H_{AD}$  (Figure 3.4(d)). The similar interfaces of Pt on both sides of the Co layer show the insignificant effect of Rashba-Edelstein effect (REE) and, as an outcome, FL-SOT is negligible compared to the AD-SOT[15]. The significant

$H_{AD}$  values suggest that, due to the Pt thickness asymmetry on both side of Co thin film, a net spin current flows from the thicker Pt in the Pt stack.

### 3.3.4 Second harmonic signal comparison for Pt stack and Ta stack

Next, we compared the second harmonic Hall resistance ( $R_H^{2\omega}$ ) as a function of magnetic field, swept along the current direction ( $H_x$ ) for both Pt and Ta stacks which is depicted in Figure 3.5. The  $R_H^{2\omega}$  vs.  $H_x$  curve for Pt stack (Figure 3.5(a)) differs distinctly from the  $R_H^{2\omega}$  vs.  $H_x$  plot of Ta stack (Figure 3.5(b)). The Pt stack curve shows a generic AD-SOT behaviour with asymmetric  $R_H^{2\omega}$  about the field axis (as,  $H_{AD} \propto m \times y$ )[21,24]. In case of Ta stack, the  $R_H^{2\omega}$  vs.  $H_x$  plot exhibits a significant hysteric nature in low field regime. This is attributed to the presence of thermoelectric effects[22]. The electrical current passing through the sample leads to Joule heating which in turn creates the temperature gradient ( $\nabla T$ ) due to mismatch in the resistivity and thermal conductivity in the stack after introducing the Ta layer[25,26] (illustrated in Figure 3.5(b)). Notably, the temperature gradient in Ta stack can generate anomalous Nernst effect (ANE) along with longitudinal spin Seebeck effect (SSE)[26,27]. However, the contribution of the SSE is negligible since the Ta stack possesses significant PMA[27]. Thus, the hysteric nature is attributed to the presence of ANE in Ta stack. Notably, in spite of keeping Co thickness of 0.6 nm in both the Ta stack & Pt stack, in Ta stack considerable ANE emerges. Note that, for Pt stack, the Pt (3 nm) and Pt (6 nm) undergoes different growth conditions (initial Pt(3) was grown on Si/SiO<sub>2</sub> wafer whereas Pt(6) was grown on Co layer) which may lead to the difference in the resistivities[15,28] of the Pt thin films (top & bottom) in comparison to the Co thin film. This could lead to the ANE in Pt stack as well. Moreover, while analysed closely, the inset of Figure 3.5(a) shows very faint hysteric signal. In order to comprehend the relative contribution of the ANE in Pt stack & Ta stack, we have measured the variation of the  $R_H^{2\omega}$  with the external field ( $H_z$ ) swept along the z-axis of the sample[27]. Figure 3.5(c) exhibits the variation of the  $R_H^{2\omega}$  vs.  $H_z$  for both Pt stack & Ta stack. The occurrence of the feeble hysteresis for Pt stack in comparison to the Ta stack confirms that the ANE signal is dominant (negligible) in Ta stack (Pt stack). Notably, the voltage generated due to ANE is proportional to  $m \times \nabla T$ , ( $m$  being the magnetization of the thin film) which has similar magnetization dependency as  $H_{AD}$ . In this regard, while estimating  $H_{AD}$  through the

measurement of  $R_H^{2\omega}$ , the contribution of the ANE needs to be separated else it would lead to the overestimation of the  $H_{AD}$  values in Ta stack.

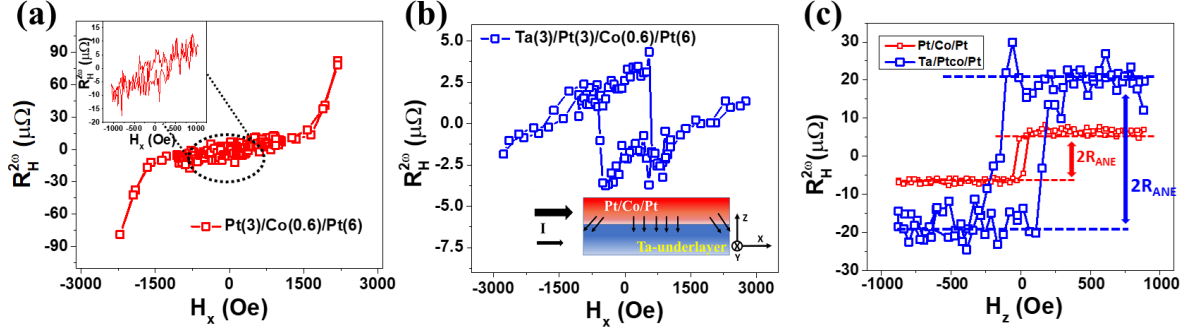


**FIGURE 3.5** (a)  $R_H^{2\omega}$  vs.  $H_x$  for Pt stack. Inset: zoom-in view of  $R_H^{2\omega}$  vs.  $H_x$  in lower field regime. (b)  $R_H^{2\omega}$  vs.  $H_x$  for Ta stack (Inset: thermal gradient due to resistivity mismatch, color gradients indicate the heat distribution in each layer. The darker portion represents the hot region, while the lighter portion represents the cold region in each layer in the picture, black arrows point from top to bottom layer, indicating heat flow direction. The thickness of the right arrow denotes the magnitude of the current flowing through these layers.), (c)  $R_H^{2\omega}$  vs.  $H_z$  comparison for Pt stack and Ta stack, measurements are performed at  $J_{AC} \sim 1 \times 10^{10} \text{ A/m}^2$ .

### 3.3.5 SOT measurement for the Ta stack

To extricate the AD-SOT generated effective field from the ANE contribution, we followed a low field second harmonic magnetization rotation technique recently developed by H Yang *et al.*[22] In this method, the  $R_H^\omega$  and  $R_H^{2\omega}$  were measured to quantify AD-SOT and ANE contribution by rotating the sample in  $xz$ -plane in presence of a constant magnetic fields ( $H_{ext}$ )[21,22]. The angle  $\theta_H$  defines the direction of magnetic field from the  $z$ -axis (experimental geometry shown in Figure 3.6(a)). The contribution of FL-SOT is negligible for Ta stack due to similar interfaces about Co layer (supplementary information). Considering trifling contribution from planar Hall effect (from section 3.3.1) and FL-SOT for Ta stack (discussed later), the magnetization angle ( $\theta$ ) dependent  $R_H^{2\omega}$  in presence of  $H_{ext}$  can be expressed as[22]:

$$R_H^{2\omega} = \left( \frac{\Delta R_{AHE}}{2} \frac{H_{AD}}{H_{ext} + H_k} + I_0 \alpha \nabla T \right) \sin \theta. \quad (3.3)$$



where  $\alpha$  is the ANE coefficient and  $I_0$  is the applied AC current defined by  $I_{AC} = I_0 \sin(\omega t)$ . The magnetization angle  $\theta$ , was found using  $\theta = \cos^{-1}(\text{Norm. } R_H^\omega)$  where the normalized  $R_H^\omega$  was obtained as a function of magnetic field angle ( $\theta_H$ ) (Figure 3.6(b)). Eq. (3.3) can further be modified as:

$$\frac{dR_H^{2\omega}}{d(\sin\theta)} = \frac{\Delta R_{AHE}}{2} \frac{H_{AD}}{H_{ext}+H_k} + I_0 \alpha \nabla T \quad (3.4)$$

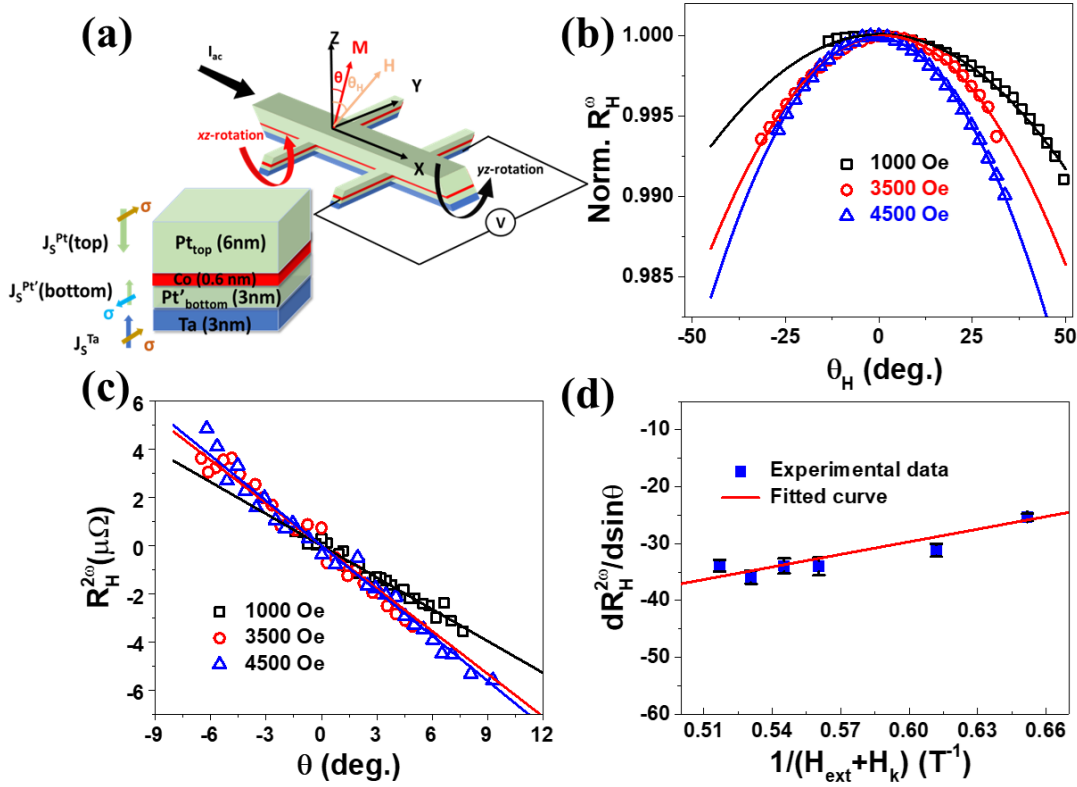


**FIGURE 3.6** (a) Illustration of the experimental geometry and spin current ( $J_s$ ) and polarization directions ( $\sigma$ ) for each HM layer in Ta- stack. (b) Normalized  $R_H^\omega$  vs.  $\theta_H$ . (c)  $R_H^{2\omega}$  vs.  $\theta$  at different external magnetic fields. (d) Contributions of SOT and ANE as a function of  $1/(H_{ext}+H_k)$ . Measurements are performed at  $I_{AC} = 4.4$  mA.

Thus, it is important to plot the variation of  $R_H^{2\omega}$  vs.  $\theta$  which is depicted in Figure 3.6(c). According to the Equation (3.4) the slope of the variation of  $R_H^{2\omega}$  vs.  $\sin\theta$  would give rise to the quantification of the ANE voltage along with AD-SOT. Figure 3.6(d) shows the plot of  $\frac{dR_H^{2\omega}}{d(\sin\theta)}$  vs.  $\frac{1}{H_{ext}+H_k}$ . The slope of this graph leads to the estimation of the AD-SOT whereas the intercept predicts the ANE contributions in Ta stack. In our calculation we have used  $H_k \sim 1.4$

T for Ta stack. From Figure 3.6(d) and using Eq. (3.4) we have obtained  $H_{AD} \sim 7$  Oe and  $V_{ANE} = 0.32 \mu V$ . [21,22]

FL-SOT is determined by using the angle resolved magnetization rotation technique when  $H_{ext}$  is rotated in  $yz$ -plane [22]. The FL-SOT is induced in HM/FM heterostructures due to the interfacial Rashba-Edelstein effect (REE). For Ta/Pt/Co/Pt stack, the variation of  $V_H^{2\omega}$  vs.  $\theta_H$  does not show any significant trend in the resolution limit of our setup (Fig. 3.7). This indicates that the FL-SOT values are insignificant, similar to the Pt/Co/Pt case. The similar Pt interfaces about Co layer diminish the FL-SOT effect in both Pt/Co/Pt and Ta/Pt/Co/Pt stacks.

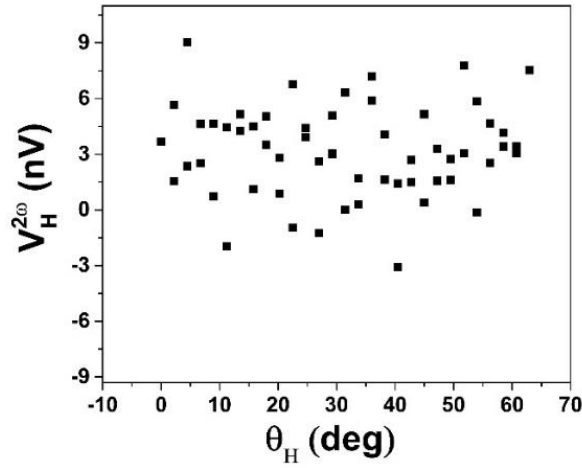


**Figure 3.7** Second harmonic Hall voltage  $V_H^{2\omega}$  as a function of magnetic field angle ( $\theta_H$ ) in  $yz$ -plane.

Remarkably,  $H_{AD}$  for Ta stack matches well with the value of  $H_{AD}$  for Pt stack when measured with the same current density of  $\sim 3 \times 10^{10} \text{ A/m}^2$ . The intuitive picture leading to this similarity in the  $H_{AD}$  values in both the samples is depicted in Figure 3.6(a). In Pt stack, AD-SOT was generated because of thickness asymmetry in  $\text{Pt}_{\text{top}}$  and  $\text{Pt}_{\text{bottom}}$  (as shown in Figure 3.6(a)). The effective spin current acting on the Co layer for Pt stack can be expressed as  $J_s^{\text{Pt}}(\text{top}) - J_s^{\text{Pt}}(\text{bottom})$ . Similarly, for Ta stack, the resultant spin current can be expressed as  $J_s^{\text{Pt}}(\text{top}) - J_s^{\text{Pt}'}(\text{bottom}) + J_s^{\text{Ta}}(\text{bottom})$ . Notably, the addition of Ta underlayer produces a spin current [29] that has similar spin polarization as  $\text{Pt}_{\text{top}}$  since Pt and Ta has opposite  $\theta_{SH}$ . One has to note that the  $\text{Pt}_{\text{bottom}}$  layer in Pt stack is directly grown on Si/SiO<sub>2</sub> substrate whereas in Ta stack ( $\text{Pt}'_{\text{bottom}}$ ) it is grown on Ta. It is expected that the quality of the  $\text{Pt}_{\text{bottom}}$  layer in Pt

stack is inferior to the  $\text{Pt}'_{\text{bottom}}$  layer in Ta stack. This in turn indicates that  $J_s^{\text{Pt}'}$  (bottom) –  $J_s^{\text{Ta}}$  (bottom)(for Ta stack)  $\approx J_s^{\text{Pt}}$  (bottom) (for Pt stack). This results in the comparable value of the effective spin current acting on the Co layer for both the stack leading to the similar value of  $H_{AD}$  for both the Pt and Ta stack, respectively. Furthermore, the anisotropy fields also show a drastic enhancement from  $0.34 \pm 0.007$  T (for Pt stack) to  $1.43 \pm 0.063$  T (for Ta stack) after addition of Ta layer. This enhancement is a result of enhance spin-orbit coupling at the interfaces with the addition of Ta layer as reported in the literature[14]. Moreover, the SOT efficiency extracted in this work matches well with the SOT efficient for the similar stacks reported in the literature. The same is depicted in Table I.

<u>Stack(s)</u>	<u>SOT efficiency</u>	<u>Reference</u>
<b>Our work</b>	<b><math>\sim 23 \text{ Oe}/(10^7 \text{ A.cm}^{-2})</math></b>	<b>This paper</b>
SiO <sub>2</sub> ./Pt(2)/Co(0.6)/Pt(5)	$\sim 41 \text{ Oe}/(10^7 \text{ A.cm}^{-2})$	Ref. [16]
SiO <sub>2</sub> /Pt(5)/Co(0.6)/Pt(2)	$\sim 20 \text{ Oe}/(10^7 \text{ A.cm}^{-2})$	
GGG /Pt(2.5)/Co(1.1)/ Pt(5)	$\sim 25 \text{ Oe}/(10^7 \text{ A.cm}^{-2})$	Ref. [15]
SiO <sub>2</sub> /Pt(3.5)/Co(1.1)/Pt(3.5)	$\sim 11 \text{ Oe}/(10^7 \text{ A.cm}^{-2})$	
Pt(3)/Co(0.6)/Pt(1)	$\sim 20 \text{ Oe}/(10^7 \text{ A.cm}^{-2})$	Ref. [30]
Pt(3)/Co(0.6)/Ru(0.6)/Pt(1)	$\sim 40 \text{ Oe}/(10^7 \text{ A.cm}^{-2})$	
Pt(4)/Co(1)/MgO(2)	$\sim 75 \text{ Oe}/(10^7 \text{ A.cm}^{-2})$	Ref. [31]
Pt(5)/Co(1.2)/MgO(5)	$\sim 20 \text{ Oe}/(10^7 \text{ A.cm}^{-2})$	Ref. [32]
Pt(5)/Co(1.2)/Ho(2)/MgO(5)	$\sim 95 \text{ Oe}/(10^7 \text{ A.cm}^{-2})$	

**Table 3.1** Comparison of SOT efficiencies in our stack with the similar stacks reported in the literature.

### 3.3.6 Magnetization switching in Ta-stack

#### 3.3.6.1 Current induced magnetization switching in Ta/Pt/Co/Pt stack

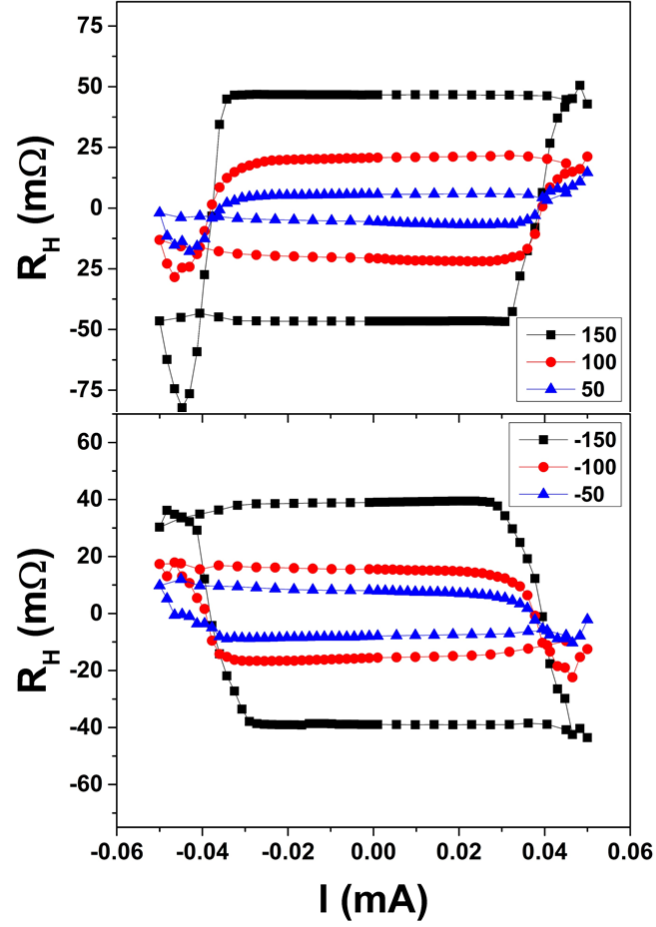


**Figure 3.8** DC Hall resistance as a function of applied current pulse in presence of in-plane applied magnetic field. (Top portion shows plots in presence of positive values of in-plane magnetic field (in Oe) and bottom portion in presence of negative values of in-plane magnetic field (in Oe)).

To see magnetization switching we performed the current induced magnetization experiments in presence of the in-plane symmetry breaking magnetic fields. In this DC measurement technique, a varying current pulse for the duration of 1ms followed by a 60 sec wait time was applied through current channel. Subsequently, the transverse resistance  $R_H$  was measured at 500 $\mu$ A read current in the Delta configuration employing Keithley 2450 source meter and 2182A nanovoltmeter. The experimental results with different in-plane field values are shown in Fig. 3.8. The hysteresis behaviour of  $R_H$  vs.  $I$  plot confirms the significant value of AD-SOT in Ta/Pt/Co/Pt stack.

### 3.3.6.2 Field-free switching in Ta/Pt/Co/Pt stack

Further, we had achieved the field-free magnetization switching by measuring  $R_H$  as a function of DC current pulses. The typical field-free switching behaviour of the Ta stack is demonstrated in Figure 3.9(a). Notably, the field-free switching was achieved for the sample with Co deposited in the wedge form unlike the uniformly deposited Co sample. The measurement of  $R_H^{2\omega}$  for Ta stack as function of out-of-plane applied field ( $H_z$ ) resembles an AHE type of behaviour for our PMA base stack (shown in Figure 3.9(b)). This behaviour is consistent with the ANE signature reported in the literature[23,27]. Similar behaviour of AHE and ANE signifies that ANE can also be used as reading mechanism to probe different magnetization states. Conventionally for detecting the field-free magnetization switching in a PMA sample using DC current, the transverse DC resistance is measured with minute probe current after applying the varying current pulses which were swept from positive to negative magnitude and vice versa. In order to utilize ANE for detecting the magnetization orientation we have devised an AC 2<sup>nd</sup> harmonic technique. In our AC 2<sup>nd</sup> harmonic technique, a current pulse that changes the magnetization state due to AD-SOT is applied and the 2<sup>nd</sup> harmonic Hall signal instead of DC Hall resistance, is measured after the pulse. The writing and reading mechanisms are illustrated in Figure 3.9(c). At first, we have applied a 1ms current pulses with predefined magnitude to change the magnetization state utilizing AD-SOT and wait for 60 sec. The second harmonic Hall resistance ( $R_H^{2\omega}$ ) using 4 mA AC current was measured subsequently. We have taken the average of 30 readings for better signal to noise ratio.

The ANE signal in 2<sup>nd</sup> harmonic Hall measurement shows magnetization dependency as:

$$V^{2\omega,ANE} \propto m \times \nabla T$$

where,  $\nabla T$  is the thermal gradient generated due to the Joule heating of the stack ( $\nabla T \propto I^2$ ) and  $m$  is the magnetization vector of the stack. Since the 2<sup>nd</sup> harmonic Hall voltage is probed along y-direction so the above equation suggests that  $V^{2\omega,ANE}$  must have a following form:

$$V^{2\omega,ANE} \propto (\nabla_x T m_z + \nabla_z T m_x)$$

Here,  $\nabla_x T$  and  $\nabla_z T$  are the temperature gradient along x- and z-directions and  $m_x$  and  $m_z$  are x- and z-component of magnetization, respectively. The  $\nabla_z T$  is generated because of the differences in thermal conductivity of substrate and stack materials. Due to the different width of current and voltage branches, heat conduction occurs differently at the centre of Hall bar and

towards the Hall branches, which generates  $\nabla_x T$ . For our high PMA based Ta stack the  $m_z$  part dominates in above equation. The variation of ANE ( $V^{2\omega, ANE}$ ) vs.  $H_z$  is asymmetric in nature as the ANE signal is odd with respect to the magnetization reversal.

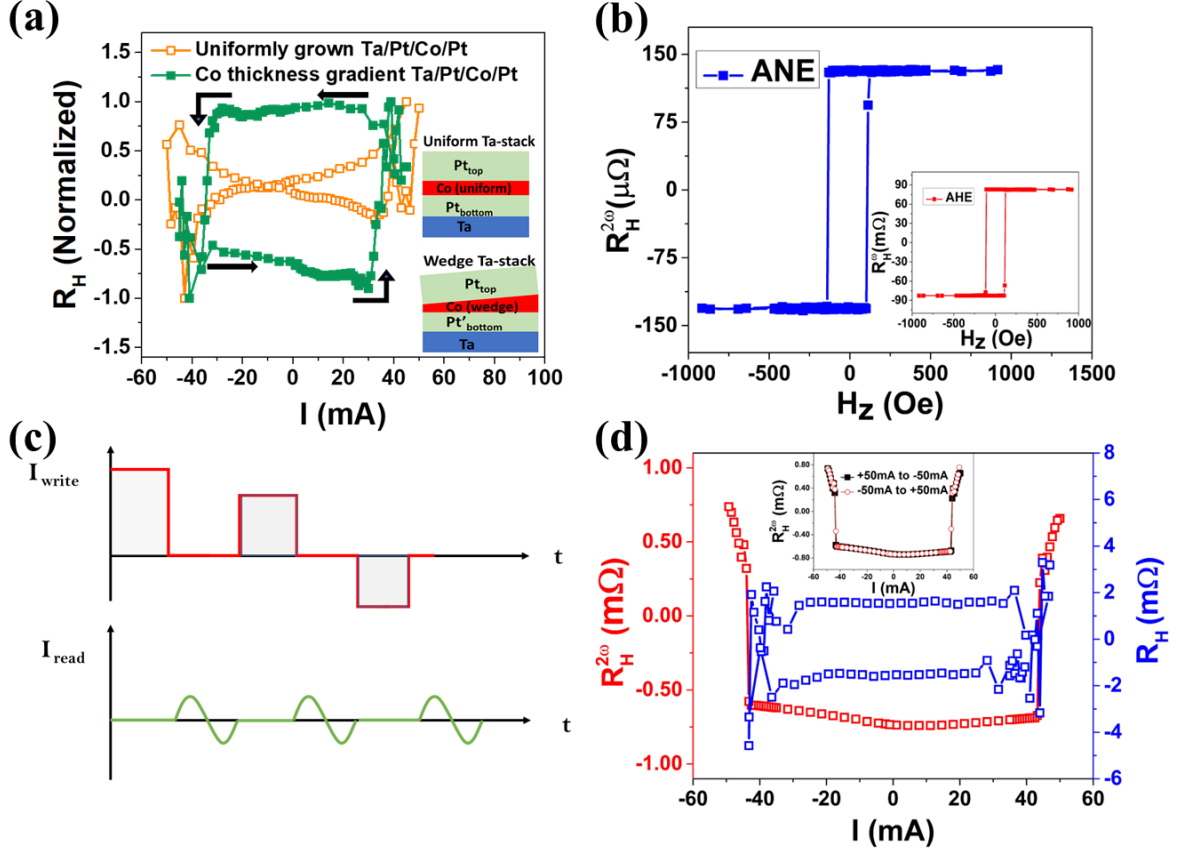


**Figure 3.9(a)**  $R_H$  vs.  $I$  for Ta- stack with Co wedge and uniformly grown Ta stacks (inset: illustration of Co uniform and Co wedge in Ta stack). **(b)**  $R_H^{2\omega}$  (anomalous Hall resistance ( $R_H$ ) in the inset) vs.  $H_z$  for Ta stack. **(c)** Writing and reading scheme for the 2<sup>nd</sup> harmonic ANE based reading mechanism. **(d)**  $R_H^{2\omega}$  (left y-axis) and  $R_H$  (right y-axis) vs. applied current pulses (inset: retracing of  $R_{xy}^{2\omega}$  as a function of applied current pulses).

Further, we have employed our AC 2<sup>nd</sup> harmonic method to detect the field-free switching in Ta stack which exhibit a significant ANE contribution as depicted in Figure 3.5 & 3.9(b). Notably, the significant ANE behaviour is highly reproducible across different devices and stacks (discussed later). Figure 3.9(d) exhibits  $R_{xy}^{2\omega}$  vs. the applied current pulses for Ta stack depicting field-free magnetization switching, employing our method. As expected,  $R_{xy}^{2\omega}$

is symmetric about the current axis and the complete current sweep retraces its nature with two distinct crossover regions where the magnetization switching occurs (inset of Figure 3.9(d)). Using our method, we can restrict the application of the DC pulses until zero while starting from the positive (negative) value. The sensitivity of the proposed methodology was further confirmed by plotting  $R_{xy}^{2\omega}$  vs. the applied current pulses together with the Hall resistance ( $R_H$ ) as a function of DC current as shown in Figure 3.9(d). The switching current estimated to be  $\sim 43$  mA by our method matched well to the conventional DC Hall measurement method.

### 3.3.7 Repeatability of ANE nature in different Ta stacks

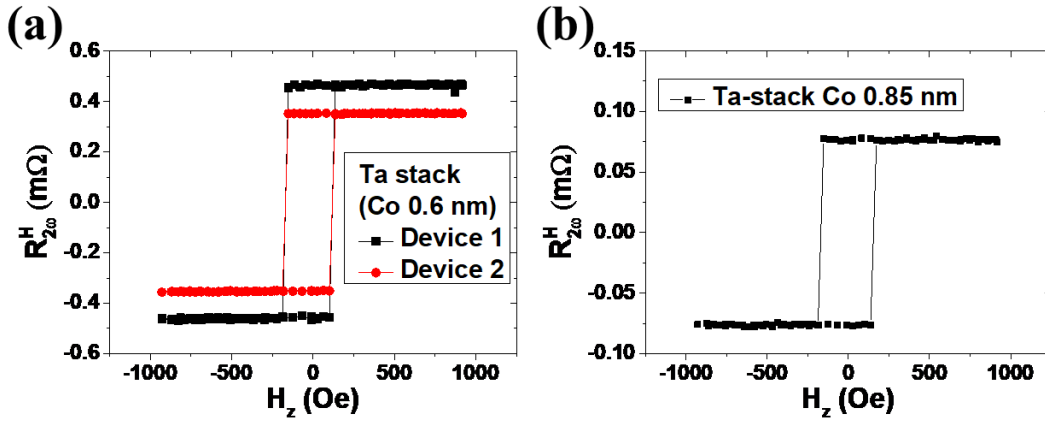


**Figure 3.10:** Hysteric nature of  $R_H^{2\omega}$  vs.  $H_z$  for two different devices of Ta stack with Co thickness 0.6 nm in (a), and for a Ta stack device with Co thickness 0.85 nm in (b).

Figure 3.10 (a) shows the variation of  $R_H^{2\omega}$  vs.  $H_z$  for two different devices of Ta-stack (namely Device 1 and Device 2, respectively) with Co thickness of 0.6 nm. Notably, the Device 1 belong to the same set of devices for which the results are presented in the previous sections. The Device 2 was fabricated at the later stage. It is evident from Figure 3.10 (a) that the hysteric nature (ANE signal) in both the devices remains identical indicating that the ANE signature reported in the manuscript is highly reproducible. The figure 3.10 (b) shows the variation of  $R_H^{2\omega}$  vs.  $H_z$  for Ta stack with Co thickness of 0.85 nm which shows a similar hysteric nature as shown in Figure 3.10 (a) and Figure 3.9 (b) of main text. This leads to the fact that the contact resistivity of the interface between layers does not affect the joule heating and the signal of ANE. [This leads to the fact that thermal gradient generated ANE nature is reproducible in

Pt/Co/Pt stacks with Ta underlayer.] The coercivity difference of  $\sim 20$  Oe in Figure 3.9 (a) and (b) is due to difference in FM layer thicknesses.

### 3.4 Conclusion

In summary, we have investigated the effect of addition of the Ta underlayer to the asymmetric Pt/Co/Pt stack leading to the enhanced perpendicular magnetic anisotropy and emergence of the ANE which was otherwise negligible in the asymmetric Pt/Co/Pt stack. The emergence of the ANE due to the addition of the underlayer in HM-FM heterostructure is important as the contribution of the ANE needs to be separated while measuring the AD-SOT values using low field harmonic Hall method else it would lead to the overestimation of the  $H_{AD}$  values. It was found that FL-SOT torque remains insignificant in both the stacks whereas the AD-SOT exhibits similar magnitude. For estimating AD-SOT torque, we have adopted an angle resolved magnetization rotation technique. Using this methodology, we could quantify the AD-SOT and ANE contributions, respectively. Moreover, we had developed a methodology of detecting field-free switching by utilizing the ANE behaviour present in our sample. In our methodology, the field-free switching as well as the estimation of the switching current can be achieved by sweeping the current from zero to positive (negative) value unlike the full current sweep from positive to negative current values for the DC method. Our result suggests that the addition of Ta to the model Pt/Co/Pt stack leads to the generation of considerable thermoelectric effect coupled with strong PMA which indicates the major role played by the choice of underlayer for future design of the SOT devices.



## References

- [1] K. Garello, C. O. Avci, I. M. Miron, M. Baumgartner, A. Ghosh, S. Auffret, O. Boulle, G. Gaudin, and P. Gambardella, Ultrafast magnetization switching by spin-orbit torques, *Applied Physics Letters* **105**, 212402 (2014).
- [2] I. M. Miron *et al.*, Perpendicular switching of a single ferromagnetic layer induced by in-plane current injection, *Nature* **476**, 189 (2011).
- [3] L. Liu, C.-F. Pai, Y. Li, H. W. Tseng, D. C. Ralph, and R. A. Buhrman, Spin-Torque Switching with the Giant Spin Hall Effect of Tantalum, *Science* **336**, 555 (2012).
- [4] K. Cai *et al.*, Ultrafast and energy-efficient spin-orbit torque switching in compensated ferrimagnets, *Nature Electronics* **3**, 37 (2020).
- [5] A. V. Khvalkovskiy *et al.*, Basic principles of STT-MRAM cell operation in memory arrays, *Journal of Physics D: Applied Physics* **46**, 074001 (2013).
- [6] D. Apalkov, B. Dieny, and J. M. Slaughter, Magnetoresistive Random Access Memory, *Proceedings of the IEEE* **104**, 1796 (2016).
- [7] T. Kimura, Y. Otani, T. Sato, S. Takahashi, and S. Maekawa, Room-Temperature Reversible Spin Hall Effect, *Physical Review Letters* **98**, 156601 (2007).
- [8] J. E. Hirsch, Spin Hall Effect, *Physical Review Letters* **83**, 1834 (1999).
- [9] J. Sinova, S. O. Valenzuela, J. Wunderlich, C. H. Back, and T. Jungwirth, Spin Hall effects, *Reviews of Modern Physics* **87**, 1213 (2015).
- [10] L. Chen *et al.*, Robust spin-orbit torque and spin-galvanic effect at the Fe/GaAs (001) interface at room temperature, *Nature Communications* **7**, 13802 (2016).
- [11] I. M. Miron, P. J. Zermatten, G. Gaudin, S. Auffret, B. Rodmacq, and A. Schuhl, Domain Wall Spin Torquemeter, *Physical Review Letters* **102**, 137202 (2009).
- [12] U. H. Pi, K. Won Kim, J. Y. Bae, S. C. Lee, Y. J. Cho, K. S. Kim, and S. Seo, Tilting of the spin orientation induced by Rashba effect in ferromagnetic metal layer, *Applied Physics Letters* **97**, 162507 (2010).
- [13] C. Zhang, S. Fukami, H. Sato, F. Matsukura, and H. Ohno, Spin-orbit torque induced magnetization switching in nano-scale Ta/CoFeB/MgO, *Applied Physics Letters* **107**, 012401 (2015).
- [14] R. Wang, Z. Xiao, H. Liu, Z. Quan, X. Zhang, M. Wang, M. Wu, and X. Xu, Enhancement of perpendicular magnetic anisotropy and spin-orbit torque in Ta/Pt/Co/Ta multi-

layered heterostructures through interfacial diffusion, *Applied Physics Letters* **114**, 042404 (2019).

[15] H. An, H. Nakayama, Y. Kanno, A. Nomura, S. Haku, and K. Ando, Spin-orbit torques in asymmetric Pt/Co/Pt structures, *Physical Review B* **94**, 214417 (2016).

[16] C. Hin Sim, J. Cheng Huang, M. Tran, and K. Eason, Asymmetry in effective fields of spin-orbit torques in Pt/Co/Pt stacks, *Applied Physics Letters* **104**, 012408 (2014).

[17] S. Woo, M. Mann, A. J. Tan, L. Caretta, and G. S. D. Beach, Enhanced spin-orbit torques in Pt/Co/Ta heterostructures, *Applied Physics Letters* **105**, 212404 (2014).

[18] L. Zhu, D. C. Ralph, and R. A. Buhrman, Spin-Orbit Torques in Heavy-Metal--Ferromagnet Bilayers with Varying Strengths of Interfacial Spin-Orbit Coupling, *Physical Review Letters* **122**, 077201 (2019).

[19] M. Hayashi, J. Kim, M. Yamanouchi, and H. Ohno, Quantitative characterization of the spin-orbit torque using harmonic Hall voltage measurements, *Physical Review B* **89**, 144425 (2014).

[20] J. Kim, J. Sinha, M. Hayashi, M. Yamanouchi, S. Fukami, T. Suzuki, S. Mitani, and H. Ohno, Layer thickness dependence of the current-induced effective field vector in Ta|CoFeB|MgO, *Nature Materials* **12**, 240 (2013).

[21] T. Shirokura and P. N. Hai, Angle resolved second harmonic technique for precise evaluation of spin orbit torque in strong perpendicular magnetic anisotropy systems, *Applied Physics Letters* **119**, 222402 (2021).

[22] H. Yang, H. Chen, M. Tang, S. Hu, and X. Qiu, Characterization of spin-orbit torque and thermoelectric effects via coherent magnetization rotation, *Physical Review B* **102**, 024427 (2020).

[23] K. Garello *et al.*, Symmetry and magnitude of spin-orbit torques in ferromagnetic heterostructures, *Nature Nanotechnology* **8**, 587 (2013).

[24] J. Yu, X. Qiu, W. Legrand, and H. Yang, Large spin-orbit torques in Pt/Co-Ni/W heterostructures, *Applied Physics Letters* **109**, 042403 (2016).

[25] C. O. Avci, K. Garello, A. Ghosh, M. Gabureac, S. F. Alvarado, and P. Gambardella, Unidirectional spin Hall magnetoresistance in ferromagnet/normal metal bilayers, *Nature Physics* **11**, 570 (2015).

[26] C. O. Avci, K. Garello, M. Gabureac, A. Ghosh, A. Fuhrer, S. F. Alvarado, and P. Gambardella, Interplay of spin-orbit torque and thermoelectric effects in ferromagnet/normal-metal bilayers, *Physical Review B* **90**, 224427 (2014).

- [27] S. Tu *et al.*, Anomalous Nernst effect in Ir<sub>22</sub>Mn<sub>78</sub>/Co<sub>20</sub>Fe<sub>60</sub>B<sub>20</sub>/MgO layers with perpendicular magnetic anisotropy, *Applied Physics Letters* **111**, 222401 (2017).
- [28] M.-H. Nguyen, D. C. Ralph, and R. A. Buhrman, Spin Torque Study of the Spin Hall Conductivity and Spin Diffusion Length in Platinum Thin Films with Varying Resistivity, *Physical Review Letters* **116**, 126601 (2016).
- [29] H. Gamou, Y. Du, M. Kohda, and J. Nitta, Enhancement of spin current generation in epitaxial  $\alpha$ -Ta/CoFeB bilayer, *Physical Review B* **99**, 184408 (2019).
- [30] Y. Wu, K. Meng, J. Miao, X. Xu, and Y. Jiang, Enhanced spin-orbit torque in Pt/Co/Pt multilayers with inserting Ru layers, *Journal of Magnetism and Magnetic Materials* **472**, 14 (2019).
- [31] C.-F. Pai, M. Mann, A. J. Tan, and G. S. D. Beach, Determination of spin torque efficiencies in heterostructures with perpendicular magnetic anisotropy, *Physical Review B* **93**, 144409 (2016).
- [32] T. Jin, W. C. Law, D. Kumar, F. Luo, Q. Y. Wong, G. J. Lim, X. Wang, W. S. Lew, and S. N. Piramanayagam, Enhanced spin-orbit torque efficiency in Pt/Co/Ho heterostructures via inserting Ho layer, *APL Materials* **8**, 111111 (2020).

## Chapter 4

# Multistate memory behavior of SOT induced magnetization switching in presence of an external field

### 4.1 Introduction

With its non-volatile nature, fast switching capabilities, and low power consumption, spin-orbit torque (SOT) emerges as a promising writing mechanism for spintronics memory devices[1,2]. In recent years, significant efforts are made towards the understanding and applications of SOT based multistate memory or memristor devices, suitable for neuromorphic computing and processing in-memory application[3-5]. Conventional Von Neumann memory architecture suffers from data shuttling problem between processor and memory, leading to increased energy consumption[6]. A solution to this problem is processing the data locally in memory akin to the operation of brain. Brain-like or neuromorphic computing replicates the operations of neuron and synapses in brain, where neurons transfer the information through synapses[3]. Here, each information is assigned a different weight. Therefore, to emulate the functioning of synaptic weight a multivalued, non-volatile memory is required. Significant efforts are made to the realization of multistate memory or memristor nature via material engineering in magnetic heterostructures[7-11]. However, a lack in fundamental experimental approach to achieve memristor behavior is still lacking.

Here, we utilized combined symmetry of SOT and DC field to stabilize multistate in our stacked device. Further, we verified that the integration of SOT with a static field could yield multiple metastable saturation states, characterized by magnitudes and polarity of static field. Furthermore, our finding suggests that this phenomenon is induced by both SOT and field simultaneously. This effect enables the manipulation of energy barrier between states. At last, our measurements try to resolve the initialization problem of modern memristor devices through experimental demonstration of initialization-free multistate memory.

## 4.2 Effect of external field ( $H_z$ ) on SOT

In this section we explored the possibility of altering the spin Hall effect generated anti-damping like torque by an application of external field. In a simple macrospin picture, spin Hall effect (SHE) in heavy metal (HM) layer is considered as the source of spin current which interacts with the magnetization ( $\mathbf{m}$ ) of adjacent ferromagnetic layer (Fig. 4.1a). Magnetization dynamics or the time evolution of magnetization in presence of SOTs can be understood by the Landau-Lifshitz-Gilbert (LLG) equation[12]:

$$\frac{\partial \mathbf{m}}{\partial t} = -\gamma \mathbf{m} \times \mathbf{H}_{eff} + \alpha \mathbf{m} \times \frac{\partial \mathbf{m}}{\partial t} + \gamma H_{AD} \mathbf{m} \times (\mathbf{m} \times \boldsymbol{\sigma}) \quad (4.1)$$

Here,  $\gamma$  is gyromagnetic ratio,  $\boldsymbol{\sigma}$  ( $\parallel y$ ) is spin current polarization and  $H_{AD}$  been anti-damping effective field produced by SHE. FM magnetization  $\mathbf{m}$  ( $m_x, m_y, m_z$ ) can be denoted by  $(\theta, \varphi)$  coordinates (schematic of system is in Fig. 4.1a). To achieve a deterministic switching an in-plane symmetry breaking field ( $H_x$ ) along the current direction ( $\parallel x$ ) is applied. Additionally, we incorporated an out-of-plane external field ( $H_z$ ) to explore its effect on the current generated  $H_{AD}$  field. The effective field  $\mathbf{H}_{eff}$  in Eq. (1), other than  $H_x$  and  $H_z$ , has an anisotropy field contribution ( $H_k$ ). Therefore, the  $\mathbf{H}_{eff}$  is written as:

$$\mathbf{H}_{eff} = (H_x, 0, H_k \cos\theta + H_z) \quad (4.2)a$$

The magnetization in spherical polar coordinates is defined by

$$\mathbf{m} = (\sin\theta \cos\varphi, \sin\theta \sin\varphi, \cos\theta) \quad (4.2)b$$

The polarization of spin is current is:

$$\boldsymbol{\sigma} = (0, 1, 0) \quad (4.2)c$$

An illustration of above-mentioned system is shown in Fig. 4.1. For the stationary state solution of Eq. (4.1),  $\frac{\partial \mathbf{m}}{\partial t} = 0$

$$\Rightarrow -\mathbf{m} \times \mathbf{H}_{eff} + H_{AD} \mathbf{m} \times (\mathbf{m} \times \boldsymbol{\sigma}) = 0 \quad (4.3)$$

Using Eq. (4.2) in Eq. (4.3) and equate each component of  $\hat{x}$ ,  $\hat{y}$ ,  $\hat{z}$  to zero.

$$\sin\theta \sin\varphi (-H_z + H_{AD} \sin\theta \cos\varphi - H_k \cos\theta) = 0 \quad (4.4)$$

$$-H_{AD}\cos^2\theta + \sin\theta \cos\varphi(H_z - H_{AD}\sin\theta \cos\varphi) + H_K \cos\theta \sin\theta \cos\varphi - H_x \cos\theta = 0 \quad (4.5)$$

$$\sin\theta \sin\varphi(H_{AD} \cos\theta + H_k) = 0 \quad (4.6)$$

During SOT switching  $m_y \sim 0$ , hence,  $\varphi = 0$ ,

Further,  $\varphi = 0$  makes Eq. (4.4) & (4.6) self-evident and Eq. (4.5) became:

$$-H_{AD}\cos^2\theta + \sin\theta (H_z - H_{AD}\sin\theta) + H_K \cos\theta \sin\theta - H_x \cos\theta = 0$$

From here  $H_{AD}$  is determined as:

$$h_{AD} = h_z \sin\theta + \cos\theta(\cos\theta - h_x) \quad (4.7)$$

Here,  $h_{AD}$ ,  $h_z$ , and  $h_x$  are  $H_{AD}$ ,  $H_z$ , and  $H_x$  fields, respectively which are scaled by  $H_k$ .

i.e.,  $h_{AD} = H_{AD}/H_k$ ,  $h_z = H_z/H_k$ , and  $h_x = H_x/H_k$

To find the values of  $\sin\theta$  and  $\cos\theta$  we find the local minima/maxima of Eq. (4.7)

Which gives

$$4\sin^2\theta + 4h_x \sin^3\theta + (h_x^2 + h_z^2 - 4)\sin^2\theta + 2h_x \sin\theta + (1 - h_z^2) = 0 \quad (4.8)$$

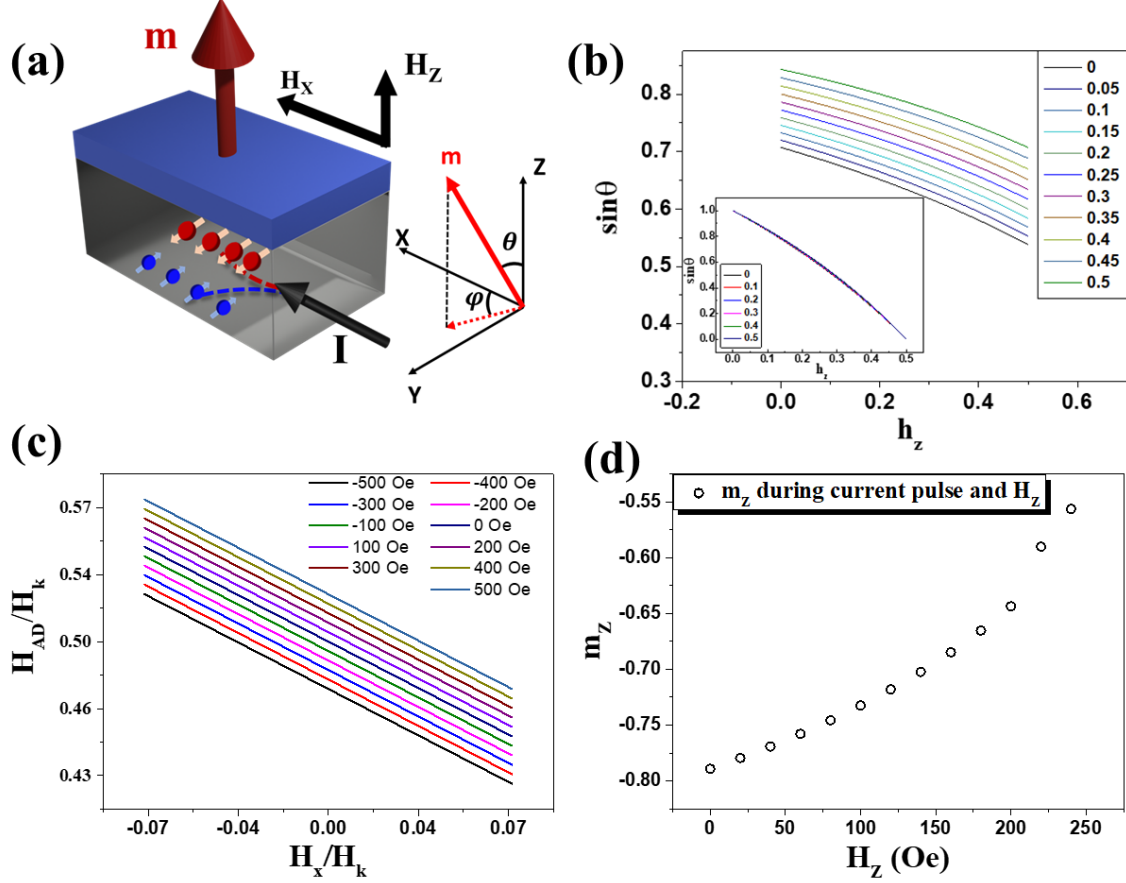


**Figure 4.1** (a) FM/HM model system with coordinate geometry. In-plane current through HM and external fields along x- and z- directions ( $H_x$  and  $H_z$ , respectively) are applied. (b) Root of Eq. (4.8) as a function of  $h_z$  ( $=H_z/H_k$ ). Here, various line plots represent the  $\sin\theta$  vs.  $h_z$  plot for a fix value of  $h_x$  ( $=H_x/H_k$ ) (numeric values of  $h_x$  are written to the right side of plot). Inset: normalized  $\sin\theta$  vs.  $h_z$  plot for different values of  $h_x$ . (c)  $H_{AD}$  value from Eq. (4.10) as a function of  $H_x$  in presence of different  $H_z$  values. (d) Results of micromagnetic simulation showing the trend of change in magnetization z-component ( $m_z$ ) during the action of  $H_z$  and a 4 nS current pulse.

We obtained the graphical solution of Eq. (4.8) in the form of  $\sin\theta$ . Further, we plotted only those roots where  $\theta \rightarrow 90^\circ$  for a fix  $h_x$  and varying  $h_z$  (shown in Fig. 4.2(a)). Now, if we plot these roots as a function of  $h_z$  at various values of  $h_x$  (as shown in Fig. 4.2(a)), the point corresponding to  $h_z=0$  coincide with  $\frac{1}{4}\left(h_x + \sqrt{h_x^2 + 8}\right)$  which is the solution for  $\sin\theta$ , if we consider  $h_z=0$  in Eq. (4.7). Until the  $h_x, h_z = 0.5$  limit these plots follow similar trends. It is

noteworthy that the  $h_x, h_z < 0.5$  condition hold for PMA material from the experimental point of view[12]. This is shown in Fig. 4.2(a). It is evident from the graph that the fitted solution of graph must be added to the  $h_z=0$  solution of  $\sin\theta$  which is  $\frac{1}{4}\left(h_x + \sqrt{h_x^2 + 8}\right)$ . We fit this equation with a polynomial of degree  $n$ , however to a good approximation we can neglect second and higher order terms (as  $h_x, h_z \ll 1$  since  $H_k \gg H_x, H_z$ ). Incorporating the obtained value of  $\sin\theta$  and  $\cos\theta$  in Eq. (4.7) with  $h_x, h_z \ll 1$  approximation yields the solution

$$h_{AD} = \frac{(h_z - h_x)}{\sqrt{2}} + \frac{1}{2} \quad (4.9)$$

Eq. (4.9) is the solution for anti-damping like torque effective field when an additional field  $H_z$  is applied. Further, for  $h_z=0$ , Eq. (4.9) reduces to its previous form as calculated in Ref [12,13].

Therefore, from the steady state solution of Eq. (4.1) the SHE induced field can be derived as:

$$H_{AD} = \frac{1}{\sqrt{2}}(H_z - H_x) + \frac{H_{k,eff}}{2} \quad (4.10)$$

The graphical representation of Eq. (4.10) is shown in Fig. 4.1(c) where  $H_{AD}$  been plotted against  $H_x$  for different values of  $H_z$ . In Fig. 4.1(c) field values were scaled by  $H_{k,eff}$ . Here, the value of  $H_{k,eff}$  is taken as a real value of 1.4 T from our previous work[14] (chapter 3). Remarkably, the  $H_z=0$  case replicates the previous results where  $H_z$  was not taken into account. However, a non-zero  $H_z$  value shows change in  $H_{AD}$ . These results suggest that the application of  $H_z$  can modify the effect of SHE induced field and hence the switching state of magnetization. To verify this, we perform micromagnetic simulations on  $100 \times 100 \times 0.6 \text{ nm}^3$  sample with Pt/Co/Pt material stack parameters. Magnetization state was recorded during simultaneous effect of a 4 nS current pulse and an application of  $H_z$  field. Here, the recorded values are attributed to the magnetization state that results from sufficiently long current pulse, where no further changes in magnetization dynamics occur during this pulse. We observe a reduction in magnetization states (Fig. 4.1(d)) with increasing magnitude of  $H_z$ . This is a direct outcome of Eq. (4.10) which suggest that application of out-of-plane field during current pulse can modify the current induced effective field and hence can possibly stabilize different intermediate state.

### 4.3 Multi-state memory behavior in HM/FM/HM stack



### 4.3.1 Sample alignment

Graphical solution of Eq. (4.10) suggest that a small value of out-of-plane field ( $H_z$ ) is sufficient to alter the values of anti-damping spin-orbit torque (AD-SOT). Therefore, before performing any SOT-induced magnetization switching experiment in presence of  $H_x$  and  $H_z$ , a near perfect alignment of sample with  $H_x$  is inevitable. During the necessary application of in-plane field along current direction ( $H_x$ ), a small misalignment of applied ( $H_{ext}$ ) will result as an out-of-plane component of field ( $H_{ext,z}$ ) which will add/subtract with the externally applied  $H_z$ . Consequently, the additional  $H_{ext,z}$  generated as a misaligned component of  $H_{ext}$  would misinterpret the effect of externally applied  $H_z$  on SOT-induced magnetization switching. A near perfect alignment of sample with the external field in the device plane field is achieved with the help of transport measurements. The misalignment angle ( $\theta$ ) defines the direction (outward/inward) direction of  $H_{ext,z}$  component arising from  $H_{ext}$  (Fig. 4.2(a)). Further, initial different direction of  $H_{ext,z}$  component arose from  $H_{ext}$  ( $\theta > 0$  or  $\theta < 0$ ) will lead to different polarity of  $V_H$  vs.  $H_{ext}$  plot (Fig. 4.2 (b) and (c)). Furthermore, between these two hysteresis polarities  $\theta = 0$  or a near perfect alignment can be situated.

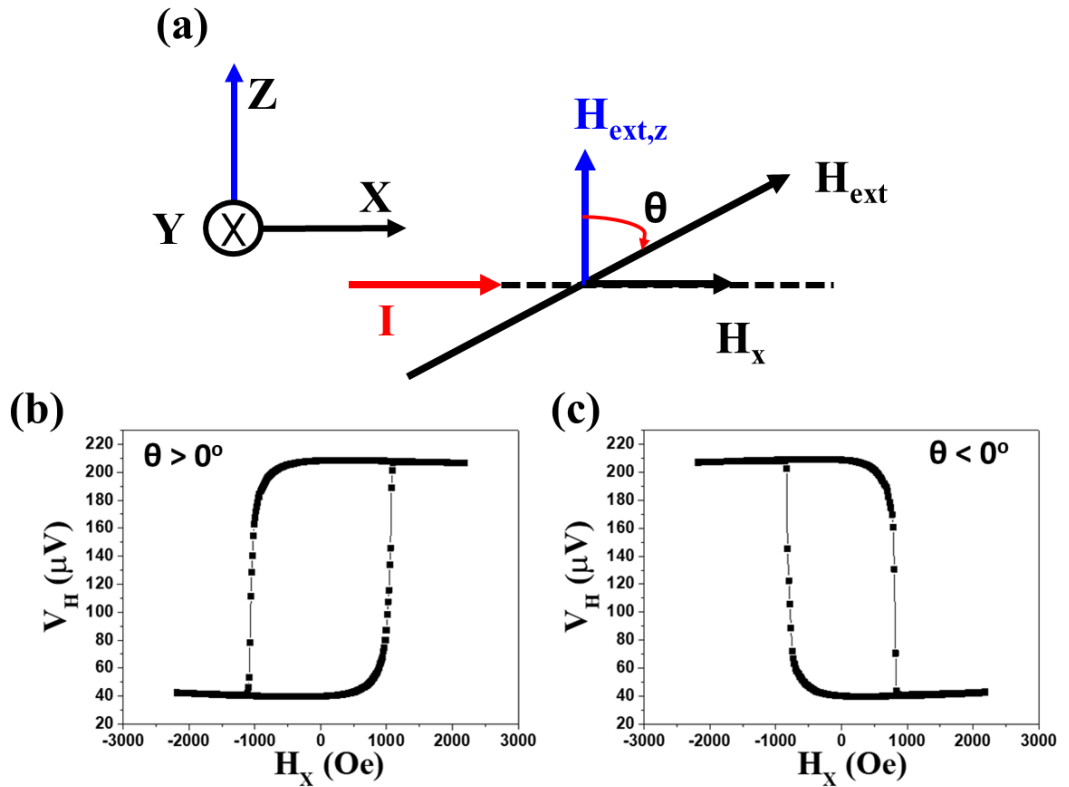


**Figure 4.2 (a)** Misalignment ( $\theta$ ) between applied field ( $H_{\text{ext}}$ ) and current direction producing in-plane and out of plane component of  $H_{\text{ext}}$ . Polarity of hysteresis depending on the component of  $H_{\text{ext}}$  produced by **(b)**  $\theta > 0^\circ$ , and **(c)**  $\theta < 0^\circ$ .

### 4.3.2 Multistate SOT switching

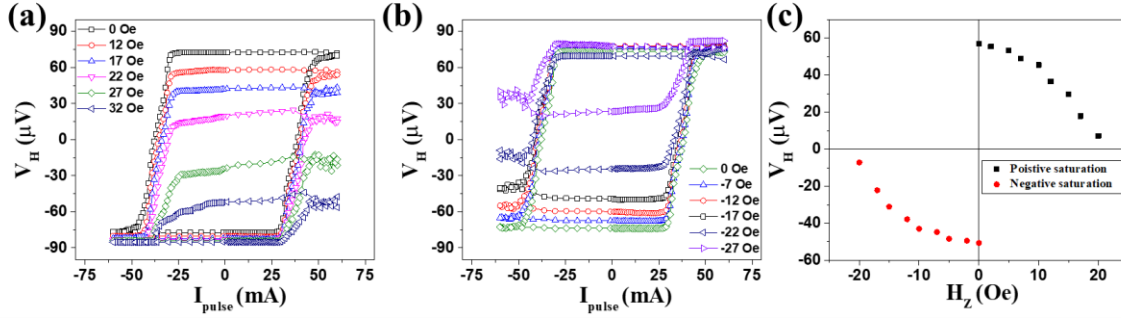


**Figure 4.3** SOT switching in presence of **(a)** negative and **(b)** positive  $H_z$  fields showing memristor behavior. **(c)** Trend of reduction of saturation state in SOT switching in presence of different  $H_z$  magnitude and polarity.

For the experimental verification, in the work reported here, Si/SiO<sub>2</sub>/Ta(3 nm)/Pt(3 nm)/Co(0.6 nm)/Pt(6 nm) stack consisting perpendicular magnetic anisotropy (PMA) is used. The reason for selecting Pt/Co/Pt system for this study is twofold: Pt/Co/Pt exhibit a strong PMA which is a necessary requirement for the highly dense state-of-the-art memory devices. Additionally, Pt/Co/Pt is one of the earliest model systems for PMA studies thereby expanding the potential applicability of the current results. The anti-damping-like torque (AD-SOT) component of SOT, which is the responsible contribution for the SOT switching, is obtained through harmonic Hall measurements in our previous work[14]. Here, SOT induced magnetization switching experiments were conducted with a 100  $\mu\text{S}$  current pulse ( $I_{\text{pulse}}$ ) applied along x-direction. For SOT switching a necessary assistance of magnetic field is required to compensate the effective field of Dzyaloshinskii-Moriya interaction (DMI). Therefore, a symmetry breaking field was applied along the current direction ( $H_x$ ). Notably, while performing SOT switching experiments, the introduction of an additional field in a direction perpendicular to the sample plane ( $H_z$ ) leads to the emergence of an analogue switching behavior (Shown in Fig. 4.3 (a) and (b)). Here, in Fig. 4.3(a) and (b),  $H_x \sim 900$  Oe and  $H_z$  are of positive and negative polarities, respectively. Note that the magnitude of  $H_z$  is always less than coercive field of the stack. After each pulses the magnetization states are measured using conventional AHE reading

mechanism. AHE signal ( $V_H$ ) is proportional to the weighted average of z-component of magnetization ( $m_z$ ) in the sample. Further, the application of a small  $+H_z$ , less than the coercivity field ( $H_c$ ), fixes the  $+m_z$  states whereas  $-m_z$  saturation show an analogue reduction. Similarly, for  $-H_z$  ( $|H_z| < |H_c|$ ) the  $+m_z$  saturation shows a shrink while  $-m_z$  saturation state remains constant. Furthermore, the changes in saturation states are more prominent with increasing magnitude of  $H_z$ . The overall trend of state reduction with  $H_z$  is shown in Fig. 4.3(c). These results show a similar trend as obtained by micromagnetic simulation which verifies that the saturation state reduction is an outcome of  $H_{AD}$  reduction. Our results shows that the manifestation of multistate or memristor-like behavior that does not require any additional material engineering could find extensive application in the field of neuromorphic computation and other spintronics logic devices.

#### 4.4 Stabilization of domain states and presence of Néel domain walls

Although the macrospin formulation shows a good agreement with the experimental results, however, magnetization reversal in our Pt/Co/Pt stack occur through the nucleation of reversed domain and their propagation throughout the sample.

##### 4.4.1 Presence of domain states

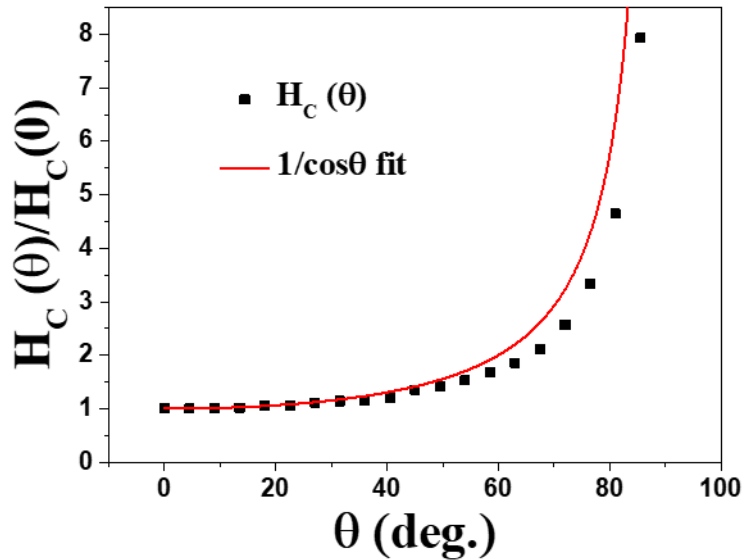


**Figure 4.4** Switching field ( $H_c$ ), scaled by value of  $H_c$  when field is out of plane to the sample ( $H_c(0)$ ) and plotted as a function of angle of external field from z-axis ( $\theta$ ) (refer to Fig. 4.2 (a)).

To prove that the domain state prevails in the Pt/Co/Pt stack during SOT switching in presence of  $H_z$  we first try to analyze the magnetization reversal process in the stack. The two possible reversal mechanisms are: (a) coherent rotation of magnetization described by Stoner-Wohlfarth model[15], and (b) magnetization reversal by domain nucleation and its propagation described by Kondorsky model [16]. To verify that domain nucleation and propagation as the reversal mechanism we measured switching field  $H_c$  as a function of polar angle  $\theta$ . Obtained value  $H_c(\theta)/H_c(0^\circ)$  are well fitted by  $1/\cos\theta$  function (Fig. 4.4), similar to the previous reports[17,18]. The  $H_c(\theta) = H_c(0^\circ)/\cos\theta$  verifies the Kondorsky model and hence the reversal mechanism as domain nucleation and propagation. Therefore, Kondorsky model confirms the presence of domain states in our Pt/Co/Pt system. Furthermore, with symmetry breaking field Néel domain state stabilizes in Pt/Co/Pt, we have discussed this in the succeeding section.

#### 4.4.2 Presence of Néel domain walls

We verified that the magnetization switching is govern by domain dynamics by fitting the angle dependent coercive field ( $H_c$ ) values by Kondorsky model. Therefore, the reduced saturated values of  $+m_z$  ( $-m_z$ ) for  $-H_z$  ( $+H_z$ ) are the attributes of intermediate domain states.

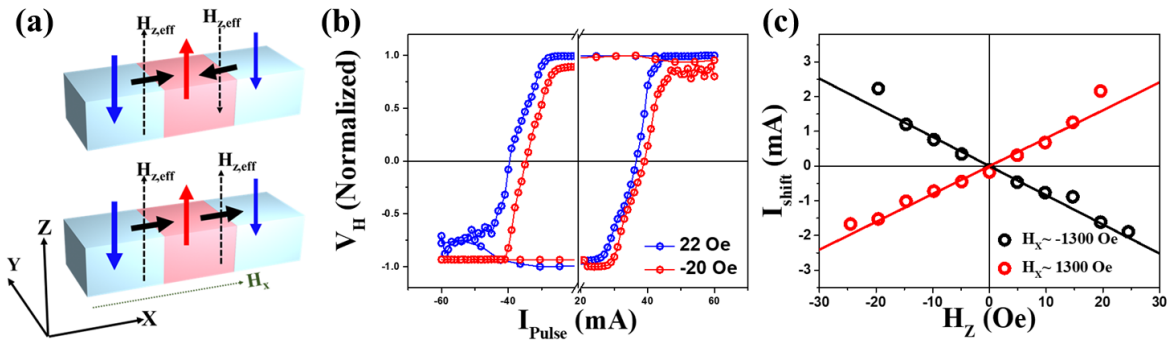


**Figure 4.5.** (a), Out of plane effective SOT field ( $H_{z,eff}$ ) acting on chiral and achiral DW. SOT induces chiral Néel wall motion (top). Contraction/expansion of DW by SOT, inducing magnetization switching depending on  $H_x$  polarity (bottom). (b) SOT loop shift as a consequence of  $\pm H_z$ . Here, a symmetry breaking field  $H_x \sim 1300$  Oe was also applied. (c) Linear trend of SOT induced hysteresis loop shift as a function of  $H_z$ . Linear plots with different slopes attributes to the different polarity of  $H_x$ .

In domain wall (DW) assisted switching, the deterministic switching is achieved by breaking the chiral symmetry of Néel DW through the application of a symmetry breaking field along current direction ( $H_x$ )[17,19,20]. By applying  $H_x$ , the in-plane projection of magnetization in DW tries to align along the in-plane field direction. Further, to fully align the DW moments along  $H_x$  a minimum field of Dzyaloshinskii–Moriya interaction (DMI) must be compensated (i.e.,  $H_x > H_{DMI}$ )[19]. The DMI sets a chirality in DW (Fig 4.5 (a)) and  $H_x > H_{DMI}$  overcomes this chirality and fix DW magnetization along current direction. On these achiral DW, AD-SOT acts as an effective field along z-direction ( $H_{z,eff}$ ), defined by  $H_{z,eff} \propto (m \times \sigma) \sim m_x \times \sigma$ . Here,  $m_x$  is the x-component of DW moment ( $m$ ) and  $\sigma$  is the spin polarization direction ( $\parallel y$ ). Therefore, AD-SOT leads to an asymmetric motion of the achiral Néel DW and eventually leads to the deterministic magnetization reversal[19,21] (Fig. 4.5(a)). Charge current applied in plane to the magnetic heterostructure generates  $H_{z,eff}$  whose magnitude and direction depends on magnitude of current and DW profile[19,22]:

$$H_{z,eff} = \chi_{AD} \cos \varphi_{DW} J_e \quad (4.11)$$

Where  $\chi_{AD}$  is AD-SOT efficiency and  $\varphi_{DW}$  corresponds to the angle between current direction and DW magnetization. Further,  $\chi_{AD}$  is defined as:

$$\chi_{AD} = \frac{\pi}{2} \left( \frac{\hbar \theta_{SH}}{2e\mu_0 M_S t} \right) \quad (4.12)$$

Here,  $\theta_{SH}$  is spin Hall angle,  $M_S$  corresponds to saturation magnetization and  $t$  is the thickness of ferromagnetic layer.

Utilizing this, SOT efficiency can be determined. For that, an in-plane field ( $H_x$ ) is applied to fix the  $m_x$  in DW followed by the measurement of hysteric behavior of AHE signal with respect to the out-of-plane field ( $H_z$ ). Further, depending on the magnitude of applied current, magnitude of  $H_{z,eff}$  varies. This magnitude is measured as an offset of hysteresis centroid along  $H_z$  axis. Furthermore, the measured  $H_{z,eff}$  follows a linear trend with the applied current. Moreover, this explanation of SOT also suggests that if a current induced switching hysteresis is recorded in presence of a constant  $H_z$ , then the current induced switching hysteresis would also shift along the current axis. This is in accordance with Eq. (4.11), which implies that the additional applied field  $H_z$  would act as an offset along current axis as well. In this case, applied  $H_z$  should be equivalent to the  $H_{z,eff}$  produced by shifted current value. Therefore, the shift in

deterministic switching scheme in presence of  $H_z$  is an outcome of the chirality broken Néel DW present in the system.

Our experimental results show a shift in current assisted switching loop in presence of a constant  $H_z$  field. In Fig. 4.5 (b) the shift of loop is opposite for different polarity of the  $H_z$  ( $H_z = +22$  Oe, and  $-20$  Oe) at a fixed value of symmetry breaking field  $H_x \sim 1300$  Oe. This loop shift in SOT current axis shows a linear trend with respect to  $H_z$  field. Additionally, the polarity of slope within this linear trend is determined by the polarity of applied  $H_x$  field. Fig. 4.5 (c) shows linear trends of shifted current values with  $H_z$  field and polarity of this linear nature is opposite for  $H_x \sim +1300$  Oe, and  $-1300$  Oe. In presence of chirality broken Néel DW, results in Fig. 4.5(c) are an outcome of Eq. (4.11). Therefore, these results validate the presence of Néel DW in our stack.

As the SOT switching process is a thermally activated process, meaning, current pulse in presence of  $H_x$  field nucleates reversed domain and their propagation is facilitated through thermally assisted DW depinning. Application of a DC field  $+H_z$  (+ sign defines the direction of  $H_z$  along  $+z$  direction) adds or subtract with the SOT effective field  $H_{z,eff}$  depending upon the current polarity. For  $+I_{pulse}$ ,  $H_{z,eff}$  is along  $+z$  and hence net effective field of SOT and applied DC sums up and favours  $+m_z$  saturation state. However, as the polarity of current pulse reversed ( $-I_{pulse}$ ) the resultant field of SOT and applied DC field reduces. The resultant (reduced) field along  $-z$  direction does not favor a complete saturation along  $-m_z$  (i.e.,  $m_z < -1$ ) and hence a domain state is stabilized. The reduction of  $-m_z$  in this case depends on the magnitude of  $H_z$ . Conversely,  $+m_z$  state saturation is reduced in case of  $-H_z$ . While the macrospin model predicts the diminishing of the SOT field, the practical scenario, where domain dynamics plays a more significant role, results in the emergence of multiple intermediate saturation states as a consequence of the reduced SOT field.

## 4.5 Energy barrier reduction with states

Further, to confirm that the multistate phenomena is an outcome of both SOT current and out of plane field we obtain the energy landscape of SOT switching by using Arrhenius fitting. We measured SOT induced switching hysteresis at each  $H_z$  by applying current with different pulse widths and considering that saturation states for each  $H_z$  are separated by an energy barrier  $E_b$ .

Obtained critical switching currents ( $I_c$ ) at different pulse width ( $\tau_p$ ) are then fitted using[23,24]:

$$I_c = I_{c0} \left[ 1 - \frac{k_B T}{E_b} \ln \left( \frac{\tau_p}{\tau_0} \right) \right] \quad (4.13)$$

Here,  $I_{c0}$  is critical current value at temperature  $T=0$  K,  $\tau_0$  is the attempt switching time, considered 1 nS. For a fix value of  $H_z=7$  Oe the fitting of Eq. (4.13) is shown in the inset of Fig. 4.6(a).

Obtained energy barrier values from the fitting of Eq. (4.13) with respect to different  $H_z$  are plotted in Fig. 4.6 (a). The empirical form of energy barrier in presence of magnetic field  $H_z$  and current  $J$  is[25,26]:

$$E_b(J, H) = E_b(0) - a(H - \varepsilon J) + a\mu J - cJ^2 \quad (4.14)$$

Here,  $E_b(0)$  is the barrier depth  $-aH$  is the contribution of Zeeman energy,  $\varepsilon J$  is the field-like contribution of SOT, which directly modifies  $H$  by  $H - \varepsilon J$ . The quadratic term in  $J$  is the contribution of AD-SOT term. Since we have experimentally verified that the current values produce SOT effective field with a SOT efficiency factor (Eq. (4.11)), hence similar to the inclusion of the field like term  $J$  in last term can be transform to  $J - \frac{1}{\chi_{AD}} H_z$ . Therefore, above equation can be rewritten as:

$$E_b(J, H) = E_b(0) - a(H - \varepsilon J) + a\mu J - c \left( J - \frac{1}{\chi_{SOT}} H_z \right)^2 \quad (4.15)$$

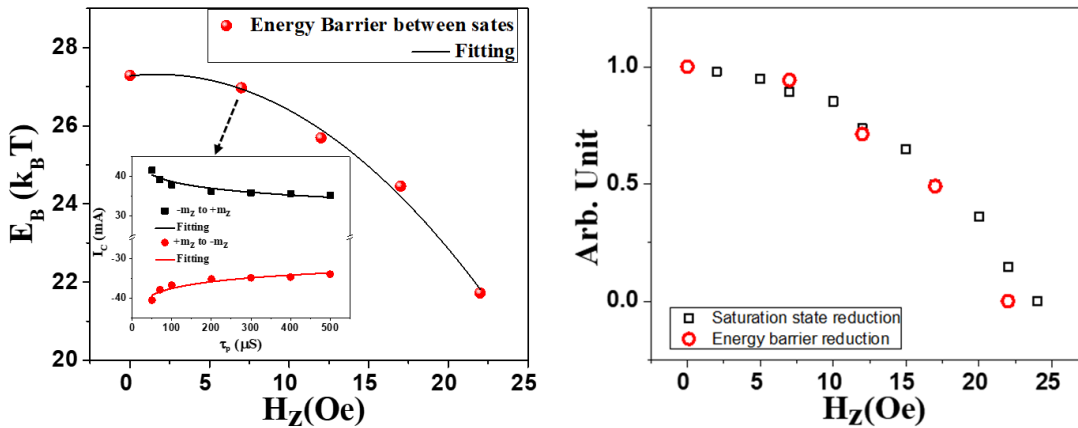


**Figure 4.6 (a)**, Energy barrier (red points) obtained from the Arrhenius fitting Eq. (4.13) at different  $H_z$  field values (Inset: Representative case for the fitting of Eq. (4.13) when  $H_z = 7$  Oe). Energy barrier modification with respect to the  $H_z$  field is well fitted by Eq. (4.15) (black line). **(b)** Comparison of energy barrier (red circle) reduction and reduction of saturation states (black square) as a function of  $H_z$ .

Obtained data is well fitted using above equation justifies that the energy barrier modification with applied field is an outcome of both field and SOT current.

On comparing the normalized data of the energy barrier and the reduced saturation state, we found striking similarities in their trends. This finding implies that saturation states, after applying  $H_z$ , also follows a quadratic trend, similar to energy barrier. Moreover, it is worth noting that reduction of energy barrier with magnetic states could offer a potential solution for modifying the energy barrier to a level where thermal switching becomes feasible. In more straightforward terms, these findings could pave an alternate way for stochastic switching devices. These devices could be realized by simply manipulating the barrier with an applied field, eliminating the need for extensive material growth optimization. Furthermore, the energy barrier is reduced by  $\sim 18\%$  from  $H_z = 0$  Oe to 23 Oe, until this point, we observed 9 different states. Hence the retention time reduced minimally after a large number of states.

## 4.6 Initialization free multistate behaviour



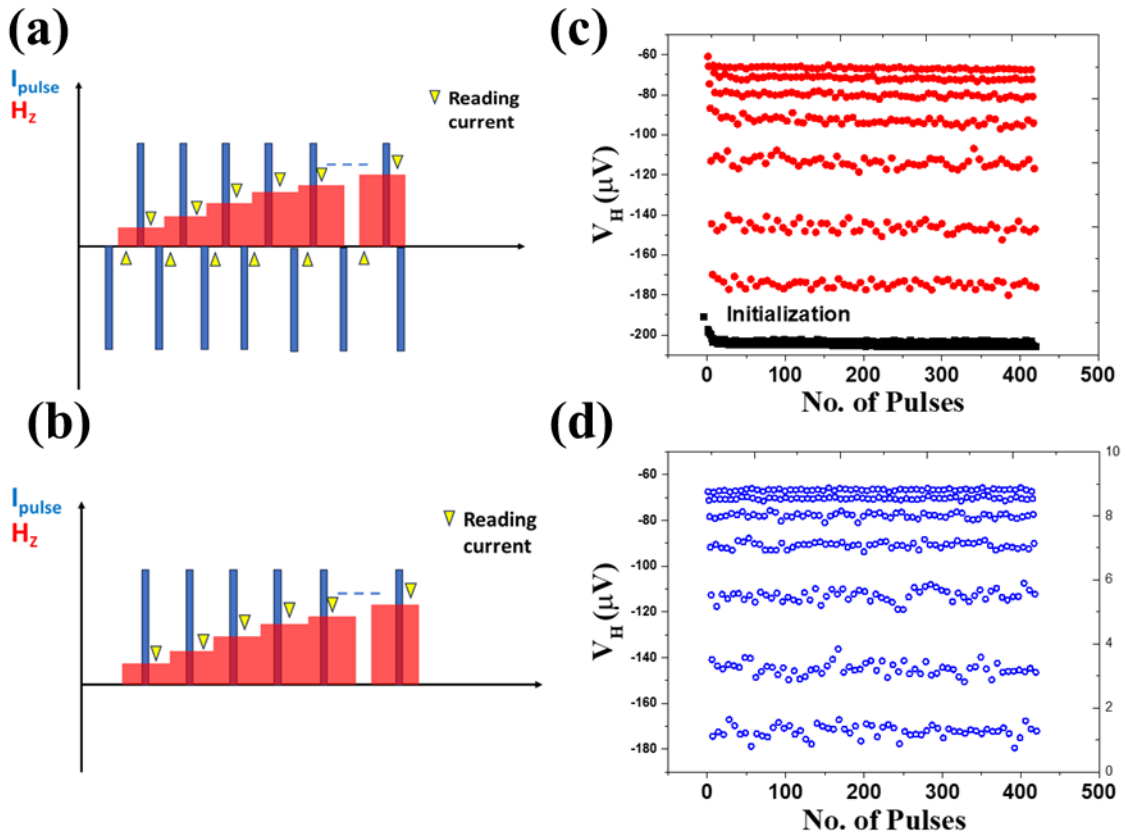


**Figure 4.7** (a) Multistate SOT switching procedure in presence of initialization step. (b) in absence of initialization step (c) multistate data (red points) after initialization step (black points) (d) multistate data even in the absence of any initialization step.

Analogue memristor nature have application in neuromorphic computing. The field of neuromorphic computing is focused with a goal of brain like functionalities in devices which could make the processing in memory function true. To replicate brain like computing in an electronic devices two main functions of brain are considered: neurons and synapses. Synapse connects neurons in brain by a connection strength called synaptic weight. To replicate this behaviour connection strengths must be non-volatile in nature and should be a multi-valued non-binary. For the realization of these functions magnetic memristor devices are prime candidates. However, in most of the multistate devices, before reaching to desired value of multi-valued synaptic weight an initial state must be attain[3,7,8,10,11]. This additional initialization step stretches the writing duration and consume additional power. We observe a solution to this issue in our proposed method. Here, a combination of  $H_z$  and current pulse are responsible for the reduction in saturation states and hence multistate behaviour. Moreover, the simulation results from Fig. 4.1 (d) suggests that the state reduction is a manifestation of SOT

and  $H_z$  and it does not require any of initialization step. Here, we compare the results for multistate with an initialization step and without it. Fig. 4.7(a) and Fig. 4.7(b) shows the writing mechanism for multistate memory with and without an initialization step. In both the cases a +60 mA pulse in presence of different  $-H_z$  field is applied as a writing sequence. Additionally, in the case where initialization step is included (Fig. 4.7(a)) a current pulse of -60 mA was applied after each writing pulse (+60 mA) to reach to an initial state. After each current pulse, AHE voltage reads the magnetic state in the device (both in Fig. 4.7(a) and (b)). In Fig. 4.3(a) the results corresponding to the - 60 mA pulse shows a fix state irrespective of various  $-H_z$  values. Therefore, the application of the initialization pulse, regardless of whether it was applied in the presence of  $H_z$  or not, has no impact on the constancy of the state corresponding to -60 mA. Here, Fig. 4.7(c) shows the multistate behaviour with an initialization step. The measurement results in Fig. 4.7(c) are obtained in presence of an applied  $-H_z$  in initialization step. However, in absence of  $-H_z$  the results do not change as the initial state is fix irrespective of  $-H_z$  value. Fig. 4.7(d) shows the results without any initialization pulse. Here, from our results it is evident that the multistate values are same with and without initialization step. Further, we have verified that the observed multistate values are at similar levels for with-initialization and initialization free process.

#### 4.6.1 Comparison of with-initialization and initialization free states

Figure 4.7 discusses the states with and without the initialization step. To compare the consistency of the multistate in both cases, Hall voltage ( $V_H$ ) is plotted against  $H_z$  field values in Figure 4.8(a). Here, we compare states corresponding to the sequence of pulses under different  $H_z$  fields for the initialization case (red circles) and the initialization-free case (black solid squares). The overlap of the data points for with and without the initialization step confirms that the states corresponding to distinct  $H_z$  values remain the same in both scenarios.

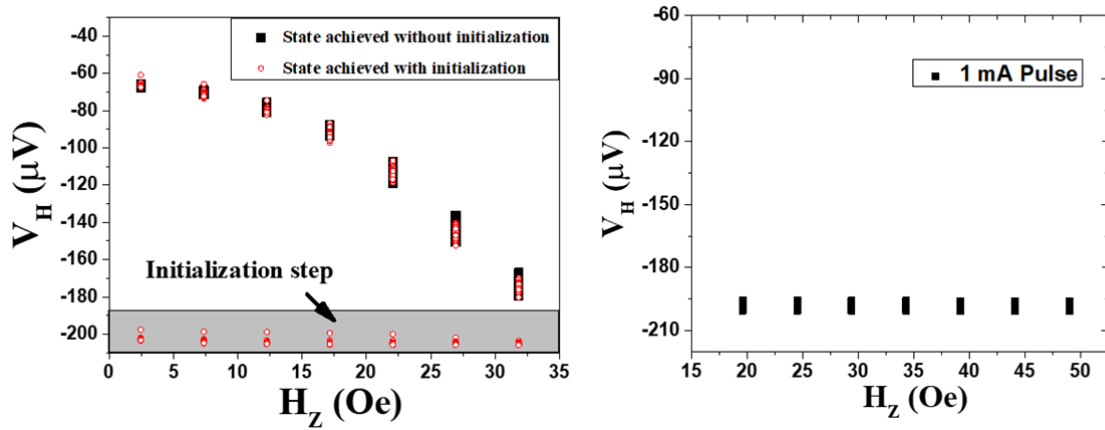


**Figure 4.8 (a)** Conventional multistate behavior with (red circle) and without (black solid square) initialization step. +60 mA SOT current pulse with different  $H_z$  field stabilizing different states. Initialization step corresponds to the -60 mA pulse **(b)** Insufficient current pulse for SOT switching (+1 mA) and varying  $H_z$  showing no change in state or  $V_H$ .

#### 4.6.2 Exploring the sole effect of $H_z$ on multistate behavior

To demonstrate that the multistate behavior is an outcome of SOT and  $H_z$  collectively or  $H_z$  alone cannot induce this effect we applied different  $H_z$  fields and small current pulses of 1mA. Note that, 1 mA pulse is insufficient to induce the SOT switching. Therefore, if the multistate behavior persists with small current pulses and different  $H_z$  fields then this would be because of  $H_z$  alone. However,  $H_z$  field alone did not show any multistate behavior and state remain idle at one state. Here,  $H_z$  values were less than the coercive field. The results are shown in Fig 4.8 (a) and Fig 4.8 (b), where the Fig 4.8 (a) is conventional multistate behavior when SOT, due to sufficient switching currents (60 mA), and  $H_z$  applied simultaneously. In comparison to Fig 4.8 (a), Fig 4.8 (b) remains in an idle initial state for various values of  $H_z$  while SOT current is only 1 mA. These results confirms that  $H_z$  field alone cannot achieve a multistate behavior and the combine effect of SOT and  $H_z$  is necessary to achieve this effect.

#### 4.6.3 Retention of states after switching off the field $H_z$

The  $H_z$  field-induced multistate/memristor behavior has its potential applications in neuromorphic computing as synaptic weight. Magnetic devices with a memristor behavior are

of great potential due to their non-volatility. To verify the stability of multi-states we read the states after switching off the magnetic field  $H_z$ . In these experiments, initially, a ‘State 1’ with  $H_z=0$  Oe is achieved (attained by  $H_z = 0$  Oe and  $I = +60$  mA). This state has highest magnitude among all multi-states as can be seen in Fig 4.3. Transition from ‘State 1’ to a different state required an application of 60 mA pulse in presence of a field  $H_z \neq 0$  Oe. Once this new state is reached, to confirm its stability,  $H_z$  field is switched off and the Hall voltage is read: (a) immediately after switching of the field (b) after a definite time. The results are shown in bar graph presented in Fig. 4.9. Here, y-axis is Hall voltage and hence y-axis differentiate multiple states and at x-axis current pulse,  $H_z$  field and time interval conditions are mentioned. For a better understanding table below also describes the condition for each bar line.

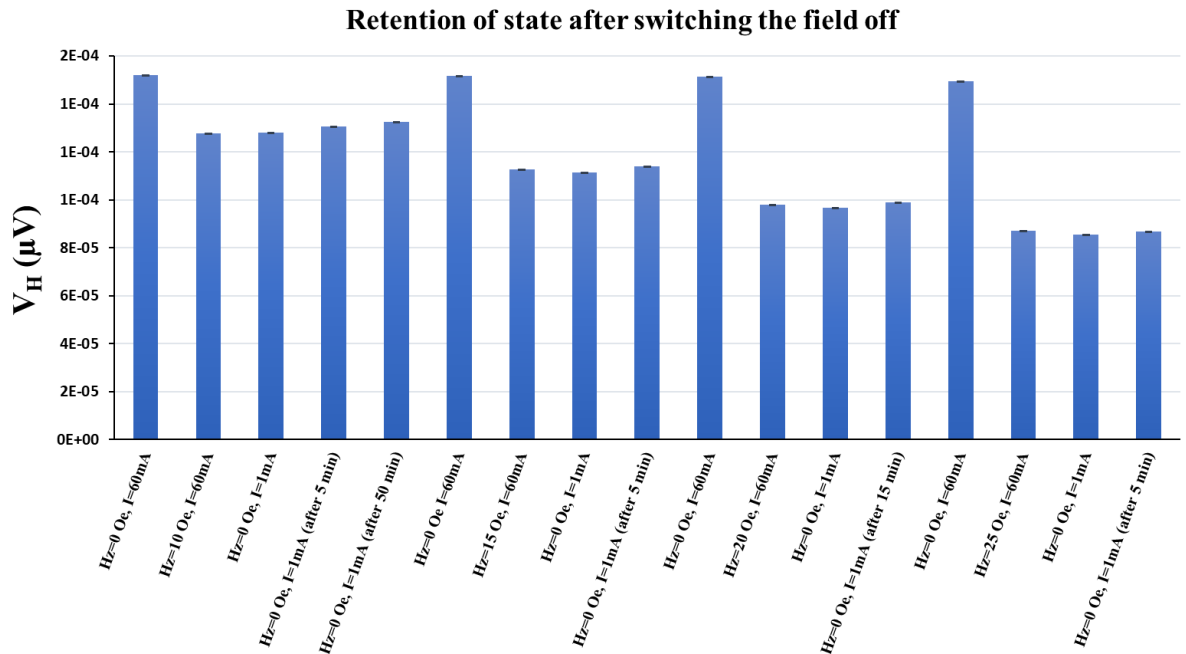


**Fig. 4.9** Retention of different states after switching off the  $H_z$  field. States are read after various time intervals.

S.No.	Write current	Read current	$H_z$ field	Time condition
1.	60 mA	1 mA	0 Oe	---
2.	60 mA	1 mA	200 mA	---

3.	-	1 mA	0 Oe	Read immediately after $H_z=0$ Oe
4.	-	1 mA	0 Oe	Read after 5 min.
5.	-	1 mA	0 Oe	Read after 50 min.
6.	60 mA	1 mA	0 Oe	-
7.	60 mA	1 mA	300 mA	-
8.	-	1 mA	0 Oe	Read immediately after $H_z=0$ Oe
9.	-	1 mA	0 Oe	Read after 5 min.
10.	60 mA	1 mA	0 Oe	-
11.	60 mA	1 mA	400 mA	-
12.	-	1 mA	0 Oe	Read immediately after $H_z=0$ Oe
13.	-	1 mA	0 Oe	Read after 15 min.
14.	60 mA	1 mA	0 Oe	-
15.	60 mA	1 mA	500 mA	-
16.	-	1 mA	0 Oe	Read immediately after $H_z=0$ Oe
17.	-	1 mA	0 Oe	Read after 5 min.

**Table 4.1** Explained x-axis of Fig. 4.9.

These results suggest that after achieving a state by the combine effect of  $H_z$  and SOT when  $H_z$  is turned off, magnetization retains this state for a long duration. Therefore, a continuous

applied field ( $H_z$ ) is not required to sustain a magnetic state making this  $H_z$  field-induced multistate behavior an energy-efficient approach

#### 4.6.4 Multistate behavior on sample other than Pt/Co/Pt

Pt/Co/Pt was one of the earliest observed PMA stacks and has been considered as a model stack for various spintronics studies. The objective of selecting Pt/Co/Pt for present study was aimed to extend the applicability of our proposed method for a wide range of PMA materials. Further, for the proof of concept that multistate results can be obtained in any PMA based stack, experiments were performed with Ta(3)/W(0.85)/Pt(3)/Co(0.6)/AlOx(1.3) stack. The thicknesses in nm for each layer are written in parentheses. W/Pt/Co/AlOx is a PMA based stack. We perform SOT-induced switching in presence of  $H_z$  field, in search of multistate behavior. After the application of  $H_z$  during SOT switching induces multistate behavior (Fig 4.10 (a)). Notably, we observed a trend in the reduction of saturation states in the W/Pt/Co/AlOx stack, resembling the trend we observed for the Pt/Co/Pt stack in main text. In Fig 4.10(b) the reduction trend is shown in presence of various  $H_z$  fields (x-axis) and SOT current pulses ( $\sim 45$  mA). Note that, after aligning the W/Pt/Co/AlOx devices with in-plane field (using the method discussed in section 4.3.1), Fig 4.10(a) and (b) obtained in presence of a symmetry breaking field  $H_x = 900$  Oe. The universal trend of saturated state reduction confirms the general applicability of proposed method.

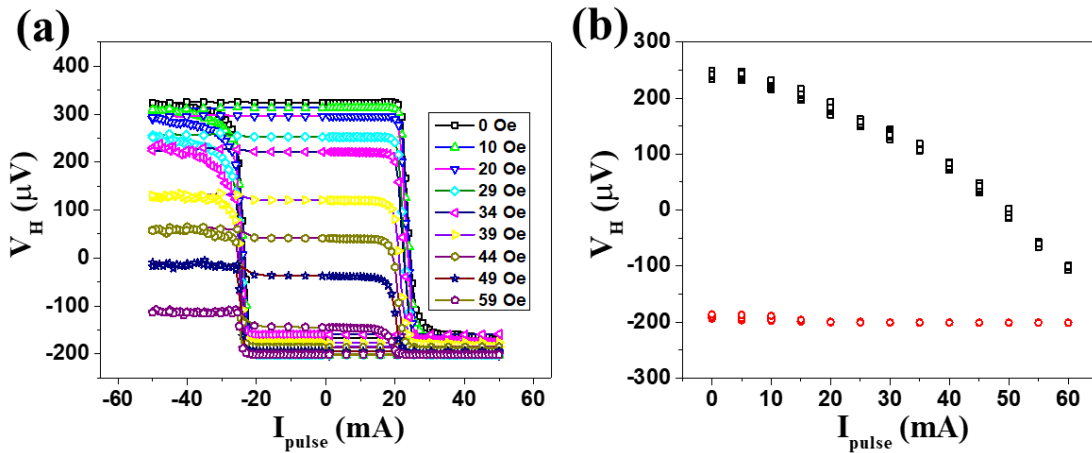


**Figure 4.10** (a) SOT switching hysteresis after the application of various  $H_z$  fields. For each  $H_z$  field value Hall voltage (y-axis) of Hall bar device is recorded after an application of 5 mS

current pulses (x-axis). **(b)** Trend of the reduction of saturation (i.e., Hall voltage at saturation, here it is read after the application of 5mS current pulse of +45 mA) as a function of  $H_z$ .

## 4.7 Conclusion

In summary, we utilized the combined symmetry of Spin-Orbit Torque (SOT) and a DC field to stabilize multiple states in our stacked device. We confirmed that integrating SOT with a static field can result in multiple intermediate saturation states, distinguished by the magnitudes and polarity of the static field. Our findings indicate that this phenomenon is induced by both SOT and the field concurrently, allowing for the manipulation of the energy barrier between states. Ultimately, our measurements address the initialization challenge in contemporary memristor devices by experimentally demonstrating initialization-free multistate memory.

## References

- [1] Y. Kim, X. Fong, K. W. Kwon, M. C. Chen, and K. Roy, Multilevel Spin-Orbit Torque MRAMs, *IEEE Transactions on Electron Devices* **62**, 561 (2015).
- [2] X. Han, X. Wang, C. Wan, G. Yu, and X. Lv, Spin-orbit torques: Materials, physics, and devices, *Applied Physics Letters* **118**, 120502 (2021).
- [3] J. Grollier, D. Querlioz, K. Y. Camsari, K. Everschor-Sitte, S. Fukami, and M. D. Stiles, Neuromorphic spintronics, *Nature Electronics* **3**, 360 (2020).
- [4] D. Marković, A. Mizrahi, D. Querlioz, and J. Grollier, Physics for neuromorphic computing, *Nature Reviews Physics* **2**, 499 (2020).
- [5] J. Torrejon *et al.*, Neuromorphic computing with nanoscale spintronic oscillators, *Nature* **547**, 428 (2017).
- [6] R. Nair, Evolution of Memory Architecture, *Proceedings of the IEEE* **103**, 1331 (2015).
- [7] H. Zhong *et al.*, Ten States of Nonvolatile Memory through Engineering Ferromagnetic Remanent Magnetization, *Advanced Functional Materials* **29**, 1806460 (2019).
- [8] Y. Cao, A. Rushforth, Y. Sheng, H. Zheng, and K. Wang, Tuning a Binary Ferromagnet into a Multistate Synapse with Spin–Orbit-Torque-Induced Plasticity, *Advanced Functional Materials* **29**, 1808104 (2019).
- [9] K.-F. Huang, D.-S. Wang, M.-H. Tsai, H.-H. Lin, and C.-H. Lai, Initialization-Free Multilevel States Driven by Spin–Orbit Torque Switching, *Advanced Materials* **29**, 1601575 (2017).
- [10] Y. Yang, H. Xie, Y. Xu, Z. Luo, and Y. Wu, Multistate Magnetization Switching Driven by Spin Current From a Ferromagnetic Layer, *Physical Review Applied* **13**, 034072 (2020).
- [11] S. Fukami, C. Zhang, S. DuttaGupta, A. Kurenkov, and H. Ohno, Magnetization switching by spin–orbit torque in an antiferromagnet–ferromagnet bilayer system, *Nature Materials* **15**, 535 (2016).
- [12] K.-S. Lee, S.-W. Lee, B.-C. Min, and K.-J. Lee, Threshold current for switching of a perpendicular magnetic layer induced by spin Hall effect, *Applied Physics Letters* **102**, 112410 (2013).
- [13] C. Zhang, S. Fukami, H. Sato, F. Matsukura, and H. Ohno, Spin-orbit torque induced magnetization switching in nano-scale Ta/CoFeB/MgO, *Applied Physics Letters* **107**, 012401 (2015).



- [14] R. Posti, A. Kumar, D. Tiwari, and D. Roy, Emergence of considerable thermoelectric effect due to the addition of an underlayer in Pt/Co/Pt stack and its application in detecting field free magnetization switching, *Applied Physics Letters* **121**, 223502 (2022).
- [15] M. Bauer, J. Fassbender, B. Hillebrands, and R. L. Stamps, Switching behavior of a Stoner particle beyond the relaxation time limit, *Physical Review B* **61**, 3410 (2000).
- [16] F. Schumacher, On the modification of the Kondorsky function, *Journal of Applied Physics* **70**, 3184 (1991).
- [17] O. J. Lee, L. Q. Liu, C. F. Pai, Y. Li, H. W. Tseng, P. G. Gowtham, J. P. Park, D. C. Ralph, and R. A. Buhrman, Central role of domain wall depinning for perpendicular magnetization switching driven by spin torque from the spin Hall effect, *Physical Review B* **89**, 024418 (2014).
- [18] S. Kim, P.-H. Jang, D.-H. Kim, M. Ishibashi, T. Taniguchi, T. Moriyama, K.-J. Kim, K.-J. Lee, and T. Ono, Magnetic droplet nucleation with a homochiral Néel domain wall, *Physical Review B* **95**, 220402 (2017).
- [19] C.-F. Pai, M. Mann, A. J. Tan, and G. S. D. Beach, Determination of spin torque efficiencies in heterostructures with perpendicular magnetic anisotropy, *Physical Review B* **93**, 144409 (2016).
- [20] L. Liu, O. J. Lee, T. J. Gudmundsen, D. C. Ralph, and R. A. Buhrman, Current-Induced Switching of Perpendicularly Magnetized Magnetic Layers Using Spin Torque from the Spin Hall Effect, *Physical Review Letters* **109**, 096602 (2012).
- [21] T. Dohi, S. Fukami, and H. Ohno, Influence of domain wall anisotropy on the current-induced hysteresis loop shift for quantification of the Dzyaloshinskii-Moriya interaction, *Physical Review B* **103**, 214450 (2021).
- [22] A. Thiaville, S. Rohart, É. Jué, V. Cros, and A. Fert, Dynamics of Dzyaloshinskii domain walls in ultrathin magnetic films, *Europhysics Letters* **100**, 57002 (2012).
- [23] R. Posti, A. Kumar, M. Baghoria, B. Prakash, D. Tiwari, and D. Roy, Odd symmetry planar Hall effect: A method of detecting current-induced in-plane magnetization switching, *Applied Physics Letters* **122**, 152405 (2023).
- [24] Y.-T. Liu, T.-Y. Chen, T.-H. Lo, T.-Y. Tsai, S.-Y. Yang, Y.-J. Chang, J.-H. Wei, and C.-F. Pai, Determination of Spin-Orbit-Torque Efficiencies in Heterostructures with In-Plane Magnetic Anisotropy, *Physical Review Applied* **13**, 044032 (2020).

- [25] S. Emori and G. S. D. Beach, Roles of the magnetic field and electric current in thermally activated domain wall motion in a submicrometer magnetic strip with perpendicular magnetic anisotropy, *Journal of Physics: Condensed Matter* **24**, 024214 (2012).
- [26] K.-J. Kim, J. Ryu, G.-H. Gim, J.-C. Lee, K.-H. Shin, H.-W. Lee, and S.-B. Choe, Electric Current Effect on the Energy Barrier of Magnetic Domain Wall Depinning: Origin of the Quadratic Contribution, *Physical Review Letters* **107**, 217205 (2011).



## Chapter 5

# Detection of in-plane magnetization switching using odd symmetry planar Hall effect

### 5.1 Introduction

Search for efficient means to process and store information coupled with negligible dissipation has been a perpetual effort in modern-day electronics. One such goal is to develop magnetoresistive random-access memory (MRAM) operating at high frequency with low energy consumption[1-3]. It was proposed that spin-transfer torque (STT) based MRAM could be an alternative to the presently used field-driven MRAM[4-6]. However, low endurance due to the flow of high current density through the tunnel barrier during the writing operation limits the applicability of STT-MRAM devices[4,7]. In this regard, spin-orbit-torque (SOT) MRAM draws immense attention due to better endurance, faster access time, and lower energy consumption than STT-MRAM[4,7]. In SOT-MRAM, the lateral current through the heavy metal (HM) layer generates spin current due to the bulk spin-Hall effect or/and interfacial Rashba-Edelstein effect, which induces a torque in the adjacent ferromagnetic (FM) layer leading to the magnetization reversal in the FM layer in HM/FM heterostructures[8-10]. Generally, two orthogonal components, namely, antidamping-like (AD) and field-like (FL) SOT, are realized in the HM/FM heterostructures[11,12].

Depending on the relative orientation of the magnetic easy axis (EA) and spin polarization ( $\sigma$ ) direction, one can envisage three different SOT switching schemes such as type-X (in-plane EA  $\perp$   $\sigma$ ), type-Y (in-plane EA  $\parallel$   $\sigma$ ) and type-Z (out-of-plane EA  $\perp$   $\sigma$ )[13-17]. It has been shown that for achieving fast switching in type-Y (type-X & type-Z) material, current pulse with a higher (lower) magnitude is required, thus restricting the device's applicability based on type-Y geometry[16,17]. Notably, type-X and type-Z devices show similar magnetization dynamics since, in both cases, EA  $\perp$   $\sigma$ . Perpendicular magnetic anisotropy [PMA] (in-plane magnetic) based material stacks show type-Z (type- X) switching. Notably, an external magnetic field or equivalent is required to break the symmetry to achieve

deterministic switching in both type-Z & type- X devices [13,14,16]. Moreover, deterministic switching in type –X device can be achieved by introducing a slight tilt angle between the current channel and the magnetic easy axis of the in-plane FM layer[16,17]. However, the thin-film deposition and post-processing to achieve an optimized growth of PMA-based heterostructures require rigorous calibration compared to in-plane magnetized stacks. Thus, type-X devices are ideal candidates for durable, faster, and energy-efficient data storage devices and magnetic sensors that can be deposited under easy growth conditions.

Regardless of these benefits, type-X switching is only detectable with limited methods. Presently, two methodologies, namely differential planar Hall Effect technique (we refer this method as 'old PHE')[14,15] and AC 2<sup>nd</sup> Harmonic technique (we would coin it as 'AC technique')[13] are utilized for detecting type-X switching. In "old PHE", planar Hall signals differing at alternating field values (along DC current direction) define in-plane magnetization direction. For the AC technique, the application of DC is replaced by the sinusoidal AC, and the magnetization state is determined by measuring the 2<sup>nd</sup> harmonic response of the planar Hall voltage. Both these methods have certain limitations such in 'old PHE', an external alternating magnetic field is required, whereas in 'AC technique', the second harmonic signals are significantly weak, rendering it to be challenging to detect for low-resistance devices. Thus, universally applicable and straightforward detection of type-X magnetization reversal is still lacking, unlike type-Z switching, which employs the measurement of the DC-based anomalous Hall effect (AHE) in presence of an external DC magnetic field[18,19]. In this regard, we propose a more straightforward methodology of detecting type-X switching by measuring a modified PHE signal based on DC measurements in presence of an external DC magnetic field. We have shown our proposed measurement scheme for the in-plane magnetized Pt/Co/NiFe/Pt stack. In this stack, the lateral current passing through it can switch the in-plane magnetization of the stack. We have demonstrated better sensitivity for our proposed scheme than the AC technique. Further, we characterized the SOT-induced effective fields generated by AD-SOT and FL-SOT in our investigated device. Notably, we have engineered this stack by introducing a very thin layer of Co to induce considerable FL-SOT, which would otherwise be absent in stacks where FM has similar HM interfaces[20,21].

## 5.2 Theoretical Background

AHE ( $V_{AHE} \propto m_z$ ) and PHE ( $V_{PHE} \propto m_x \cdot m_y$ ) signals are the measures of out-of-plane and in-plane magnetization components, respectively. Note that the magnetization switching of the perpendicularly magnetized stack is easy to detect via AHE ( $V_{AHE} \propto m_z$ ) signal. In contrast, the even symmetry of magnetization in PHE ( $V_{PHE} \propto m_x \cdot m_y$ ) makes it difficult to perceive for the in-plane magnetized sample. In this regard, our effort is directed to modify the existing PHE measurement protocol based on the DC and external DC magnetic field so that the resultant quantity based on PHE becomes proportional to the in-plane magnetization.

Generally, for an in-plane magnetized film, the Hall signal has both anomalous and planar Hall contributions, which can be expressed as

$$V_H = V_{AHE} + V_{PHE} = I\Delta R_{AHE}m_z + I\Delta R_{PHE}m_xm_y \quad (5.1)$$

Here,  $\Delta R_{AHE}$  and  $\Delta R_{PHE}$  are AHE and PHE resistances, respectively, and  $I$  here is the applied current.

A field sweep along current direction ( $H_x$ ) shows an insignificant contribution from the  $m_z$  component for an in-plane magnetized sample. Thus, the AHE contribution became redundant in Eq. 5.1. Thus, Eq. (5.1) can further be modified as

$$V_H \approx V_{PHE} = I\Delta R_{PHE} \cos\varphi \sin\varphi \quad (5.2)$$

Here,  $\varphi$  is the azimuthal magnetization angle (illustrated in Fig. 5.1a). The angle  $\varphi$  depends on the resultant magnetic field which generally combines both the external and current-induced field. When a lateral current is passed through the sample (along  $\hat{x}$ ), current-induced AD-SOT and FL-SOT with effective fields of  $H_{AD} (\propto \sigma \times m)$  and  $H_{FL} (\propto \sigma)$ , respectively (here,  $\sigma$  is along  $\hat{y}$  and  $m$  is along  $\hat{x}$ ) is generated. Here,  $H_{AD}$  is along  $\hat{z}$  and contributes to the AHE, whereas  $H_{FL}$  lies along  $\hat{y}$  and modifies the PHE. Nonetheless, current also generates an Oersted field ( $H_{Oe}$ ) along  $\hat{y}$ , which contributes to the PHE (illustrated in Fig. 5.1a) as well[22-24]. Thus, the resultant current-induced field takes the following form:  $H_I = H_{FL} + H_{Oe}$ .

The Taylor series expansion of  $\varphi(H_{ext}, H_I)$  about  $I = 0$  gives rise to:

$$\varphi(H_{ext}, H_I) = \varphi(H_{ext}, H_I)|_{I=0} + \frac{d\varphi(H_{ext}, H_I)}{dI}(I) + o(I^2)$$

$$\begin{aligned}\varphi(H_{ext}, H_I) &\approx \varphi(H_{ext}, H_I = 0) + \frac{\partial \varphi}{\partial H_I} \frac{\partial H_I}{\partial I}(I) = \varphi_0 + \Delta \varphi \\ \Delta \varphi &= \frac{\partial \varphi}{\partial H_I} \frac{\partial H_I}{\partial I} I \quad \& \quad \varphi_0 = \varphi(H_{ext}, h_I = 0)\end{aligned}\quad (5.3)$$

Here,  $\varphi_0$  is the direction of magnetization before applying the current.

After applying an in-plane current, Eq. (5.2) can be modified as:

$$V_H \approx V_{PHE} = I \Delta R_{PHE} \cos(\varphi_0 + \Delta \varphi) \sin(\varphi_0 + \Delta \varphi)$$

We have further assumed that the external field required to saturate the magnetization along the in-plane direction is greater than the current-induced field ( $\Delta \varphi \ll \varphi_0$ ). This assumption holds for all the reading currents used in our magnetization detection scheme. Further, the assumption  $\Delta \varphi \ll \varphi_0$  implies that  $\sin(\Delta \varphi) \approx \Delta \varphi$ , and  $\cos(\Delta \varphi) \approx 1$ . Hence:

$$V_H = I \Delta R_{PHE} \left[ \frac{\sin 2\varphi_0}{2} + \Delta \varphi \cos 2\varphi_0 - \frac{\sin 2\varphi_0}{2} (\Delta \varphi)^2 \right] \quad (5.4)$$

Notably, depending on the polarity of the applied DC for the measurement of PHE, the angle  $\varphi$  takes the form of  $\varphi = \varphi_0 + \Delta \varphi$  for  $(+I)$  and  $\varphi = \varphi_0 - \Delta \varphi$  for  $(-I)$ , respectively. For our magnetization switching detection scheme, we would measure  $\Delta V_H = V_H(+I) + V_H(-I)$  which takes the following form by applying Eq. (5.3) and (5.4):

$$\Delta V_H = V_H(+I) + V_H(-I) = 2I^2 \Delta R_{PHE} \cos 2\varphi_0 \frac{\partial \varphi}{\partial H_I} \frac{\partial H_I}{\partial I} \quad (5.5)$$

Further, one can approximate  $H_I \propto I \Rightarrow \frac{\partial H_I}{\partial I} = k(\text{constant})$  to Eq. (5.5). Moreover, we can estimate  $\varphi = \frac{H_I}{H_{ext}}$  for  $H_{ext} \parallel \hat{x}$ . (With  $H_{ext}, I \parallel \hat{x}$ , one can expect  $H_{FL} + H_{oe}$  is along  $\hat{y}$  and  $\tan \varphi \approx \varphi = \frac{H_I}{H_{ext}}$ )

With the conditions mentioned earlier, Eq. (5.5) can be reduced to

$$\Delta V_H \propto \frac{1}{H_{ex}} \quad (5.6)$$

Similarly,

$$V_H(+I) - V_H(-I) \propto \frac{1}{H_{ex}^2} \quad (5.7)$$

Eq. (5.6) and (5.7) qualitatively describe that the  $\Delta V_H$  have asymmetric nature about the external field, which in turn induces the change in magnetization for the device with in-plane magnetic anisotropy. Afterward,  $\Delta V_H$  is coined as odd planar Hall voltage (O-PHV). In contrast,  $V_H(+I) - V_H(-I)$  is symmetric. Thus, the estimation of the O-PHV in a sample that exhibits type-X switching would lead to the quantification of the magnetization switching similar to the measurement of AHE for the PMA sample.

### 5.3 Experimental Details

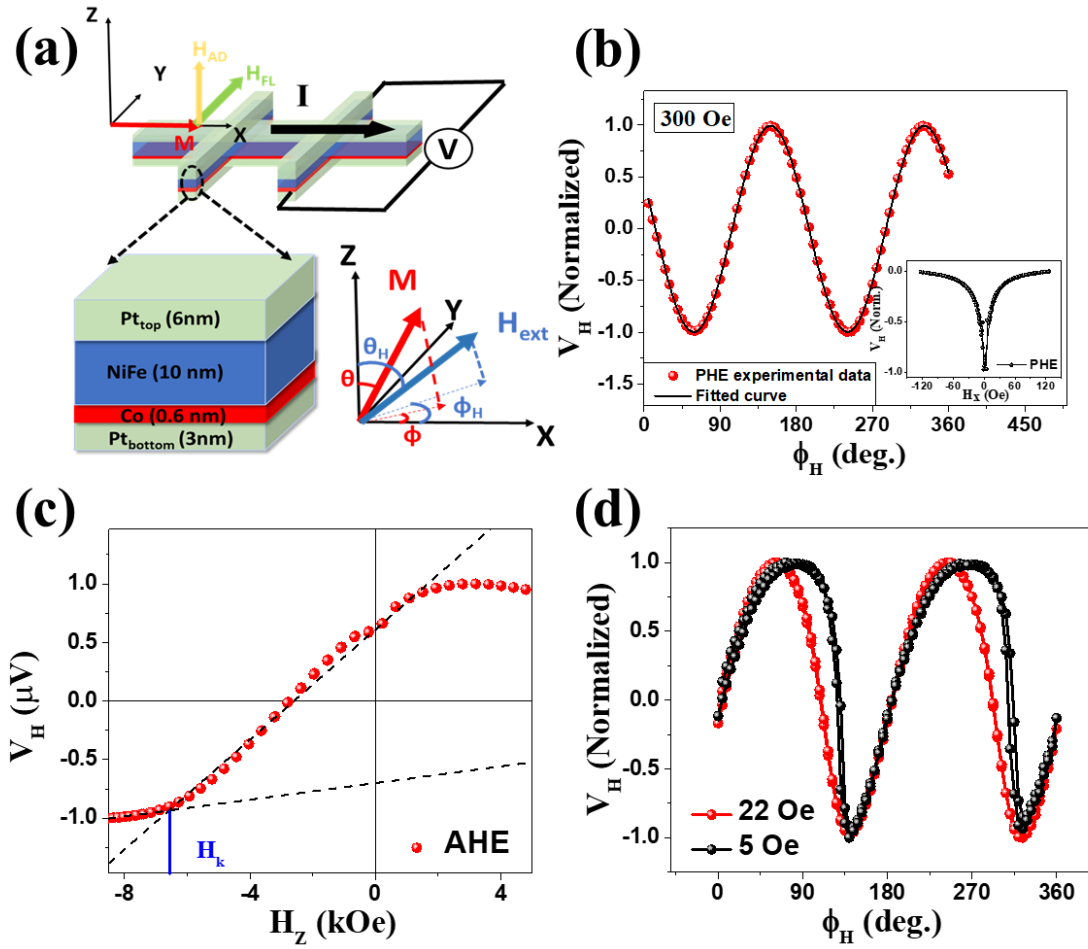


Figure 5.1 (a) Pt/Co/NiFe/Pt stack with the experimental geometries and SOT directions. (b) Planar Hall voltage ( $V_H$ ) vs.  $\phi_H$  in presence of 300 Oe (inset:  $V_H$  vs.  $H_x$ ). (c)  $V_H$  vs.  $H_z$ . (d)  $V_H$  vs.  $\phi_H$  from  $0^\circ$  to  $360^\circ$  (trace and retrace) in the presence of 5 Oe (black) and 22 Oe fields (red).



To demonstrate the applicability of the O-PHV as a method of detecting the in-plane magnetization switching for the type-X device, a thin film stack of Ta(3)/Pt(3)/Co(0.6)/NiFe(10)/Pt(6) (from hereon we would refer it as NiFe stack) films were deposited onto thermally oxidized Si/SiO<sub>2</sub> substrate by dc-magnetron sputtering. The thickness of the films indicated in the parenthesis is nanometers. The deposition was carried out at room temperature with a base vacuum better than  $1 \times 10^{-7}$  Torr and an Ar gas pressure of 3 mTorr. A thin Co layer is added to enhance the FL torque, as discussed later. Subsequently, thin films were patterned into six terminal Hall bar devices with lateral dimensions of  $135 \times 12 \mu\text{m}^2$  using photo-lithography and plasma etching. A device illustration with measurement geometry is depicted in Fig 5.1a. The current was applied through the current channel along  $\hat{x}$ , and voltage/resistance was probed along transverse Hall channels. Transport measurements were carried out at room temperature. All DC measurements were carried out using a Keithley 2450 source meter and Keithley 2182A nanovoltmeter. AC harmonic measurements were conducted using a lock-in amplifier (EG&G 7265) at a reference frequency of 577.13 Hz.

## 5.4 Results and Discussion

### 5.4.1 Magnetic properties of heterostructure

In-plane magnetic anisotropy present in our stack was confirmed through PHE and AHE experiments (Fig. 5.1b and Fig 5.1c). Figure 5.1(b) depicts planar Hall voltage ( $V_H$ )  $\propto \sin 2\phi_H$  dependency for the investigated stack when the sample is rotated in-plane in presence of 300 Oe magnetic field rendering dominating in-plane magnetization component ( $V_H \propto m_x \cdot m_y \propto \sin 2\phi_H$ ) in our sample. In-plane anisotropy of the sample is further confirmed through the measurement of the variation of  $V_H$  as a function of the in-plane field swept along x-direction ( $H_x$ ) (inset of Fig. 5.1b). The out-of-plane variation of the ( $V_H^{\text{out}}$ ) with the varying magnetic field along z-direction is shown in Figure 5.1(c) which illustrate that the hard axis with anisotropy field  $\sim 6590$  Oe lies perpendicular to the sample plane. To confirm the in-plane easy direction of magnetization in our stack lies along  $\hat{x}$ , we have performed the following experiments after saturating the sample magnetization along  $\hat{x}$  (by applying 1 kOe external field). The variation of the planar Hall voltage of the NiFe stack was measured by rotating the

sample in-plane in presence of two constant DC magnetic fields, 5 Oe & 22 Oe, as shown in Figure 5.1(d). The angular variation of PHE at  $\sim 22$  Oe depicts a usual  $\sin 2\phi_H$  dependency, whereas, at 5 Oe, it exhibits a sharp transition at  $\phi_H = 90^\circ$  (when  $m$  is along  $\hat{y}$ ). This confirms the presence of an in-plane magnetic hard axis along  $\hat{y}$ . Notably, the presence of in-plane easy direction along  $\hat{x}$  would further be corroborated in the following section.

#### 5.4.2 Odd symmetry planar Hall signal

Fig. 5.2a shows  $V_H$  for the NiFe stack as a function of  $H_x$  by applying  $\pm 5$  mA DC. Further, O-PHV and  $V_H(+5 \text{ mA}) - V_H(-5 \text{ mA})$  is estimated from the Figure 5.2(a), which shows asymmetric and symmetric nature respectively with the field sweep along  $H_x$  (Fig. 5.2b). This validates the qualitative analysis carried out in the preceding section. Furthermore, the hysteric nature of O-PHV in Fig. 5.2b separates  $+m_x$  and  $-m_x$  states. To simplify this method, instead of adding the complete PHE curves for  $+I$  and  $-I$  (as in Fig 5.2c), we measured  $V_H(+I) + V_H(-I)$  at each value of the magnetic field sweep step (Fig. 5.2d). We observed a hysteric nature separating two saturation states of  $m_x$  making it a useful detection scheme for an in-plane magnetized sample.

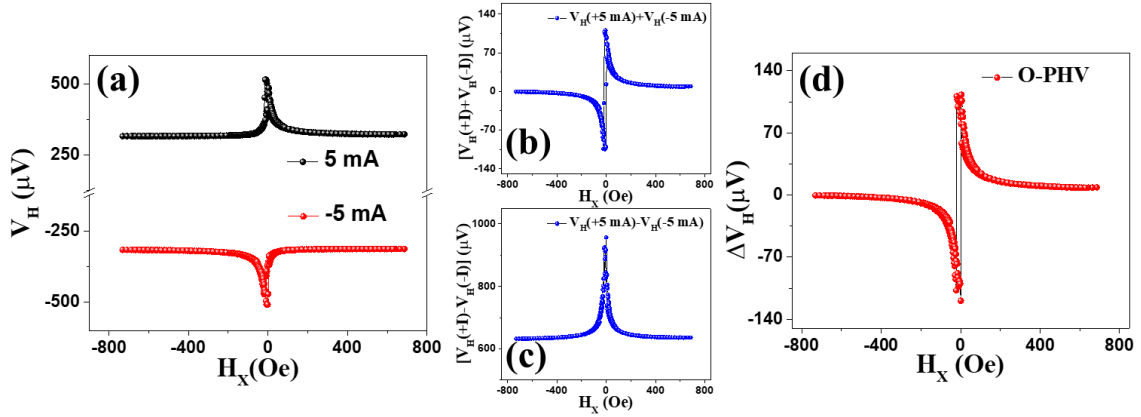


Figure 5.2 (a) PHE voltage vs.  $H_x$  at  $\pm 5$  mA currents. (b)  $V_H(+5 \text{ mA}) - V_H(-5 \text{ mA})$ , and (c)  $V_H(+5 \text{ mA}) + V_H(-5 \text{ mA})$  vs.  $H_x$ . (d) O-PHV ( $\Delta V_H$ ) measured at magnetic field sweep step.

#### 5.4.3 SOT characterization in NiFe-stack

Based on our calculation and subsequent measurement of O-PHV, one would assume the presence of considerable  $H_{FL}$  in the NiFe stack. In order to quantitatively evaluate the

contribution of  $H_{AD}$  and  $H_{FL}$ , we have measured the 2<sup>nd</sup> harmonic contribution of the Hall voltage while sweeping the applied magnetic field along  $\hat{x}$  (Figure 5.3). The experimentally obtained variation of  $R_{xy}^{2\omega}$  vs.  $H_x$  was subsequently fitted using the following equation[12,13,22,25].

$$R_{xy}^{2\omega} = \left[ \left( -R_{AHE} \frac{H_{AD}}{H_{ext} - H_k} + R_{VT} \right) \cos\varphi + 2R_{PHE} (2\cos^3\varphi - \cos\varphi) \frac{H_{FL} + H_{Oe}}{H_{ext}} \right] \quad (5.8)$$

Here, anomalous and planar Hall resistances are  $R_{AHE} = 109 \text{ m}\Omega$  and  $R_{PHE} = 19 \text{ m}\Omega$ , respectively. The  $R_{VT}$  is a signal generated by the anomalous Nernst effect (ANE). ANE is induced by a temperature gradient  $\nabla T$ , produced by Joule heating. We have repeated this measurement for different magnitude of the AC through the NiFe stack, and the obtained values of  $H_{AD}$  and  $H_I (= H_{FL} + H_{Oe})$  are plotted for different current amplitudes (Fig. 5.3a).

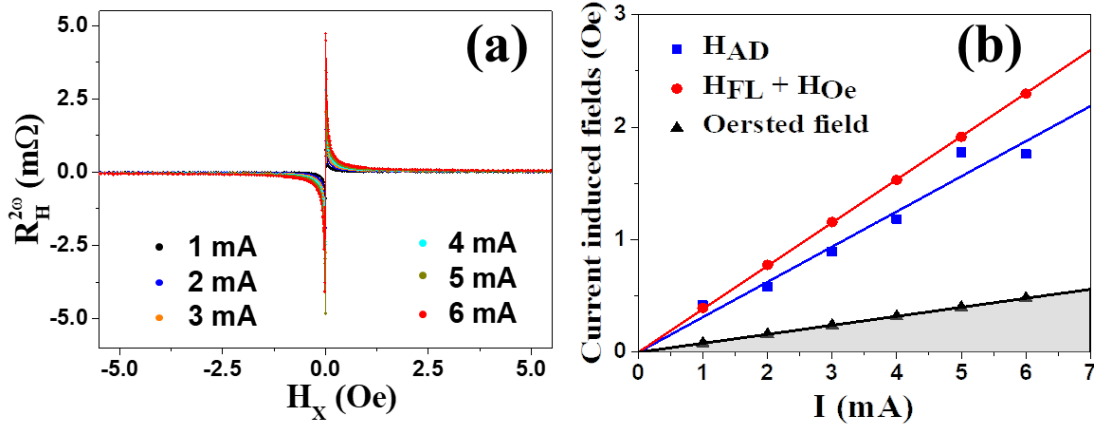


Figure 5.3 (a)  $R_{xy}^{2\omega}$  vs.  $H_x$  for different applied AC (solid circles) current and the fitted curve (corresponding lines) using Eq. 5.8. (b)  $H_{AD}$ ,  $H_I$ , and  $H_{Oe}$  contributions as a function of applied AC.

The rate of change of  $H_{AD}$  and  $H_I$  with the applied AC is found to be 0.31 Oe/mA and 0.38 Oe/mA, respectively. The ANE signal, as compared to the coefficients of effective field terms, is insignificant[13] in our case ( $R_{VT} \sim 5.9 \text{ }\mu\Omega/\text{mA}$ ). Further, the Oersted field contribution ( $H_{Oe}$ ) is disentangled from  $H_I$  in Fig. 5.3b. The  $H_{Oe}$  field originates due to the lateral current flowing through both Pt layers, calculated using[23]  $f_{HM} \frac{\mu_0 I}{2w}$ . (Here,  $f_{HM}$  is the fraction of current ( $I$ ) flowing through the HM layers,  $\mu_0$  is vacuum permeability, and  $w$  is Hall bar width.). It is found that at a given current value,  $H_I$  contribution exceeds  $H_{AD}$ . Generally, the  $H_{AD}$  field is

generated through bulk HM whereas the  $H_{FL}$  originated due to the inversion symmetry breaking at the interface. It is noteworthy that to achieve considerable  $H_{FL}$  in the NiFe stack, which is otherwise absent in an FM layer with symmetric interface[20], we have engineered the NiFe stack by introducing a thin Co layer between Pt and NiFe interface. This leads to the dissimilar interfaces about the NiFe layer resulting in a higher value of  $H_{FL}$  (hence,  $H_I$ ).

#### 5.4.4. Comparison of reading mechanisms

Next, we evaluated the NiFe stack's switching behavior in presence of an externally applied field using the 'AC technique' (Fig.5.4 (a))[13]. In this technique, an alternating current is applied during external magnetic field sweep after each field step, and second harmonic Hall signal ( $V_H^{2\omega}$ ) is detected. The  $V_H^{2\omega}$  as a function the in-plane field differentiates the two polarities of in-plane magnetization reversal (Fig. 5.4 (a)). It is found that the O-PHV based reading mechanism (Fig. 5.4 (b)) shows an enhanced signal as compared to the AC technique at same current value. Quantitatively, the ratio of DC Hall signal amplitude to the second harmonic Hall signal amplitude shows  $[\frac{(\Delta V_H)_{amp}}{(V_{2\omega})_{amp}} = \frac{4.8 \mu V}{0.8 \mu V}] \sim 6$  times enhanced O-PHV signal at 1 mA read current. Therefore, the  $m_x$  states in our proposed reading mechanism are easier to detect than the AC technique. We have estimated the coercivity of the stack using both methods (inset of Fig 5.4), and it is found to be  $\sim 12$  Oe consistent for both methods. This further validates our proposed magnetization switching detection scheme using O-PHV.

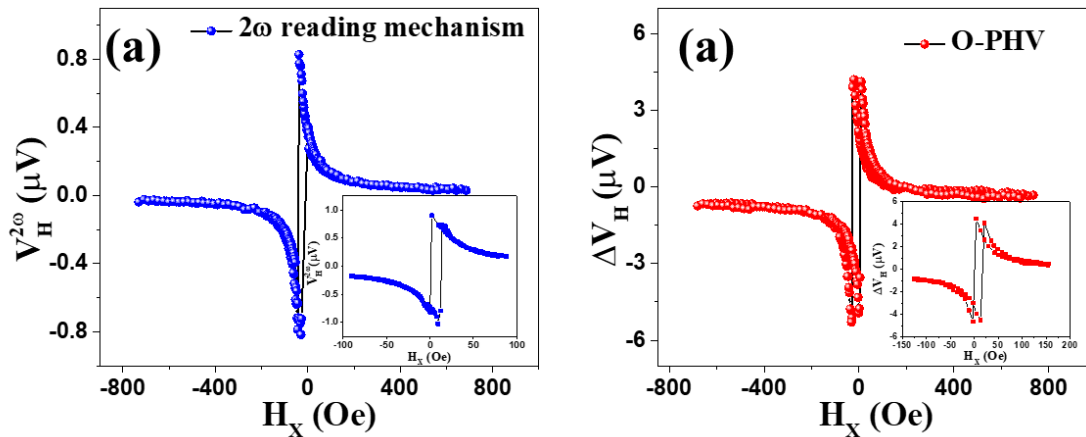


Fig. 5.4 (a)  $V_H^{2\omega}$  vs.  $H_x$ . (b) O-PHV vs.  $H_x$  (at 1 mA applied currents).

### 5.4.5. Magnetization switching detection

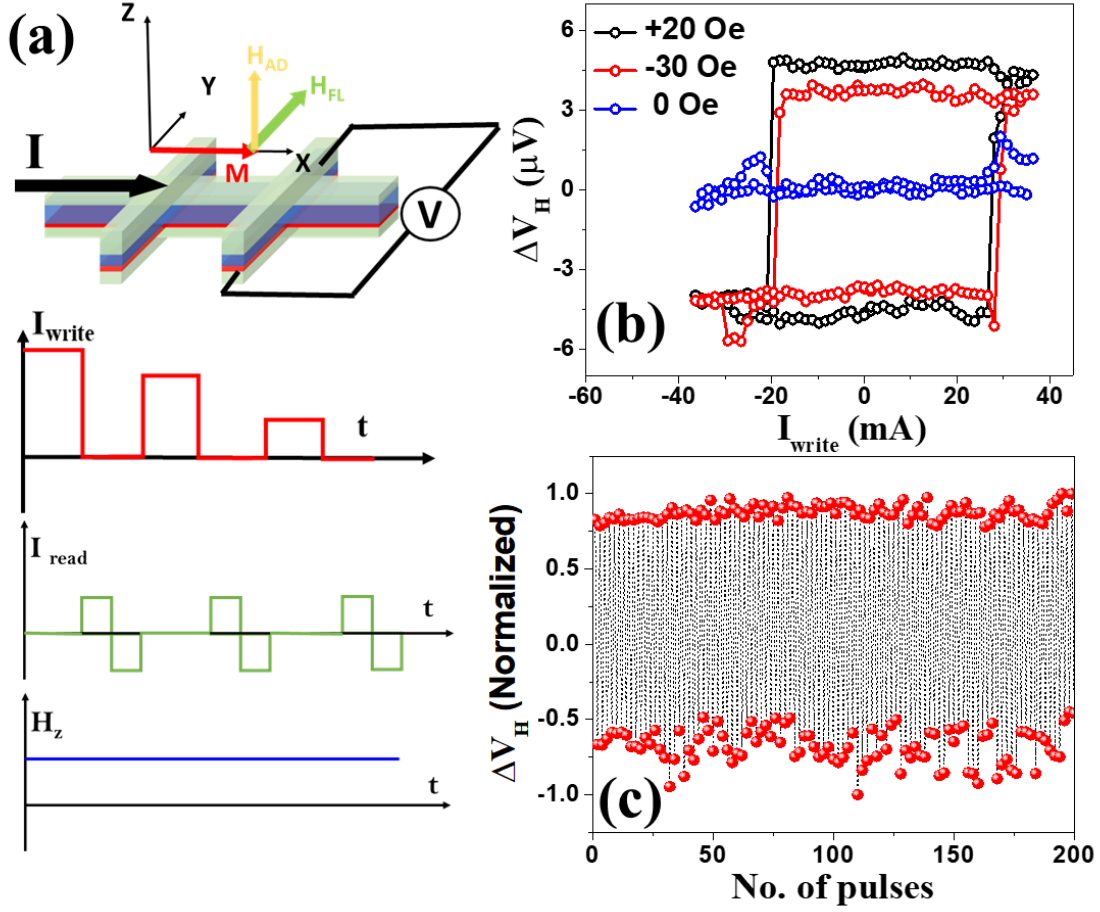


Figure 5.5 (a) Measurement scheme for the O-PHV method. (b) O-PHV (read by  $\pm 1$  mA) as function of DC pulses ( $I_{write}$ ) in the presence of different  $H_z$  fields (-30, 0, and, +20 Oe). (c) O-PHV (read currents  $\pm 1$  mA) after consecutive  $\pm 35$  mA pulses in presence of 20 Oe  $H_z$ .

Further, we have employed the O-PHV to detect the current-induced magnetization switching in the NiFe stack. We have applied 1 ms writing current pulses along  $\hat{x}$  for the current-induced switching, and the magnetization orientation is subsequently detected by our proposed method (scheme illustrated in Fig 5.5 (a)). Here the magnetization state was detected using  $\pm 1$  mA probe current. We have averaged 20 readings to obtain the final data corresponding to a particular writing current pulse for a better signal-to-noise ratio. In presence of a symmetry-breaking field  $H_z$ , we observed a hysteric behavior (Fig. 5.5 (b)), which corresponds to current-assisted magnetization switching. We observed similar hysteresis behavior for the negative and

positive polarity of  $H_z$ , corroborating similar results in the literature[13]. Our stack's in-plane switching current was found to be  $\sim 24$  mA. Without the application of  $H_z$ , we did not observe the current-induced magnetization switching (Fig. 5.5 (b)). It is found that a minimum of 7 Oe symmetry breaking field is required for current-induced switching in our stack. It is found in previous reports that a small tilt of magnetization from the current channel (in XY-plane) can induce a field-free switching[13,16,17]. However, the absence of switching behavior without applying any symmetry-breaking field suggests no tilt of magnetization from the x-direction. Therefore, as discussed earlier, our devices are truly type-X supporting measurements of angular variation of PHE in Fig. 5.1d. To check the reproducibility of the current-induced switching using our method, we measured the O-PHV voltage for 200 current cycles of +35 mA and -35 mA pulses. After applying a current pulse (+35 mA), the O-PHV signal was measured in presence of  $H_z = +20$  Oe using  $\pm 1$  mA probe current. The exact process was repeated for the -35 mA current pulse. The occurrence of bipolar states up to 200 current pulse cycles verify the high reproducibility of our proposed method.

#### 5.4.6 Magnetization reversal energy barrier

Additionally, we calculated the energy barrier (or thermal stability) between two magnetization saturation states. For high retentivity of a memory device, the industry standard for thermal stability lies  $\sim 40$ -60  $k_B T$ [26]. We performed current pulse-dependent magnetization switching experiments to calculate the barrier energy between magnetization states in NiFe stack.

For current induced magnetization switching the nucleation of reverse domain is essential. The reversed domain nucleate and propagate in the sample and eventually switch the magnetization orientation. This nucleation can occur due to current induced Oersted field, current induced SOTs, or both. To calculate the magnetization reversal energy barrier from our experimental data we performed current induced magnetization switching experiment at various current pulse widths (4, 10, 20, 30, 50, 100 and, 200 mS). The extracted switching current values are fitted with (Fig. 5.6):

$$I_c = I_{c0} \left[ 1 - \frac{kT}{E_b} \ln \left( \frac{\tau_p}{\tau_0} \right) \right] \quad (5.9)$$

Here,  $I_C$  is the experimentally measured critical switching current value at current pulse width  $\tau_p$ , while  $I_{C_0}$  is intrinsic critical current value (at  $T=0$  K),  $\tau_0$  is the inverse of characteristic attempt frequency and is considered 1 nS[27], and  $E_b$  is the energy barrier between two magnetization states. The average energy barrier value for our experiments is  $\sim 54$  k<sub>B</sub>T. The barrier energy extracted from our experiments is of the order of industrial standard to meet the retention time of  $\sim 10$  year ( $E_b \sim 40$ -60 k<sub>B</sub>T)[26]. At the same time our obtained  $E_b$  value matches well with the  $E_b$  value obtained from other SOT switching experiments[28,29].

Therefore, the calculated barrier energy ( $E_b$ ) was found to be  $\sim 54$  k<sub>B</sub>T which matches well with other SOT switching experiments as well as the industrial standard[28,29].

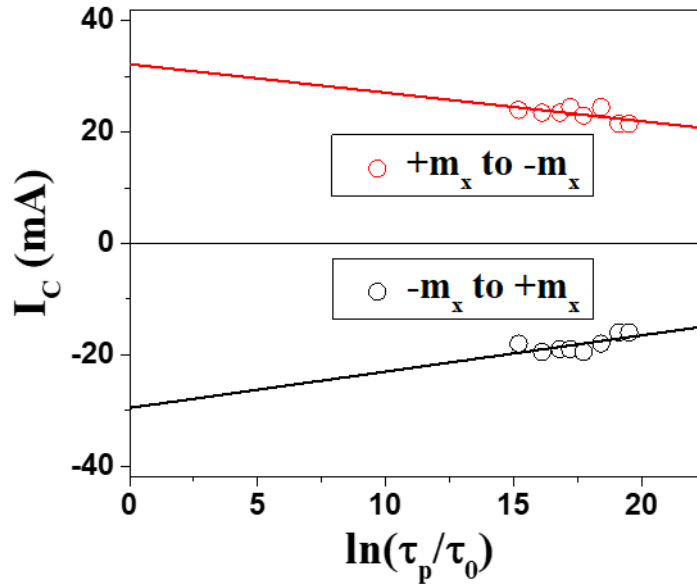


**Figure 5.6.**  $I_C$  vs.  $\ln\left(\frac{\tau_p}{\tau_0}\right)$  for  $+m_x$  to  $-m_x$  and  $-m_x$  to  $+m_x$  (data points are fitted with Eq. (5.9)).

Additionally, we calculated the energy barrier (or thermal stability) between two magnetization saturation states. For high retentivity of a memory device, the industry standard for thermal stability lies  $\sim 40$ -60 k<sub>B</sub>T[26]. We performed current pulse-dependent magnetization switching experiments to calculate the barrier energy between magnetization states in NiFe stack. The calculated barrier energy ( $E_b$ ) was found to be  $\sim 54$  k<sub>B</sub>T which matches well with other SOT switching experiments as well as the industrial standard[28,29].

## 5.5 Conclusion

In summary, we showed that the odd planar Hall signal (O-PHV) exhibits an odd symmetry with the application of an external magnetic field. This motivates us to develop a reading mechanism for detecting magnetization switching of in-plane magnetized type-X devices by simply employing the DC technique in line with the widely utilized AHE technique for the type-Z device. We verified our reading mechanism in the Pt/Co/NiFe/Pt stack. We have engineered this stack by inserting a thin layer of Co to create dissimilar interfaces about NiFe layer. This results generation of considerable FL-SOT apart from the expected AD-SOT. Moreover, the resultant of FL-SOT and Oersted field exceeds the AD-SOT's magnitude. It was shown that the O-PHV has higher signal amplitude than the 'AC technique'. Further, we have detected the current-induced magnetization switching in the Pt/Co/NiFe/Pt stack in presence of a symmetry-breaking DC magnetic field. The near-perfect reproducibility of O-PHV in detecting the current-induced magnetization switching in the Pt/Co/NiFe/Pt stack further confirms its applicability in elucidating the in-plane magnetization switching in type-X devices which may lead to its relevance in detecting future SOT-switching-based memory devices and sensors.



## References

- [1] N. H. D. Khang, T. Shirokura, T. Fan, M. Takahashi, N. Nakatani, D. Kato, Y. Miyamoto, and P. N. Hai, Nanosecond ultralow power spin orbit torque magnetization switching driven by BiSb topological insulator, *Applied Physics Letters* **120**, 152401 (2022).
- [2] H. Wu *et al.*, Spin-Orbit-Torque Switching of Ferrimagnets by Terahertz Electrical Pulses, *Physical Review Applied* **18**, 064012 (2022).
- [3] K. Garello, C. O. Avci, I. M. Miron, M. Baumgartner, A. Ghosh, S. Auffret, O. Boulle, G. Gaudin, and P. Gambardella, Ultrafast magnetization switching by spin-orbit torques, *Applied Physics Letters* **105**, 212402 (2014).
- [4] Y. J. A. b. Huai, Spin-transfer torque MRAM (STT-MRAM): Challenges and prospects, **18**, 33 (2008).
- [5] W.-G. Wang, M. Li, S. Hageman, and C. L. Chien, Electric-field-assisted switching in magnetic tunnel junctions, *Nature Materials* **11**, 64 (2012).
- [6] T. Kawahara, K. Ito, R. Takemura, and H. Ohno, Spin-transfer torque RAM technology: Review and prospect, *Microelectronics Reliability* **52**, 613 (2012).
- [7] A. Manchon, J. Železný, I. M. Miron, T. Jungwirth, J. Sinova, A. Thiaville, K. Garello, and P. Gambardella, Current-induced spin-orbit torques in ferromagnetic and antiferromagnetic systems, *Reviews of Modern Physics* **91**, 035004 (2019).
- [8] A. Manchon, H. C. Koo, J. Nitta, S. M. Frolov, and R. A. Duine, New perspectives for Rashba spin–orbit coupling, *Nature Materials* **14**, 871 (2015).
- [9] J. Sinova, S. O. Valenzuela, J. Wunderlich, C. H. Back, and T. Jungwirth, Spin Hall effects, *Reviews of Modern Physics* **87**, 1213 (2015).
- [10] J. E. Hirsch, Spin Hall Effect, *Physical Review Letters* **83**, 1834 (1999).
- [11] K. Garello *et al.*, Symmetry and magnitude of spin–orbit torques in ferromagnetic heterostructures, *Nature Nanotechnology* **8**, 587 (2013).
- [12] C. O. Avci, K. Garello, M. Gabureac, A. Ghosh, A. Fuhrer, S. F. Alvarado, and P. Gambardella, Interplay of spin-orbit torque and thermoelectric effects in ferromagnet/normal-metal bilayers, *Physical Review B* **90**, 224427 (2014).
- [13] N. H. D. Khang and P. N. Hai, Spin–orbit torque as a method for field-free detection of in-plane magnetization switching, *Applied Physics Letters* **117**, 252402 (2020).
- [14] Y. Takahashi, Y. Takeuchi, C. Zhang, B. Jinnai, S. Fukami, and H. Ohno, Spin-orbit torque-induced switching of in-plane magnetized elliptic nanodot arrays with various easy-axis

directions measured by differential planar Hall resistance, *Applied Physics Letters* **114**, 012410 (2019).

[15] G. Mihajlović, O. Mosendz, L. Wan, N. Smith, Y. Choi, Y. Wang, and J. A. Katine, Pt thickness dependence of spin Hall effect switching of in-plane magnetized CoFeB free layers studied by differential planar Hall effect, *Applied Physics Letters* **109**, 192404 (2016).

[16] S. Fukami, T. Anekawa, C. Zhang, and H. Ohno, A spin–orbit torque switching scheme with collinear magnetic easy axis and current configuration, *Nature Nanotechnology* **11**, 621 (2016).

[17] Y.-T. Liu, C.-C. Huang, K.-H. Chen, Y.-H. Huang, C.-C. Tsai, T.-Y. Chang, and C.-F. Pai, Anatomy of Type-x Spin-Orbit-Torque Switching, *Physical Review Applied* **16**, 024021 (2021).

[18] L. Liu, O. J. Lee, T. J. Gudmundsen, D. C. Ralph, and R. A. Buhrman, Current-Induced Switching of Perpendicularly Magnetized Magnetic Layers Using Spin Torque from the Spin Hall Effect, *Physical Review Letters* **109**, 096602 (2012).

[19] L. Liu, C.-F. Pai, Y. Li, H. W. Tseng, D. C. Ralph, and R. A. Buhrman, Spin-Torque Switching with the Giant Spin Hall Effect of Tantalum, *Science* **336**, 555 (2012).

[20] R. Posti, A. Kumar, D. Tiwari, and D. Roy, Emergence of considerable thermoelectric effect due to the addition of an underlayer in Pt/Co/Pt stack and its application in detecting field free magnetization switching, *Applied Physics Letters* **121**, 223502 (2022).

[21] S. Li and T. Zhu, Contribution of the magnetic anisotropy to the current induced spin–orbit effective fields in the in-plane magnetized ferromagnetic metal and heavy metal multilayers, *Japanese Journal of Applied Physics* **59**, 040906 (2020).

[22] F. Xue, S.-J. Lin, P. Li, W. Hwang, Y.-L. Huang, W. Tsai, and S. X. Wang, Spin–orbit torques of an in-plane magnetized system modulated by the spin transport in the ferromagnetic Co layer, *APL Materials* **9**, 101106 (2021).

[23] S. Emori, T. Nan, A. M. Belkessam, X. Wang, A. D. Matyushov, C. J. Babroski, Y. Gao, H. Lin, and N. X. Sun, Interfacial spin-orbit torque without bulk spin-orbit coupling, *Physical Review B* **93**, 180402 (2016).

[24] X. Fan, J. Wu, Y. Chen, M. J. Jerry, H. Zhang, and J. Q. Xiao, Observation of the nonlocal spin-orbital effective field, *Nature Communications* **4**, 1799 (2013).

[25] A. Ghosh, K. Garello, C. O. Avci, M. Gabureac, and P. Gambardella, Interface-Enhanced Spin-Orbit Torques and Current-Induced Magnetization Switching of

$\text{Pd}/\text{Co}/\text{AlO}_x$  Layers, Physical Review Applied **7**, 014004 (2017).

[26] A. D. Kent and D. C. Worledge, A new spin on magnetic memories, Nature Nanotechnology **10**, 187 (2015).

[27] M. Wang *et al.*, Current-induced magnetization switching in atom-thick tungsten engineered perpendicular magnetic tunnel junctions with large tunnel magnetoresistance, Nature Communications **9**, 671 (2018).

[28] L. Zhu, L. Zhu, S. Shi, D. C. Ralph, and R. A. Buhrman, Energy-Efficient Ultrafast SOT-MRAMs Based on Low-Resistivity Spin Hall Metal Au<sub>0.25</sub>Pt<sub>0.75</sub>, Advanced Electronic Materials **6**, 1901131 (2020).

[29] S. Z. Rahaman *et al.*, Pulse-Width and Temperature Effect on the Switching Behavior of an Etch-Stop-on-MgO-Barrier Spin-Orbit Torque MRAM Cell, IEEE Electron Device Letters **39**, 1306 (2018).

## Chapter 6

### Conclusions and Outlook

Finally in this chapter a comprehensive conclusion to the work carried out in thesis is provided.

In Chapter 1, introductory background which introduces spin-orbit coupling and its effects on magnetic heterostructures was discussed. Methods to convert charge into spin current (spin Hall effect, and Rashba effect), and magnetization dynamics in presence of spin orbit torques were also discussed in this part. Further, it also reviews the existing methodologies to characterize SOT and detect SOT induced magnetization switching.

In Chapter 2, we discussed the experimental techniques that are used to fabricate and characterize our magnetic heterostructure devices. Along with discussing the basic deposition and magnetic characterization techniques, we discussed the details of our custom-built transport measurement system, utilizing which we performed all our transport experiments.

In Chapter 3, we discussed that Ta addition to the asymmetric stack (Pt/Co/Pt) gives rise to several compelling effects, viz., thermoelectric effects [particularly, anomalous Nernst effect (ANE)], and enhanced perpendicular magnetic anisotropy which was negligible in a Pt/Co/Pt stack. For this Ta/Pt/Co/Pt stack, the antidamping-SOT values are evaluated after carefully removing the contribution of the ANE and it is found to match the AD-SOT of the Pt/Co/Pt stack. We have observed current-induced field-free magnetization switching in Ta/Pt/Co/Pt stack with Co thickness gradient. Furthermore, we have utilized the thermoelectric effects to develop a technique to detect the field-free magnetization switching. This technique detects the second harmonic ANE signal as a reading mechanism. Using ANE symmetry with the applied current, the switching can be detected in a single current sweep which was corroborated to the conventional DC Hall method.

In chapter 4, we explored the combined symmetry of SOT and DC field to stabilize multistate behavior. Further, we observed this behavior in Pt/Co/Pt stack which is one of the earliest model systems for PMA studies thereby expanding the potential applicability of our results. We

verified that the integration of SOT with a static field yields multiple metastable saturation states, characterized by the magnitude and polarity of the static field. Furthermore, our finding suggests that this phenomenon is induced by both SOT and external field simultaneously. This effect enables the manipulation of energy barrier between states. At last, we tried to resolve the initialization problem of modern memristor devices through experimental demonstration of initialization-free multistate memory.

In chapter 6, we demonstrated that the odd planar Hall voltage (O-PHV) signal exhibits an odd symmetry with the application of an external magnetic field which motivates us to develop a reading mechanism for detecting magnetization switching of in-plane magnetized heterostructures. We verified our DC-based reading mechanism in the Pt/Co/NiFe/Pt stack where a thin Co layer is inserted to create dissimilar interfaces about the NiFe layer. Remarkably, the current-induced in-plane fields are found to be significantly large in Pt/Co/NiFe/Pt stack. Furthermore, we employed the O-PHV method to detect the current-induced magnetization switching. The pure DC nature of the writing and reading mechanism of our proposed in-plane magnetization detection technique through O-PHV makes it the easiest one. Moreover, we show high repeatability and easy detection of our proposed method which will open avenues toward in-plane SOT switching based memory devices and sensors.

Beyond this thesis work, this work can be extended to multiple direction.

It would be great to observe the visualization of intermediate states in second harmonic SOT switching signal which was discussed in chapter 3. Other than this, SOT switching loop shift method in presence of HZ can be used to detect SOT efficiency and this method could be better than widely used field induced loop shift method. The reason being, conventional method does not discuss the hysteresis shrink due to joule heating, however in SOT switching loop shift this is inherently there. Further, multistate behavior with current induced switching minor loops can provide multi-level-multistate behavior where a 2D memory architecture can be saved in a single device. Furthermore, using the in-plane switching detection method the SOT switching in NiFe can be explored. It recently found that NiFe have a self-torque which is considered to be induced from surface layer.

